Department of Precision and Microsystems Engineering

Lubrication-film height imaging for hydrostatic bearings with fluorescence. With an analytic solution to the plane-parallel, fluorescent radiative transfer equation.

P.A. Lok

Report no : 2022.44
Coach : Dr ir. R.A.J. van Ostayen
Specialisation : Mechatronic System Design
Type of report : Master Thesis
Date : 07-08-2022

Figure 1: Chlorophyll extract in ethyl acetate fluorescences brilliantly in deep blue light. Within the hand palm's creases, the liquid gathers and shines brighter than on the surrounding skin where the liquid film is thin. The deep layer inside the beaker appears deep red while the adjacent, thin splotch glows orange. By Maxim Bilovitskiy, CC BY-SA 4.0, `https://creativecommons.org/licenses/by-sa/4.0`, via Wikimedia Commons

Master-exam date: 22 august 2022
Exam committee: Dr *ir.* R.A.J. van Ostayen (chair)
Dr S. Iskander-Rizk
Dr E. van der Kolk

Dear reader, before you lays more than a years' worth of work. At the start of the project, I did not know what I was getting into. Initially thinking the master-thesis subject was about engineering a measurement system for hydrostatic bearings, I quickly found out that at its core it was all about understanding physics. To be more precise, the physics of radiative transfer and optics. I, who happily avoided any courses even remotely related to those subjects was about to spend most of my productive time on precisely that. It seems to have worked out alright, for I found the matter to be unexpectedly fascinating.

The endeavour could not have been done successfully without the help and support of others. Starting with the Precision and Microsystem Engineering department, I am grateful towards my supervisor Dr ir. R. van Ostayen, who continuously incited my to push further and do more. Without his goading, I am quite sure that experimental verification of the models would never have been done. From the same department, I convey my gratitude Dr N. Bhattacharya who gave useful advice about the subject's relevance. Of the Radiation Science & Technology department, I would like to thank Dr E. van der Kolk. He helped me start the experimental side of the project by introducing me to lab technician J. de Haas, who taught me how to use the spectrometer. I am especially indebted to Dr R. Koekoek from the Analysis research group at the Delft Institute of Applied Mathematics: he demonstrated me that exponential integrals form the natural solution to the source term integral. Moreover, I thank the lab technicians G. Emmaneel, P. van Holst, A. van den Boogaard for sharing their practical knowledge and helping me find the right hardware. Furthermore, I thank S. Bezelev, who helped me tune my presentations and often listened to my ramblings on some arcane project detail. Lastly, I would like to impart my gratitude towards my parents, Ankie and Gerard: you strongly supported me during the master thesis, and also far beyond.

Pieter Lok
Delft, 7 august 2022

Summary

The performance of hydrostatic bearings is in part decided by their lubrication-film height shape. Imaging the shape can be done by dissolving fluorescent dyes in the layer. However, current imaging techniques are rooted in heuristics, and as such, their physics, design parameters, and error sources are not quantitatively understood. To fully grasp and consequently design the ultimate measurement system, the governing equation—the fluorescent radiative transfer equation—is solved analytically for a plane-parallel system. The new solution method assumes that fluorescent radiative transfer is well-described by the first two photon generations. Verification is done experimentally and by a concurrent Monte Carlo method. The model also successfully predicted the response of a real measurement setup. Further model analysis led to the understanding of factors such as: camera positioning; light source design; and the effect of the reflective background on which the lubrication layer lays. The insights suggest a practical implementation for a dynamic imaging setup.

Contents

List of Symbols

a	molar absorptivity / L mol^{-1} m^{-1}
c	Speed of light / m s^{-1}
	molar concentration / mol L^{-1}
C_{d}	integration constant; radiation toward the mirror / q s^{-1} m^{-2} sr^{-1}
C_{u}	integration constant; radiation away from the mirror / q s^{-1} m^{-2} sr^{-1}
d	distance travelled by a photon package / m
E	irradiance / q s^{-1} m^{-2}
E_1	exponential integral / -
E_{e0}	source irradiance at the top domain boundary / q s^{-1} m^{-2}
f	calibration function
g	calibration function
h	Planck constant / J s
	film height / m
l	path length of a ray inside a homogeneous domain / m
$\mathbf{l}$	local direction coordinates at a point on the ray path / -
L	radiance / q s^{-1} m^{-2} sr^{-1}
L_{d}	direct radiance solution; first photon generation
L_{g}	general radiance solution
L_{i}	indirect radiance solution; second generation
L_{p}	particular radiance solution
N_{a}	Avogrado's number
n	index of refraction / -
q	quantum yield / -
$q_{\mathrm{f_k}}$	spectral quantum yield of dye k / -
q_{d}	spectral quantum yield of dye k for the direct/first generation / -
q_{i}	spectral quantum yield of dye k for the indirect/second generation / -
r	radius / m
R	rotation matrix / -
$\mathcal{R}$	camera sensitivity / V W^{-1} or V q^{-1} s
	transform that changes the direction cosine's sign / -
$\Re$	real part of a complex number / -
s_{o}	area / m^2
s	projected area / m^2

$\mathbf{s}$	vector of direction cosines / -
S	source term / q s^{-1} m^{-2} sr^{-1}
t	time / s
T	shutter time / s
	Transmittance of an object / -
u	uniform distribution / -
U	Energy of a photon package / J
x	coordinate / m
y	coordinate / m
z	coordinate / m
$\mathbf{x}$	position vector / m
$\bar{\mathbf{x}}$	direction vector / -
α	absorptivity / m^{-1}
α_{e}	total, representative absorptivity for the excitation light / m^{-1}
α_{es}	a single dye's representative absorptivity for the excitation light / m^{-1}
α_{d}	total, representative absorptivity for the direct/first generation of fluorescent photons / m^{-1}
α_{ds}	a single dye's representative absorptivity for the direct/first generation of fluorescent photons / m^{-1}
α_{i}	total, representative absorptivity for the indirect/second generation of fluorescent photons / m^{-1}
ϵ	emissivity / -
$\bar{\epsilon}$	emissivity, area under the curve normalized / -
η	efficiency / -
θ	polar angle with the z-axis / rad
θ_{e}	excitation angle; polar angle of the light source irradiance / radian
θ_{v}	view angle; representative polar angle of the observed radiance/ rad
Θ_{d}	set of angles that make radiance point towards the mirror / rad
Θ_{u}	set of angles that make radiance point away from the mirror / rad
λ	wavelength of electromagnetic radiation / nm
	as subscript: spectral derivative for radiant flux quantities such as: L, E, and Φ
	as subscript: index to a small waveband centred on a wavelength λ
λ_{e}	representative wavelength of the irradiance [m]
μ	integrating factor / -
Ξ	ratio of pixel grey values. Measurement response of the system. [-]
ρ	reflectivity / -
ρ_{d}	representative reflectivity for the excitation irradiance / -
ρ_{e}	representative reflectivity for the first/direct generation / -
ρ_{i}	representative reflectivity for the second/indirect generation/ -
τ	excited state lifetime / s
	transmissivity of a filter / -
ϕ	azimuthal angle / rad
Φ	radiant flux / q s^{-1}
ω	solid angle / sr

1 Introduction

Hydrostatic bearings offer high load capacity, low friction, little wear, high stiffness, and zero stick-slip. They use a thin layer of high-pressure liquid to separate counter surface and bearing surface [35, 38]. The liquid film layer only applies a very low shear friction to the bearing, and non-traditional lubricants can be used due to the lack of surface contact. An interesting example could be the use of water instead of oils and greases [37].

Several applications benefit from the hydrostatic bearing's properties: pumps, high precision stages and spindles, and large systems such as civil engineering projects. However, hydrostatic bearings need stringent surface-form tolerances to work. This can be problematic in the case of large systems: maintaining exacting manufacturing tolerances over great length scales is difficult; especially the waviness in the counter surface is a precarious problem. A solution is to add compliance so the bearings can adapt to the waviness. Models and prototypes that do such a thing have been developed within the Thin Film group at the department of Precision and Microsystems Engineering at TU Delft [26, 36]. The challenge is to verify both models and prototypes: dynamic, spatial measurements of the film height play an important role here. Consequently, a master thesis project was done to explore the potential of fluorescence as an imaging technique [32]. It was found that fluorescence could work, therefore this current thesis was created with the aim to develop the technique further—readers interested in more background to hydrostatic bearings, or the choice for this particular imaging method are referred to the accompanying literature study.

This report answers the broad question: *What is the best way to use fluorescence for the imaging of lubrication-film heights under hydrostatic bearings in a way that is both practical and repeatable?* The approach is to better understand the physics of the governing equation: the fluorescent radiative transfer equation for a plane-parallel domain. Once we understand that, a better measurement setup can be designed. The method is to solve the governing equation and verify its analytic solution by comparing it to Monte Carlo simulations and practical experiments. Then, the analytic solution predicts the registered behaviour of a real measurement setup for confirmation of its predictive power. Hereafter, it analyses the effect of several design parameters. The resulting body of knowledge answers the main question by proposing the ultimate imaging setup design.

The report is structured in the following way. Chapter 2 gives the context for fluorescence in height imaging. It introduces the measurement problem, tells how fluorescence could help, how fluorescence works, and how such methods are embodied in literature. The chapter continues with an introduction to the most promising imaging method: the emission reabsorption laser induced fluorescence. The work discusses necessary modifications to make it fit our needs; the new method is called for convenience generalized emission reabsorption induced fluorescence. The issue of reflection effects is mentioned. Finally, the resulting study approach is discussed. Chapter 3 proves an analytic solution to the fluorescent radiative transfer equation with experimental verification. A concurrent Monte Carlo method is used for comparison of input to output behaviour. A journal paper format is chosen with the intention for

future publication. As such, parts of Chapter 2 are repeated here to make it an independently readable text. In Chapter 4, the analytical solution is used to explore the imaging method. Effects of observing large areas are investigated, an important assumption about reflectivity is critically analysed, design parameters are explored, and some practical experiments are conducted to see if the method can predict a real measurement setup. Chapter 5 suggests a functional implementation of all that is learned into a dynamic imaging setup design. It wraps up with pragmatic suggestions to engineers looking to use the method.

2

Fluorescence in the Context of Film Height Imaging

The goal is to image liquid film heights. A promising approach is to use fluorescence. In this chapter, a gentle introduction to fundamental concepts is given. To do so, several parts of the old literature study and parts of the paper in chapter 3 are restated.

2.1. The measurement problem

We are interested in liquid film heights underneath hydrostatic bearings: their working principle is not unlike that of an air hockey puck or hovercraft. An archetypical deep-pocket bearing—Figure 2.1—carries a load by floating on a cushion of high-pressure liquid, which lifts the bearing from the sliding surface. In proper operation, there is no bearing to sliding surface contact. The deep pocket is filled with a liquid, whose high pressure is maintained by creating a tiny gap with a large outflow resistance to the surrounding environment; imaging squeezing-off a garden hose: the harder you squeeze, the smaller the gap, the greater the flow resistance. The 2-dimensional gap-height surface, h, and pocket geometry largely determine relevant properties such as: load capacity, stiffness, and damping. There are many more ways to design a proper hydrostatic bearing, that is all-up to the engineer's creativity and skills. The latter is especially true for the design concepts considered within the research group. However, in all designs, the shaping of film height is the critical factor that determines functionality [23, 26, 35, 38]. Modelling of film height is not enough, but proper test are needed to verify design performance in the real world. We are especially interested in dynamic load cases where a bearing needs to follow a curved counter surface. Examples are pumps , or sluice gates [37]: obtaining very strict parallel-form tolerances on a sliding surface 10's of meters long underwater is impossible . During

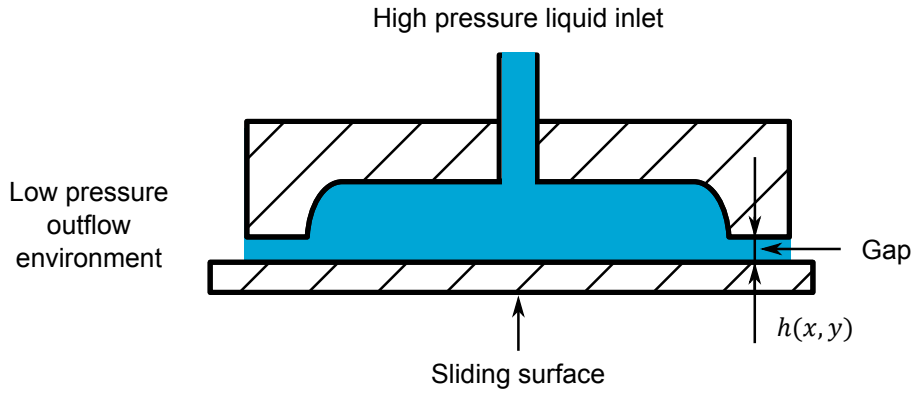

Figure 2.1: A typical, deep-pocket hydrostatic bearing on its sliding surface. Not to scale.

such movements, the bearing and sliding surface can easily misalign and create deviations from the ideal film height, which in turn negatively affects performance. In the worst case, the bearing makes contact with the sliding surface resulting in friction and wear. Clever designs prevents such problems. Several ideas for such bearings were conceived within the Thin Film group, but they need verification. Therefore, an imaging method was needed that can look at the lubrication film and recover its height. A more deeper introduction to hydrostatic bearings can be found in the literature study.

During the initial project phase the following, most important, specifications were agreed upon

Relevant design criteria	
Film thickness	10 µm to 600 µm
Observation area	100×100 mm
No modifications to the bearing	
The sliding surface can be made transparent	

2.2. How fluorescence could help

The fluorescence phenomenon was a great candidate to investigate for our imaging problem. It has a proven track record in the literature, to which we will return in the section on imaging method choice—section 2.4. Interestingly, the inside of this thesis's cover reveals the two main imaging methods and a lot of the pitfalls—see Figure 1. Take a look, we have a scene bathing in blue light, yet the liquid glows red; it has a dissolved fluorescent dye. Fluorescence changes wavelengths of in and outgoing light. The input signal, blue light, can be easily separated from the output signal, red light. We use filters for this purpose. The first method is to use intensity: in the palm of the hand, liquid pools in the creases which shine more brightly then the smudged, thin film surrounding it. The second method is to use colour shifts: take a look at the beaker, filled by a thick layer and with deep red glow inside, while adjacent a shallow drip has an orange sheen. The cause of this colour shift is explored in section 2.4.3.

Several pitfalls are visible too. Design of the light source matters: the area left to the beaker bathes in light while the downright corner is barely lit. A problem exacerbated by differences in reflectivity of liquid's underground: the glossy table-top versus the dull skin. As it will turn out in chapter 3, for a well-designed system, fluorescent radiance is linear in excitation light irradiance. Another problem is the viewing angle: the camera is at an angle with the liquid inside the beaker. A pixel does not see the true thickness, but rather the top of a diagonal ”tube” of liquid. Refraction of light at the liquid-to-glass and glass-to-air also means that the angle of the ”tube” is not the same as we perceive it to be from the photograph. Unwanted light is another trouble, at the top left corner we see the orange reflection of a light source; if we were to filter for the orange-red light of fluorescence, the orange reflection would be visible in the photograph. Fluorescence as an imaging method for film thicknesses is fraught with difficulties, which need to addressed in proper measurement design. But first, a better understanding how a fluorescent molecule works is required.

2.3. Basic physical principles of fluorescence

Fluorescence is a three-stage process that happens in specific molecules called fluorophores or fluorescent dyes [10, p.1]. The process is usually described by a Jablonski diagram [18, p. 3][8, p. 5-7]—see Figure 2.2.

1. Excitation. A fluorophore's electrons are in its ground state S_0, until it absorbs a photon with an energy of $E = \frac{hc}{\lambda}$ that is supplied by an external light source. h the Planck Constant, c the speed of light in vacuum, and λ the wavelength in vacuum. After absorption, a fluorophore gets to a higher electronic state such as S_1, S_2, S_3... each with a greater energy. Every singlet state has vibrational energy levels denoted by 0,1,2,3,.... The ground-to-singlet transition usually takes place from the lowest vibrational level of S_0 and costs 1 fs [18, p. 5] [8, p. 7].

2. Excited-State. In the vast majority of fluorophores, a rapid—typically 1 ps [18, p. 7]—internal conversion process follows whereby energy is dissipated radiation-less until lowest vibrational level of S_1

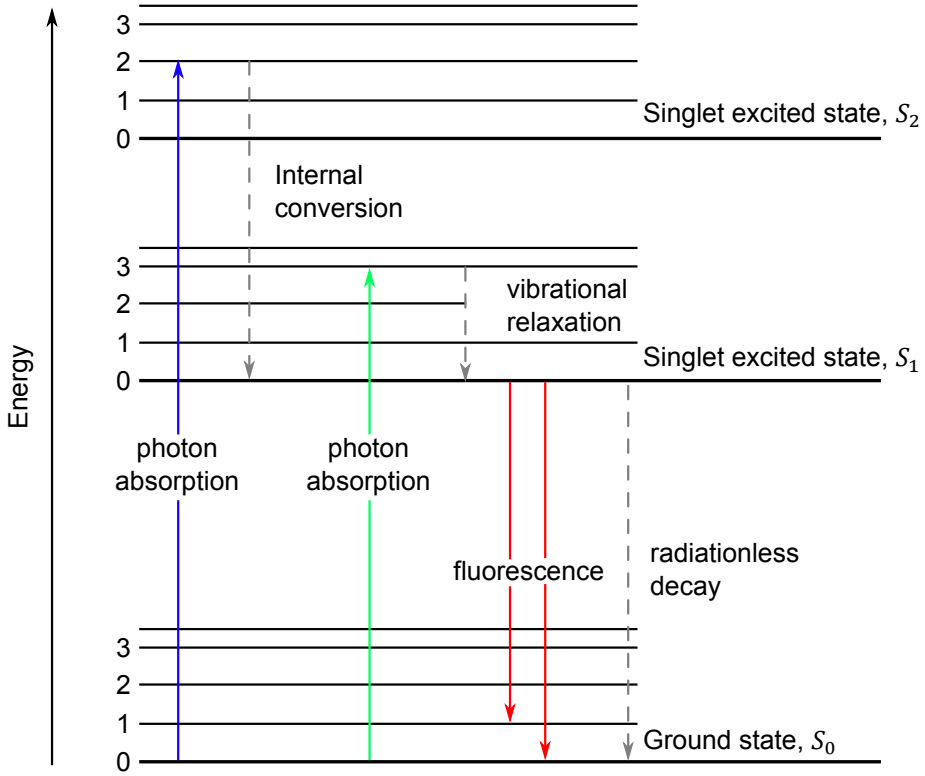

Figure 2.2: Jablonski diagram
describes the fluorescence process, including non-radiative effects. The numbers indicate vibrational levels within the electronics states S_0, S_1 and higher. Picture based on the discussion by Lakowicz [18].

is reached. The radiation exchanges occurs often with the fluorophore's molecular environment via collisions—also called quenching. If the excess energy of S_1 is not further dissipated by radiationless decay, the third stage can commence. The excited-stage for regular dyes exists up to roughly 10 ns [18, p. 5], [8, p. 18].

3. Emission. The fluorophore sheds-off any remaining energy by jumping from the S_1 to a vibration level in S_0. It does so by emitting a new photon which likely has a lower energy than the absorbed photon, as quenching processes removed some of the fluorophores energy.

The efficiency of this process is given by the quantum yield: the mean chance of a photon absorption leading to a photon emission. One usually estimates it macroscopically by using

$$q = \frac{\text{photons emitted}}{\text{photons absorbed}} \tag{2.1}$$

q depends on dye and environment but not on the absorbed photon's wavelength [10, 18, ;p. 3, p. 7]. A short aside, with environment we can mean: solvent, temperature, pH, contaminants etc.

The process of fluorescence is best described by molar absorption- and emission spectrums—an typical example can be found in Figure 2.3. An absorption spectrum describes how well an external light source at a given wavelength is able to cause fluorescence. Emission spectrums describe the likelihood of a photon emission for a wavelength. The spectrums' peaks are determined by the structure of the first singlet state S_1. Emissions spectrums depend on dye and environment and not on the absorbed photon's wavelength [10, 18, p3; p. 7-9]. A photon emission more energetic than the absorbed may occur if there are many populated vibration levels in S_0 present or if thermal energy is added to the system [8, p. 8]. Therefore, an overlap in absorption and emission spectrum is permissible and not a violation of energy conservation.

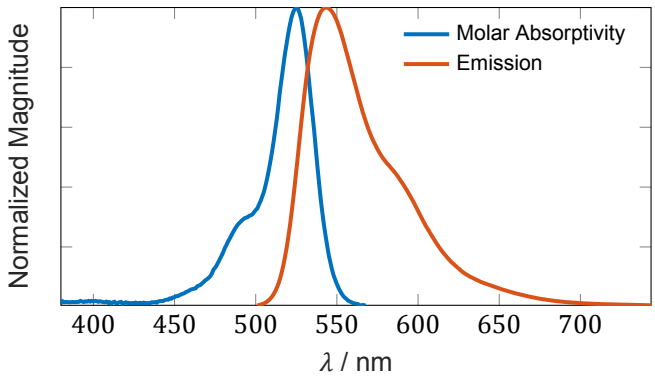

Figure 2.3: Exemplary normalized spectra of absorption and emission. The dye absorbs at shorter wavelengths and emits at longer ones. An overlap between both spectrums is a common occurrence.

2.4. Fluorescent film-height imaging in the literature

The liquid film height, h, is a spatially distributed quantity that needs to be visualized nearly instantaneously for dynamic bearing operation. Three fluorescent film height imaging techniques where found in the literature, which will now be discussed. All methods are depicted in Figure 2.6. The discussion will show that the path to take is Emission Reabsorption Laser Induced Fluorescence (ERLIF). However, the method needs tuning to our needs of a larger viewing area and different light source. The new method is called Generalized Emission Reabsorption Induced Fluorescence (GERIF).

2.4.1. Direct method

Any measurement system trying a measure a scalar quantity does not do it directly. Instead, the measurement system response is correlated to the quantity. Think of a simple mercury thermometer, it does not measure temperature straight, but the mercury level raises-and-falls with changing temperature. The calibration function is the scale alongside the glass.

Direct measurement of emissions has the most simple calibration function of any fluorescent imaging technique. Go back to the thesis's front-page inside. Dye has pooled in creases of the hand palm and the layer shines much more brightly. The deeper the layer, the more molecules, the more light is absorbed and emitted. The camera includes a filter to block out all light, except a small waveband around the fluorescent emission peak. We then can correlate captured radiant flux by a camera pixel during a shutter time T to the height via a calibration function

$$h = f\left(\int_T \Phi \mathrm{d}t\right)$$

The calibration function contains factors such as: the sensitivity of the camera, the transmittance of the filters, transmission of the bearing's sliding surface. The calibration function is usually acquired by imaging a film of known thickness and seeing what pixel grey values are obtained. According to the literature, the method is error prone and very difficult to calibrate. A classic study on oil film behaviour on a spinning cylinder noted that calibration was: "the least exact part, dependent on the underlying surface and scattering" [34]. A similar study on open-channel flow and droplets [9] faced alike problems. They tried to tackle the surface reflection dependency by adding a calibration vessel made of the same material as the background in the experiment, but achieved accuracy errors, as a percentage of the real value, of between 25.6% and 4.9% at the lowest-, and upper boundary. Measurement range was 0.100 mm to 2.000 mm over an 81×61 mm^2 area. Another great drawback is that Φ depends on the irradiance coming from the light source: a light source can vary spatially and temporary—think once again about the cover picture's variations in blue light. A higher irradiance means more fluorescent photon production: an effect that mattered in that particular study, as LEDs' intensities changed by thermal drift. Direct measurements emission techniques are not a good method for our measurement problem.

2.4.2. Ratioed Image Film Thickness Meter

Ratiometric techniques—also called intrinsically referenced methods— are popular for fluorescent measurements far beyond height imaging, as they reject disturbances such as instrument and light source drift which simplifies setup calibration [30, 31]. RIFTP is such a technique for film thickness, it was developed by Husen et al. [13, 14] to solve the problem of source light inhomogeneity—remember, fluorescent photon production depends on the number of light source photons available. It works by measuring the radiation pattern of the light source, and then us it to normalize the imaged fluorescent signal. To do so, a fluorescent layer with a weak absorbance is deposited on a diffuse-reflecting surface. Also called a Lambertian reflector, which has a reflection brightness that is equal in all directions: think of rough paper, or snow. Excitation light will barely lose irradiance when traversing the weakly absorptive layer, it will thus everywhere have approximately the same irradiance as it had entering the layer. When reflected from the Lambertian surface, its radiance will always be the same, no matter at which angle we observe the layer. Therefore, by imaging the reflections, we do know what the irradiance pattern was at the top of the layer and can remove its influence from the fluorescent measurement. Reflected excitation and fluorescent radiant fluxes are captured separately by the camera with help from two bandpass filters. They were swapped by help of a filter changer; changing filters costs time, so we can only image static films. Taking the fluxes' ratio gives the liquid film height with help from a calibration function

$$h = f\left(\frac{\int_{T_1} \Phi_{\text{fluorescent}}\,\mathrm{d}t}{\int_{T_2} \Phi_{\text{light source}}\,\mathrm{d}t}\right)$$

To demonstrate the method's robustness, a drop of liquid with a fixed volume was moved to 16 different places in the camera's field of view. Drop volume measurements showed that the standard deviation of the mean was 2.6 %. In one of the other experiments, the measurement range was approximately 8 µm to 86 µm over 3.5×19.0 cm^2. The method can easily be upscaled to layer thicknesses in which we are interested, and it shows itself to be robust, repeatable and easy to calibrate. However, the previous master thesis [32] used the method by applying a white matte coating to the bearing. A modification of the bearing is an extra uncertainty when verifying bearing design models, and therefore the method is rejected.

2.4.3. Emission Reabsorption Laser Induced Fluorescence method

ERLIF is a small-area layer-height measurement method that was developed by Hidrovo and Hart [11]. The phenomenon on which it is based can be seen on the cover image were the beaker has a deep, red layer and the droplet on the left is thin and orange. It is a colour shift method, although the paper introduces it in terms of intensity. The workings principle is as follows: emissions and absorption spectra of one or more dyes may overlap, for an example see Figures 2.3 and 2.4a. Therefore, emitted photons may encounter another fluorophore before they can leave the layer, so they get absorbed and re-emitted. This does two thing: first photons at wavelengths in the overlapping spectrums get depleted; secondly, absorbed photons get re-emitted, which usually happens at longer wavelengths. The combined effect is a red-shift: the bulk of the photons are now found at longer wavelengths.

Hidrovo and Hart utilized the red-shift phenomena by simultaneous laser-excitation of two fluorophores. The emission spectrum of one dye strongly overlaps with another's absorption, see for an example of such a system Figures 2.4a and 2.4b. Therefore, the photons produced by the first dye can be re-absorbed by the second dye. This red-shifts the overall spectrum at the top of the layer. The change of a photon meeting dye 2 determines effect strength. For thick layers, with high concentrations the chance increases: the thicker the layer, the longer the photon travel paths are, the greater the chance of meeting another fluorophore so that re-absorption can happen.
The red colour shift is captured by measuring the radiant flux at two small wavebands and then take their ratio

$$h = f\left(\frac{\int_{T_1} \Phi_{\text{waveband 1}}\,\mathrm{d}t}{\int_{T_2} \Phi_{\text{waveband 2}}\,\mathrm{d}t}\right) \tag{2.2}$$

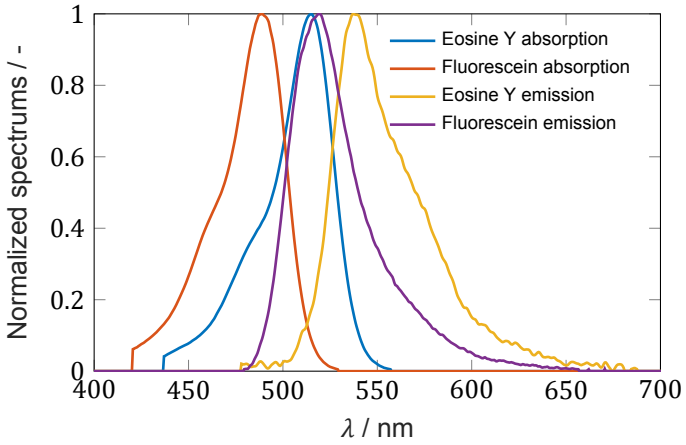

(a) Self-measured absorption spectrums
and emission spectrums of Fluorescein and Eosin Y—water, room temperature, pH=11.

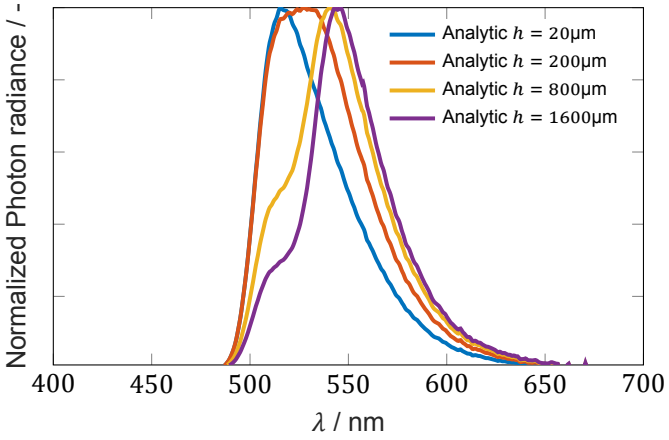

(b) Examplary, red-shift for combined radiance at top of a water layer with thickness h.

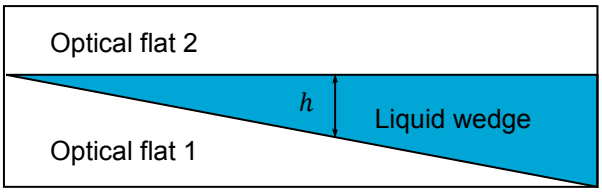

Figure 2.5: Conceptual sketch of the calibration device consisting
of a liquid wedge between two optical flats, as Hidrovo and Hart applied in their ERLIF method [11].

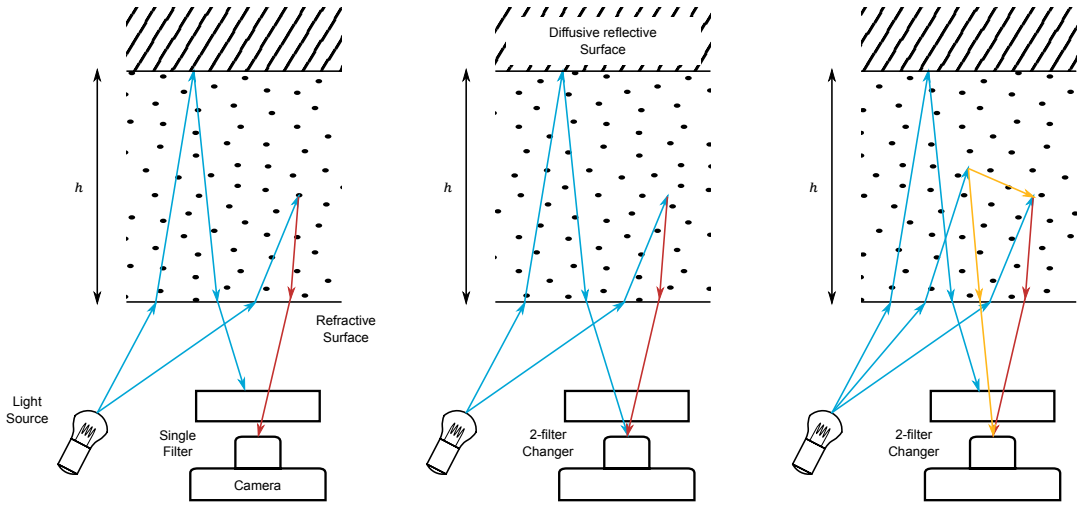

Figure 2.6: Sketches of how measurement principles could be embodied for static imaging; the setups contain filter changers, swapping filters takes time, thus only static layers can be viewed. The exception is direct imaging, as there is no filter changer present. From left to right: direct, RIFTP, and GERIF.

For an example applied to Figure 2.4b, take two bandpass filters, put the first around 520 nm and the other at 530 nm. For deepening layers, the flux seen through the 530 nm grows, while flux through the filter 520 nm weakens.

The journal paper introducing the ERLIF technique promised minimization of typical film thickness errors: optical distortion, variations in surface reflectivity, and excitation. Optical distortion effects are typically the reflectivity and tranmittance of viewing windows, like in our transparent bearing slide surface. It has a demonstrated measurement range of 5 µm to 400 µm at an accuracy of 1 %, that is close to the film thickness range agreed upon at the start of the literature study—10 µm to 600 µm. They measured an area of roughly an US mint quarter coin, which has a diameter of 24.26 mm. The setup was calibrated by an external, precisely-made device consisting of two optical flats, so a high accuracy was obtained—see Figure 2.5 for a conceptual sketch. They could make such a precise device because, according to the methodology, background reflections errors are minimized. If that is true, creating a device becomes a straightforward geometrical manufacturing problem: just create a layer of known height in a way and with materials that is the most easy and accurate. This simplifies calibration a lot. If reflections do matter, the device must include surface and materials like the intended test object with same reflective properties and thus complicating manufacturing.
Since the paper promised such powerful properties, showed remarkable accuracy, and could potentially satisfy all requirements, it was decided to develop it further to the hydrostatic bearing's needs.

2.5. Generalized Emission Reabsorption Induced Fluorescence and its reflectivity dependence

The ERLIF method is successful at its intended purpose. However, applying it to hydrostatic bearings requires a measurement setup redesign. Also, some questions were raised about the rejection of optical distortions and especially the background reflectivity. Addressing the setup design issue for a start. First, the original application successfully imaged a small area: heads-on observation of an area roughly the same size as the cameras' CCD-chips. Hydrostatic bearings are, typically, much larger and therefore viewing-angle effects are important: the camera looks diagonally into the layer, and angular radiance anisotropy is not understood. The small area was lit by a perpendicular expanded laser beam. A larger area needs a different light source with greater beam sizes. Inevitably, sources with divergent beam hitting the layer at an angle are necessary. Thence, what is the effect of irradiance at an angle on the method? GERIF should be able to handle larger viewing areas, and different light sources.
The ERLIF setup itself is clever yet complicated: a laser beam and cameras partially share an optical path with many components in the system such as 3 mirrors, 2 cameras and 2 beam-splitters—see

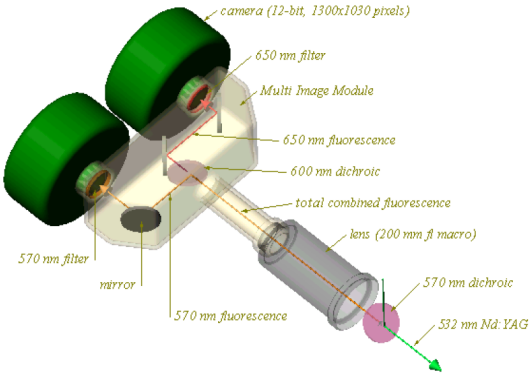

Figure 2.7: The ERLIF system module, copied from [11].

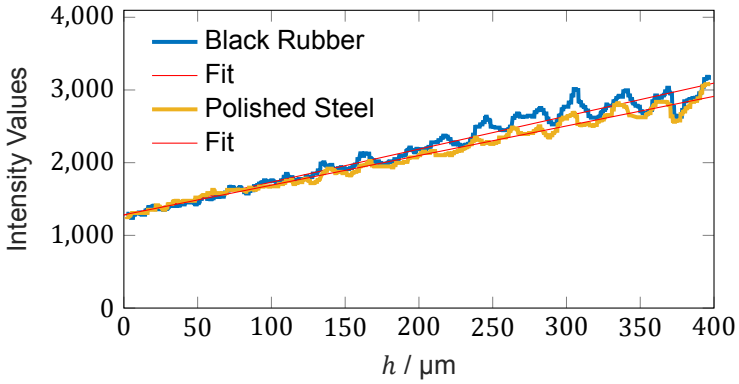

Figure 2.8: Copied, combined data [11]. Data linearly fitted to show a small 12% deviation in the slopes.

Figure 2.7. The shared optical path with two cameras makes the setup perfect for dynamic imaging: we can record both radiant flux signal simultaneous. The study intended to see if a simplified setup can still provide acceptable measurements for a bearing.

Background reflectivity errors are minimized, which we saw was a crucial assumption simplifying system calibration vessels. In the paper, this premise was tested by placing such a calibration vessel on top of a black rubber block and then on a polished steel block. The resulting measurement responses versus h were given in two separate figures and told to be similar. Here they are re-drawn together and linearly fitted in Figure 2.8 to see that there was a small difference. Their slopes deviate by 12%. It was of interest to understand this small deviation and how the method minimizes reflectivity errors.

Intuition tells us that deviations might be possible: for example, if we were to apply a reflective background to the fluorophore combination in figure 2.4a that barely reflects around the first emission peak (515.5 nm), but strongly around the second dye's peak (541 nm), a powerful red-shift should be induced in the normalized spectrum of the layer. Still, even if the background reflection were to matter, it is not an un-assailable problem: just build a more complex calibration device that mimics the reflective background.

To summarize, ERLIF is a powerful method that needs extension to larger areas. A simpler setup for hydrostatic bearings measurements is of interest. The hypothesis that background reflectivity can matter must be verified.

2.6. Approach to the study

A three-fold approach was taken. First, modelling of the physics inside a fluorescent layer. Second, use of the model to predict a test measurement setup for static imaging and explore its design parameters. Three, use the obtained knowledge to suggest the ultimate dynamic imaging setup, and give

practical use guidelines to the engineer.
Modelling consist of three parts: an analytic solution to the fluorescent radiative transfer equation for mirror-like backgrounds, which is a reasonable approximation for precisely made metal parts of a hydrostatic bearing. A secondary model, Monte Carlo, was developed. It verifies that for the same materials and geometric inputs, the models produce the same output spectra. This checks for physics and implementation errors. The third part are the experiments to validate the model in practice.
A numerical study was done into the conditions influencing a real measurement setup: differing angles of view on the lubricating layer, varying light source conditions, reflectivity differences. The Monte Carlo method also simulated a Lambertian reflector background to see if the analytic model has some predictive power there. Finally, measurement data from a real setup was compared with predictions of the analytic model. The predictions were reasonably successful, enough so to develop and optimize a setup that is simpler than the ERLIF one.

3

Analytic Solutions to the Plane-Parallel, Fluorescent Radiative Transfer Equation on a Mirror

Abstract

Modelling the radiant fluxes in fluorescent media is a challenge. This work derives the analytic solution for the stationary, fluorescent radiative transfer equation in a homogeneous, scatter-free, plane-parallel, mirror-bounded domain. The solution is a compact, fast way to calculate spectral radiances for any location inside the domain. It assumes that there are only two generations of by fluorescence produced photons. A computer algebra system with custom integration rules finds the solution. With help from Monte Carlo simulations and practical experiments, the solution is verified. A good agreement between all three methods was found.

3.1. Introduction

Fluorescence is a three-stage process that happens in specific molecules called fluorophores or fluorescent dyes [10, p.1]. The process is usually described by a Jablonski diagram [18, p. 3][8, p. 5-7]—see Figure 2.2.

1. Excitation. A fluorophore's electrons are in its ground state S_0, until it absorbs a photon with an energy of $E = \frac{hc}{\lambda}$ that is supplied by an external light source. h the Planck Constant, c the speed of light in vacuum, and λ the wavelength in vacuum. After absorption, a fluorophore gets to a higher electronic state such as S_1, S_2, S_3... each with a greater energy. Every singlet state has vibrational energy levels denoted by 0,1,2,3,.... The ground-to-singlet transition usually takes place from the lowest vibrational level of S_0 and costs 1 fs [18, p. 5] [8, p. 7].

2. Excited-State. In the vast majority of fluorophores, a rapid—typically 1 ps [18, p. 7]—internal conversion process follows whereby energy is dissipated radiation-less until lowest vibrational level of S_1 is reached. The radiation exchanges occurs often with the fluorophore's molecular environment via collisions—also called quenching. If the excess energy of S_1 is not further dissipated by radiationless decay, the third stage can commence. The excited-stage for regular dyes exists up to roughly 10 ns [18, p. 5], [8, p. 18].

3. Emission. The fluorophore sheds-off any remaining energy by jumping from the S_1 to a vibration level in S_0. It does so by emitting a new photon which likely has a lower energy than the absorbed photon, as quenching processes removed some of the fluorophores energy.

The efficiency of this process is given by the quantum yield: the mean chance of a photon absorption

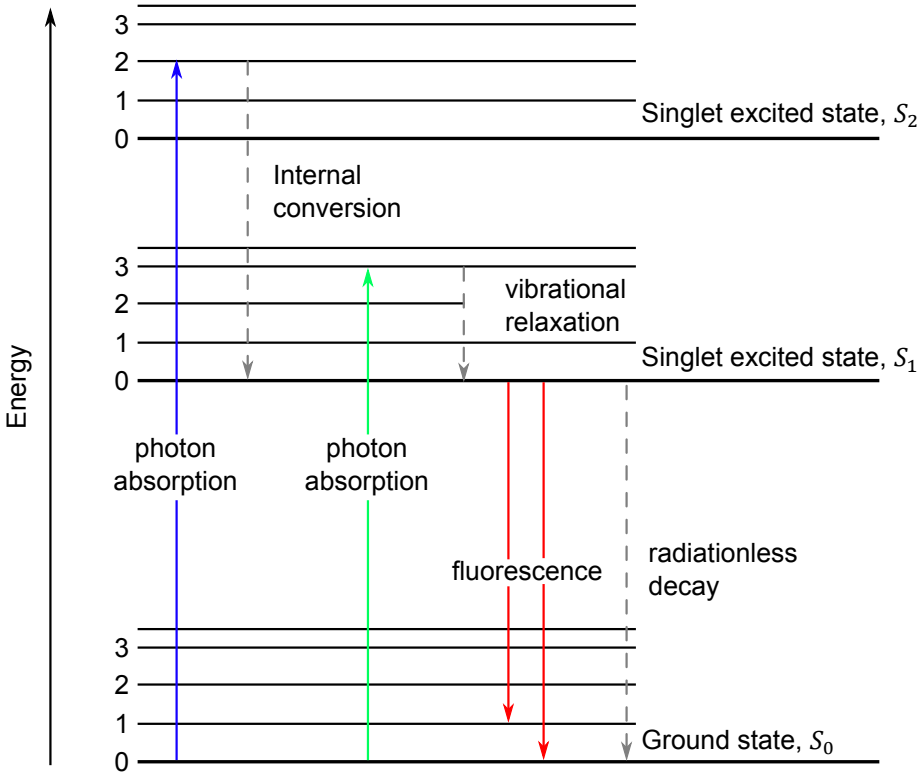

Figure 3.1: Jablonski diagram
describes the fluorescence process, including non-radiative effects. The numbers indicate vibrational levels within the electronics states S_0, S_1 and higher. Picture based on the discussion by Lakowicz [18].

leading to a photon emission. One usually estimates it macroscopically by using

$$q = \frac{\text{photons emitted}}{\text{photons absorbed}} \tag{3.1}$$

q depends on dye and environment but not on the absorbed photon's wavelength [10, 18, ;p. 3, p. 7]. A short aside, with environment we can mean: solvent, temperature, pH, contaminants etc.

The process of fluorescence is best described by molar absorption- and emission spectrums—an typical example can be found in Figure 2.3. An absorption spectrum describes how well an external light source at a given wavelength is able to cause fluorescence. Emission spectrums describe the likelihood of a photon emission for a wavelength. The spectrums' peaks are determined by the structure of the first singlet state S_1. Emissions spectrums depend on dye and environment and not on the absorbed photon's wavelength [10, 18, p3; p. 7-9]. A photon emission more energetic than the absorbed may occur if there are many populated vibration levels in S_0 present or if thermal energy is added to the system [8, p. 8]. Therefore, an overlap in absorption and emission spectrum is permissible and not a violation of energy conservation.

3.1.1. Applications

Fluorophores alter photon wavelength and are sensitive to molecular environments, which are attractive properties in practical applications. Some examples pertaining to fluorescent layers are: measurement techniques [30], dyes to turn blue-LEDs into white-LEDs [21], bio photonics [20], yield-enhancing coatings on green-houses [4], and the imaging of liquid film heights [11, 14]. Effective modelling of such layers is useful.

3.1.2. The difficulties in modelling

The radiative behaviour of a single fluorophore is easily described by its spectrums and quantum yield: it are material properties. However, macro-scale modelling—called fluorescent radiative transport—

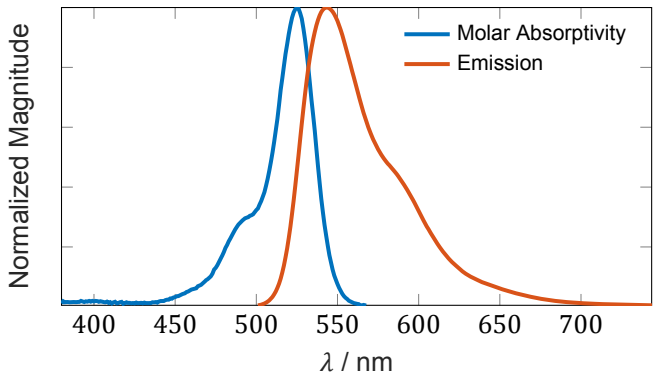

Figure 3.2: Exemplary normalized spectra of absorption and emission. The dye absorbs at shorter wavelengths and emits at longer ones. An overlap between both spectrums is a common occurrence.

of domains with a large number of molecules is complicated. Radiative transport is 6-dimensional in nature: imagine using a torch to illuminate a room. The position in the room requires three coordinates. The direction at which you point the torch needs 2-coordinates: probably a polar and azimuthal angle. The sixth and final dimension is a description of the emission spectrum, or colour of the torchlight. Photon packets travel from a source to a sink and carry the history of their trajectory: absorption events, interaction with scatterers, reflective surfaces. Consequently, a local light flux is aptly influenced by the global system behaviour. Fluorophores worsen the problem by altering wavelengths and acting as a local point source. Hence, the modelling of fluorescent radiative transfer is difficult.
A phenomenon unique to fluorophores is of special interest in modelling. Photons can get re-absorbed and re-emitted multiple times—a process called the fluorescent cascade [29, 40]. This happens if one or more dyes have overlapping emission and absorption spectrums, as depicted in Figure 3.2. A photon might have multiple up-and-down wavelengths changes before leaving the domain or getting quenched. In turn, fluxes between different wavelengths get very complicated. Cascading happens when the photons can travel for long distances through a domain with high dye concentration. The dyes must have significant spectral overlap and a large quantum yield to prevent quenching.

3.1.3. Modelling methods in literature

The most accurate, but computationally expensive, modelling approach is to apply the Monte Carlo method [5, 17, 40]; it is not a solution to the governing equation, but a simulation of large numbers of photon packages inside the domain. It is a stochastic method where pseudo random numbers determine the chance a package undergoes physical phenomena such as absorption and emission. When enough packages are simulated, the model converges to the macroscopic behaviour of the system.

Another modelling strategy is to use various discretization methods to solve the governing equation: the so-called Fluorescent Radiative Transfer Equation (FRET). Of course, discretization of 3 spatial, 2 directional, and 1 spectral dimension leads to very large sets of equations. To moderate that problem, many studies concentrate on domains were some dimensions are irrelevant. Often, this means analysing a single layer or a stack of layers, where one only the depth coordinate and the out-of-plane direction angle matter—Figure 3.3 shows an example for such a single layer. The in-plane flux variations are irrelevant, so 2 positional, and one directional coordinate do not matter; discretisation is much easier now. We call such a system plane-parallel [28, p. 2].
The adding-doubling is a method specifically intended for layer stacks of homogeneous, parallel plane media; it was successfully applied with a 600 computation time reduction compared to Monte Carlo by [19], where they studied a single dye in a scattering domain. The difference between the Monte Carlo and the adding-doubling methods was less than 0.5%. A similar approach for re-absorption was implemented with a discrete ordinates method [21], and achieved 7.6% maximal error compared to the measured spectrum of a scattering, planar, single-phosphor plate. It has the drawback of solving for the spectrum from short to long wavelengths, and thus ignoring re-emissions at ones shorter than

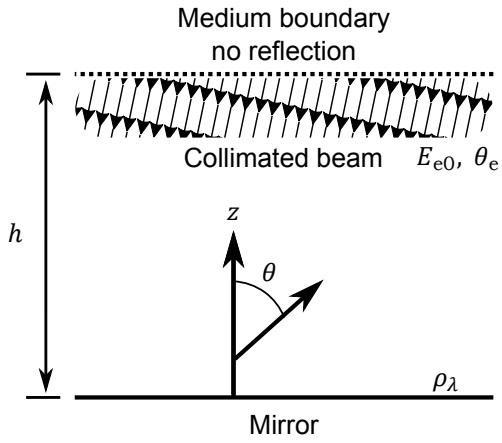

Figure 3.3: plane-parallel medium with thickness h on a flat mirror with reflectivity ρ_λ. Collimated beam with at the top boundary with an angle of θ_e and radiance of E_{e0}.

the excitation wavelength. Thence, a fluorescent cascade solution is impossible. On the contrary, a mathematical particle method solved the complete fluorescent cascade for multiple dyes at the cost of trial-and-error damping and time-step tuning [25]. A spherical harmonics approach was applied to a strongly scattering, single-dye, plane medium, it modelled a fluorescent cascade and was able to reproduce qualitative findings from other literature [29]. Likewise, a powerful and flexible method for multiple, scattering layers was developed by [20], However, it is unable to account for a cascade.

3.1.4. A new modelling approach

This work concentrates on non-scattering, fluorescent radiative transport in a plane-parallel layer on top of a mirror. The new, main assumption is that for many practical systems, the fluorescent cascade is limited to only the first 2 generations of fluorescent photons. Then the governing equation can be solved analytically by the integrating factor method. The method is implemented in the MATLAB Symbolic Toolbox, a computer algebra system, with help from some custom integration identities. Solutions were verified against practical experiments and Monte Carlo simulations. The solution offers a fast way to calculate the radiance spectrum at any point inside the domain for an arbitrary number of fluorophores.

3.2. Fluorescent Radiative Transfer Equation

Radiative transport needs three spatial, two directional, and one spectral coordinates. The most general quantity to describe it is radiance, L. Its definition—see Figure 3.4—is the photon flux density per unit projected surface, and per unit solid angle incident on, passing through, or emerging in a specified direction from a specified point in a specified surface with units q s^{-1} sr^{-1} m^{-2} [22, p. 11]. The defining equation in spherical coordinates is

$$L = \frac{\mathrm{d}^2\Phi}{\mathrm{d}\omega \mathrm{d}s_0 \cos(\theta)}$$

The surface s_0 is specified by its location; this takes care of the three spatial coordinates. The projected surface, $\mathrm{d}s = \mathrm{d}s_0 \cos(\theta)$, stems from the fact that the effective area photons can pass through decreases when they are at an angle with that surface: imagine looking on a square window at a very steep angle, it will appear to you like a thin rectangle. The element of flux goes into a unit of solid angle $\mathrm{d}\omega$ at angles ϕ and θ with the surface's normal; this takes care of the directional nature of radiative transport. Geometrical dimensions are not enough, all our quantities are spectral: they depend on the wavelength of the photons. Include this last dimension by adding subscript λ to obtain L_λ. We define the spectral quantities to be at a small waveband centred around λ. That is, wavelengths are discretized because material data is often in the form of look-up tables.

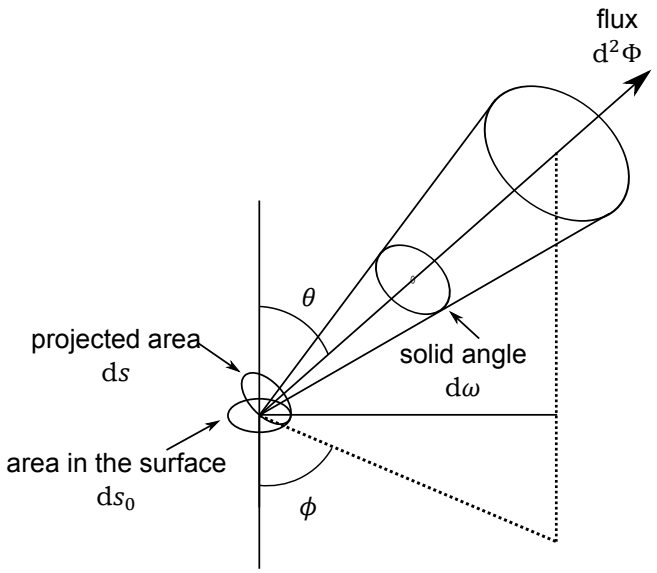

Figure 3.4: The geometry of radiance in spherical coordinates. Redrawn from [22, p. 12]

One of the fundamental equations in radiative transport is the attenuation of L_λ along a short path length l

$$\frac{\mathrm{d}L_\lambda}{\mathrm{d}l} = -\alpha_\lambda L_\lambda \tag{3.2}$$

Where α_λ is the absorptivity in m^{-1}. This differential equation has a well-known solution: the Lambert-Beer law

$$L_\lambda(l) = L_\lambda(0)\,\mathrm{e}^{-\alpha_\lambda l} \tag{3.3}$$

The much more complicated FRTE can be conceptually understood in terms of the Lambert-Beer law and the differential equation. It is a well-established equation [15, 16, 40] describing the transport of photons or energy in a medium—for a full derivation see appendix B.1.

Consider a homogeneous, plane-parallel system—see Figure 3.3—where L only depends on position z and direction θ. Inside the medium, N different fluorophores partake in a stationary radiation process, then the FRTE is given by

$$\cos(\theta)\,\frac{\partial L_\lambda(z,\theta)}{\partial z} = -\alpha_{\mathrm{m}\lambda} L_\lambda(z,\theta) + \sum_{k=1}^{N} \alpha_{\mathrm{f}_k\lambda} L_\lambda(z,\theta) + S_\lambda \tag{3.4}$$

Essentially, it is the same equation leading to the Lambert-Beer law, but with an extra source term S_λ. A infinitesimal small path length is now defined by $\mathrm{d}l = \partial z \,/\, \cos(\theta)$. L_λ is now attenuated by the medium it is traversing through, which is captured by absorptivity $\alpha_{\mathrm{m}_\lambda}$. Besides medium absorption losses, there are N fluorescent dyes present that add their absorption via $\alpha_{\mathrm{f}_k\lambda}$. Their absorptivity is the product of the molar absorptivity, a material property, and the molar concentration: $\alpha_\lambda = a_\lambda\, c$.

Source term S_λ adds extra photons along the path, which is initiated by the absorption and subsequent fluorescent emissions of the dyes. We know that the absorption process is described by differential equation 3.2. The emission process then adds the absorbed photons back into the medium, therefore flip the equation's sign, and multiply with an "re-distribution efficiency" to define the source term

$$S_\lambda = \frac{1}{4\pi} \sum_{k=1}^{N} q_{\mathrm{f_k}\lambda} \sum_{\lambda'} \alpha_{\mathrm{f_k}\lambda'} \int_\omega L_{\lambda'}(z,\theta')\,\mathrm{d}\omega \tag{3.5}$$

First, a small volume element absorbs photons from all directions, which is captured by the integral over the full solid angle ω and the absorptivity. This is done over all possible wavelengths λ' at which the dyes are able to absorb. Second, the probability of an fluorescent emission following absorption is given by the spectral quantum yield

$$q_{\mathrm{f_k}\lambda} = q_{\mathrm{k}} \bar{\epsilon}_{\mathrm{k},\lambda} \tag{3.6}$$

q_{k} is the "regular" quantum yield for a fluorophore: the mean chance of a fluorescent emission after a photon absorption. $\bar{\epsilon}_\lambda$ is a fluorophore's emission spectrum normalized such that the area under the curve equals 1. $\bar{\epsilon}_\lambda$ behaves, essentially, as a probability density function for a photon emission to occur at λ. Finally, fluorescent photons are radiated-out evenly in all directions, therefore, normalize the density by 4π, which is the solid angle of the sphere surrounding a small control volume.
For plane-parallel systems, a solid angle simplification can be done. The definition of ω in spherical coordinates is

$$\mathrm{d}\omega = \sin(\theta)\,\mathrm{d}\theta\,\mathrm{d}\phi$$

Since the system is plane-parallel, the azimuthal angle ϕ is irrelevant. Therefore, simplify S_λ

$$\begin{aligned} S_\lambda &= \frac{1}{4\pi} \sum_{k=1}^{N} q_{\mathrm{f_k}\lambda} \sum_{\lambda'} \alpha_{\mathrm{f_k}\lambda'} \int_0^{2\pi} \int_0^{\pi} L_{\lambda'}(z,\theta') \sin(\theta')\,\mathrm{d}\theta'\,\mathrm{d}\phi' \\ &= \frac{1}{2} \sum_{k=1}^{N} q_{\mathrm{f_k}\lambda} \sum_{\lambda'} \alpha_{\mathrm{f_k}\lambda'} \int_0^{\pi} L_{\lambda'}(z,\theta') \sin(\theta')\,\mathrm{d}\theta' \end{aligned}$$

Substitute back in equation 3.4 to obtain the full FRTE

$$\cos(\theta) \frac{\partial L_\lambda(z,\theta)}{\partial z} + \alpha_{\mathrm{m}\lambda} L_\lambda(z,\theta) + \sum_{k=1}^{N} \alpha_{\mathrm{f_k}\lambda} L_\lambda(z,\theta) = \underbrace{\sum_{k=1}^{N} \frac{q_{\mathrm{f_k}\lambda}}{2} \sum_{\lambda'} \alpha_{\mathrm{f_k}\lambda'} \int_0^{\pi} L_{\lambda'}(z,\theta') \sin(\theta')\,\mathrm{d}\theta'}_{S_\lambda} \tag{3.7}$$

3.2.1. Distinct forms of the FRTE

The FRTE can take 3 distinct forms for different wavelengths ranges, which is best explained by an example. Look at the hypothetical absorption and emission spectrums of figure 3.2 and assume no medium absorption losses. For λ <500 nm there is only absorption and the source-term will disappear, unless an external light source is present. Between 500 nm and 560 nm there is both absorption and fluorescent emission. It is this exact area where fluorescent cascade takes place. Beyond 560 nm, there is pure emission, so the absorption term left of the $=$ sign vanishes.

3.2.2. Extra assumptions

The FRTE can break down under some peculiar conditions that might not directly be obvious during experimentation or modelling

- The fluorescent process takes a finite amount of time. Under strong photon irradiance, there is a significant number of fluorophores in the excited stage. Meanwhile, the fluorophores in the ground state are depleted. The fluorescent emission now shows a non-linearity in light source irradiance [27]. This effect is not considered here.

- There are no concentration dependent quenching mechanisms [8, p. 28], nor are there non-fluorescent energy exchange mechanisms between the fluorophores. A poignant example would be Förster resonance energy transfer: a radiation-less energy exchange between donor and acceptor fluorophore; it induces an emission red-shift that in homogeneous media has a much earlier onset than predicted from classic theory [6].

- Fluorophores can break down under high-intensity illumination. A process called photobleaching [10, p. 3]

3.2.3. Boundary conditions

See Figure 3.3, a slab of thickness h is deposited on a flat mirror surface with spectral reflectivity ρ_λ. The medium boundary at h has negligible reflection. The z-coordinate axis is perpendicular to both the mirror and medium boundary surface. To excite the fluorophores, use a tightly-collimated, monochromatic light beam entering the medium at an angle θ_e, wavelength λ_e and an irradiance of $E_{\mathrm{e}0}$. E is the photon flux density passing through the area $\mathrm{d}s$ [39, p. 24] in $\mathrm{q\,s^{-1}\,m^{-2}}$. A practical example for E could be all the photons passing through a pinhole. The fundamental relation between radiance and irradiance is [22, p. 16]

$$E = \int_\omega L\cos(\theta)\mathrm{d}\omega$$

A collimated beam is a theoretical but useful construct that can help us simplify the source term in the FRTE. A collimated beam is a photon flux with no angular spread, therefore it cannot subtend a finite solid angle $\mathrm{d}\omega$ at all. The relation between L and E would break down and there is no sensible "mathematical" definition of an radiance L. Likewise, the source term S_λ in equation 3.7 would be undefined for the same reason. However, think of what the source term tries to represent: a capturing of a number of photons and their subsequent conversion. By heuristics, define now the source term simplification as

$$S_\lambda = \sum_{k=1}^{N} \frac{q_{\mathrm{f_k}\lambda}\alpha_{\mathrm{f_k}\lambda_\mathrm{e}}}{4\pi} E(z) \quad \text{for collimated beams} \tag{3.8}$$

With $E(z)$ the solution to irradiance field in the medium, and 4π the solid angle of the spherical radiation pattern.

3.3. Solving the fluorescent radiative equation

The plane-parallel FRTE 3.7 is made difficult by the fluorescent cascade: there is a coupling between source term on the right hand side and the system response on the left hand side; the solution for L_λ pops-up at both sides of the equation. Repeated re-emission and re-absorption means wavelengths change, and thus the solution has to be found simultaneously for all λ.

Break this self-coupling by assuming that for many systems multiple re-emissions and re-absorption events are rare. There are only two generations of fluorescent photons that contribute. The direct generation is the one driven by the beam of excitation light and the indirect one is driven by partial absorption of the direct generation. This means that a chain of three equations has to be solved where the solution of the first is the input to the source term of the next generation. The three equations are: firstly, the equation describing excitation light of the collimated beam; secondly, the direct fluorophore photons; thirdly, there are the indirect emissions arising from the absorption of the first fluorophore light. The final solution for the fluorescent light is then sum of the direct and indirect solutions for all wavelengths and fluorophores. To wit, the simplified FRTE is

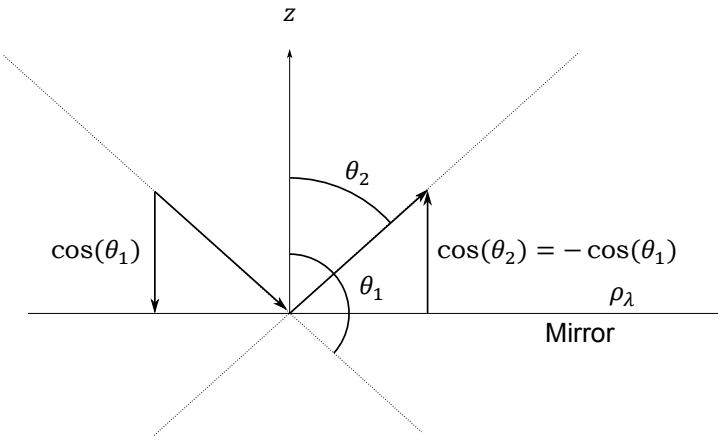

Figure 3.5: Reflection is the inversion of a ray's z-direction cosine

$$\cos(\theta)\frac{\partial L_{\lambda,\mathrm{g}+1}}{\partial z}+\alpha_{\mathrm{m}_\lambda}L_{\lambda,\mathrm{g}+1}(z,\theta)+\sum_{k=1}^{N}\alpha_{\mathrm{f}_k\lambda}L_{\lambda,\mathrm{g}+1}(z,\theta)=\underbrace{\sum_{k=1}^{N}\frac{q_{\mathrm{f}_k\lambda}}{2}\sum_{\lambda'}\alpha_{\mathrm{f}_k\lambda'}\int_0^{\pi}L_{\lambda',\mathrm{g}}(z,\theta')\sin(\theta')\,\mathrm{d}\theta'}_{S_\lambda} \tag{3.9}$$

With g the generation index. This only works for systems were photons can escape the medium before a significant third generation can form. To predict beforehand, several detrimental aspects should be analysed in combination: large domains, high dye concentration, quantum yields near unity, and a significant overlap between emission and absorption spectra. As it will turn out, we can check the 2-generation assumption by inspecting the solutions.

3.3.1. A general solution method for the FRTE

Inspect the FRTE (equation 3.9). See that it can be written in the following form, ignoring subscript λ

$$\frac{\mathrm{d}L(z,\theta)}{\mathrm{d}z}+p(z,\theta)\,L(z,\theta)=q(z,\theta) \tag{3.10}$$

A common solution method to these types of ordinary differential equations is the integrating factor method, defined as

$$\begin{aligned} L_{\mathrm{p}}(z,\theta)&=\underbrace{\mu^{-1}(z,\theta)\int\mu(z,\theta)\,q(z,\theta)\,\mathrm{d}z}_{L_{\mathrm{g}}(z,\theta)}+C\mu^{-1}(z,\theta)\\ \mu(z,\theta)&=\mathrm{e}^{\int p(z,\theta)\,\mathrm{d}z}\end{aligned} \tag{3.11}$$

Where L_{p} is the particular solution, L_{g} the general solution, C the integration coefficient and μ the integrating factor.

The domain has two distinct boundaries: a mirror and a non-reflecting layer. By intuition, the upward going radiation must have a different character than the downward one: first, reflections are added to the upward terms; second, it is likely that most of the photons are produced at the top part where the light source's irradiance comes in, so most upward photons escape quickly while downward photons go into the layer to make further contributions. Therefore, the solution can be split in upward and downward direction. To wit, define now two sets of polar angles, θ so we can differentiate between the

two different *particular* solutions

$$\begin{aligned} \Theta_{\mathrm{u}} &: \left[0,\, \frac{\pi}{2}\right] \\ \Theta_{\mathrm{d}} &: \left[\frac{\pi}{2},\, \pi\right] \end{aligned} \tag{3.12}$$

Boundary conditions are split. At the upper-boundary, there is no fluorescent light entering the layer. Therefore, the downward boundary condition and solution are

$$\begin{aligned} L_{\mathrm{p}}\left(h, \Theta_{\mathrm{d}}\right) &= 0 \\ C_{\mathrm{d}} &= -\mu\left(h\right) L_{\mathrm{g}}\left(h, \Theta_{\mathrm{d}}\right) \\ L_{\mathrm{p}}\left(z, \Theta_{\mathrm{d}}\right) &= L_{\mathrm{g}}\left(z, \Theta_{\mathrm{d}}\right) - \mu\left(h, \Theta_{\mathrm{d}}\right) L_{\mathrm{g}}\left(h, \Theta_{\mathrm{d}}\right) \mu^{-1}\left(z, \Theta_{\mathrm{d}}\right) \end{aligned} \tag{3.13}$$

At the mirror boundary, the downward going light, $L_{\mathrm{p}}(z, \Theta_{\mathrm{d}})$, reflects. The strength of reflection depends on ρ. The direction change in θ follows from basic physics: specular reflection is a depth-inversion—angle of incidence is angle of reflection. Adding this effect to the solution is surprisingly easy. As it turns out, all solutions found included direction cosines, which all derive from the cosine term of the FRTE—equation 3.7. A reflection is equivalent to a direction-cosine sign change—see Figure 3.5. Consequently, define $\mathcal{R}\{:\}$ as the transform that changes a function's direction cosines by $\cos\left(\theta\right) \rightarrow -\cos\left(\theta\right)$. The boundary condition at the mirror is then

$$L_{\mathrm{p}}\left(0, \Theta_{\mathrm{u}}\right) = \rho\, \mathcal{R}\{\, L_{\mathrm{p}}\left(0,\, \Theta_{\mathrm{d}}\right)\} \tag{3.14}$$

Solve for this condition by plugging it in 3.11

$$\begin{aligned} L_{\mathrm{g}}\left(0, \Theta_{\mathrm{u}}\right) + C_{\mathrm{u}}\, \mu^{-1}\left(0, \Theta_{\mathrm{u}}\right) &= \rho\, \mathcal{R}\{\, L_{\mathrm{g}}\left(0,\, \Theta_{\mathrm{d}}\right) - L_{\mathrm{g}}\left(h,\, \Theta_{\mathrm{d}}\right) \mu\left(h, \Theta_{\mathrm{d}}\right) \mu^{-1}\left(0, \Theta_{\mathrm{d}}\right)\} \\ L_{\mathrm{g}}\left(0, \Theta_{\mathrm{u}}\right) + C_{\mathrm{u}} &= \rho\, \mathcal{R}\{\, L_{\mathrm{g}}\left(0,\, \Theta_{\mathrm{d}}\right) - L_{\mathrm{g}}\left(h,\, \Theta_{\mathrm{d}}\right) \mu\left(h, \Theta_{\mathrm{d}}\right)\} \\ C_{\mathrm{u}} &= \rho\, \mathcal{R}\{\, L_{\mathrm{g}}\left(0,\, \Theta_{\mathrm{d}}\right) - L_{\mathrm{g}}\left(h,\, \Theta_{\mathrm{d}}\right) \mu\left(h, \Theta_{\mathrm{d}}\right)\} - L_{\mathrm{g}}\left(0, \Theta_{\mathrm{u}}\right) \end{aligned} \tag{3.15}$$

Substitute the integration constant into 3.11: this gives the final particular solution

$$L_{\mathrm{p}}\left(z, \Theta_{\mathrm{u}}\right) = L_{\mathrm{g}}\left(z, \Theta_{\mathrm{u}}\right) + \left[\, \rho\, \mathcal{R}\{\, L_{\mathrm{g}}\left(0,\, \Theta_{\mathrm{d}}\right) - L_{\mathrm{g}}\left(h,\, \Theta_{\mathrm{d}}\right) \mu\left(h, \Theta_{\mathrm{d}}\right)\} - L_{\mathrm{g}}\left(0, \Theta_{\mathrm{u}}\right) \right] \mu^{-1}\left(z, \Theta_{\mathrm{u}}\right) \tag{3.16}$$

This solution scheme can be implemented in a computer algebra system with help from some custom integration identities to find expressions for L_{g} and $q(z, \theta)$, the latter is essentially the source term S_{λ}. Some of these are difficult to derive. However, when found an implemented, a simple conversion to numeric functions gives a swift way to calculate the radiative transfer in the medium.

There are three distinct forms of the FRTE. The method solved for the cascade regime. The indirect generation solution in that form is not always directly applicable to the two other regimes of no absorption or no source term. Without absorption can be found from the cascade solution by taking a limit to 0 for the absorptivity left of $=$ in equation 3.9. When there is no source term there are no photons emitted. Hence, we have the zero solution. All solutions, their limits, and integration identities can be found in the appendices: B.4, B.5, B.6, B.8, B.7, and B.9.

3.4. Method

Proof that the analytic solution works is necessary. Verification of the model was done by checking for implementation errors, see appendix B.10. A concurrent test was done with a Monte Carlo method to see if for the same material spectra and geometry, they produce the same output. Another aspect checked was the 2-generation limit concept by investigating the number of absorption events. A measurement setup was built to investigate the emission spectrum for a water layer with two dissolved fluorophores.

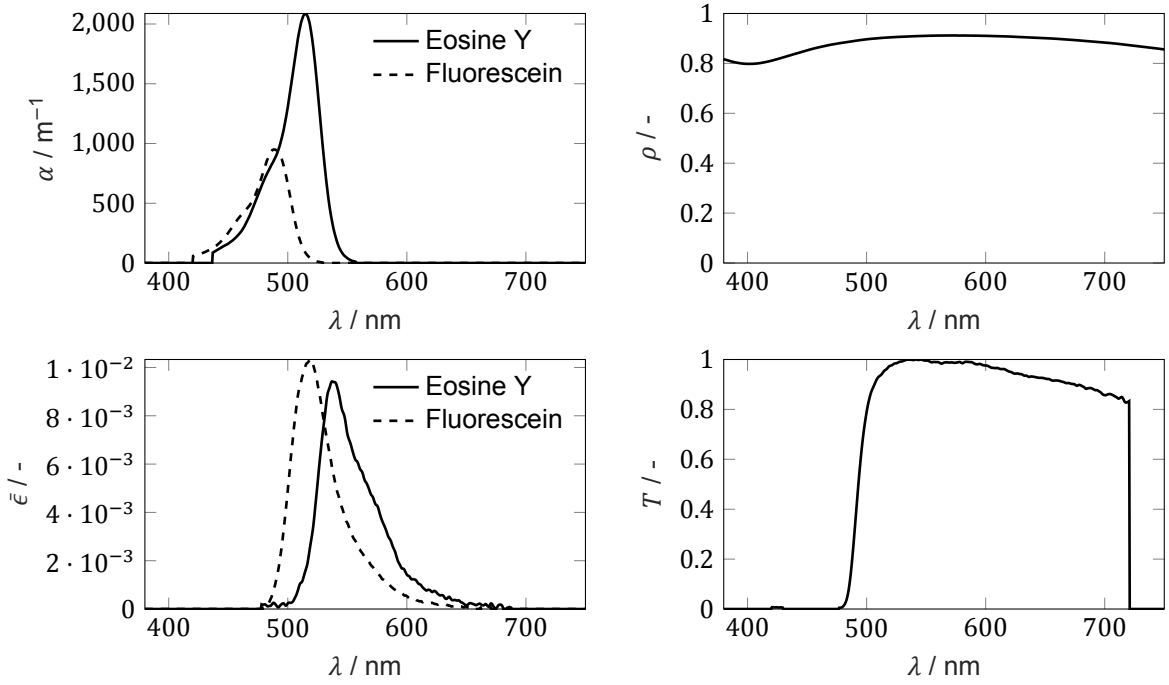

Figure 3.6: All spectrums used in analytic and Monte Carlo models. α absorptivity, ρ reflectivity, $\bar{\epsilon}$ normalized emissivity, T filter and fibre transmission.

3.4.1. Initial analysis and material spectrums

To provide the MC and analytic model with material spectra, two fluorophoric dyes were chosen, and their material properties investigated. They are Fluorescein sodium salt—purity unknown—and Eosin Y disodium salt—purity>85%—both acquired from Sigma-Aldrich. They were dissolved in water with pH of 11—sodium hydroxide of 99% purity—also obtained from Sigma-Aldrich. A pH of 11 makes for the best quantum yields and creates spectra with well-defined peaks [33]. The water was filtered with a Puralab Flex.

Spectrums were obtained with an USB4000 spectrometer calibrated by a HL-3P-CAL tungsten source from Ocean Optics. The spectrometer used an optical fibre as a source, and if necessary, its numerical aperture was reduced to 0.0371 via attachment of a black tube with a pinhole. As a light source, a XPE - Starboard blue LED ($\lambda_{\max}$ =450 nm, $\Delta\lambda \pm 20$ nm) was used with an Ledil Lisa2-Clip16-XP lens to focus the beam—full width at half maximum angle of $\pm 8°$. A long pass filter with an measured half-transmission at 493 nm was used to filter-out excitation light from the LED.

Material properties were measured at 741 different wavelengths. Before measuring them, the transmissions of filter, fibre-optics and dark spectrum were obtained.

Fluorescein emission spectrum measurements were done by placing 0.02%wt dissolved fluorescein between two thin glass plates to create a very thin layer without self-absorption—in very thin layers, the path lengths of the fluorescent photons are too short for re-absorption to occur. The LED-light shone nearly perpendicularly at the layer while a perpendicular optical fibre with black tube recorded the spectrum. The light shone away from the tube opening. Measurements were conducted in a blacked-out, highly light absorptive enclosure. The eosin spectrum was recorded by observing a drop; the finite optical-lengths in a not-so-thin drop will cause a red-shift of several nanometers. The shift was removed by literature verification from [41]. It was found that the transmission of the filter bled in the emission spectra which was not removable. This unfortunate occurrence was unavoidable, as the spectrometer was not sensitive enough for the glass-plates method.

Absorption spectrums were obtained by placing a 10 mg L^{-1} solution in a transparent, plastic cup of 10.2 mm deep and 34.0 mm in diameter. The cup was placed between a broad-source LED and the optical fibre with pinhole tube. Measurements took place in windowed room during daytime. Obtained

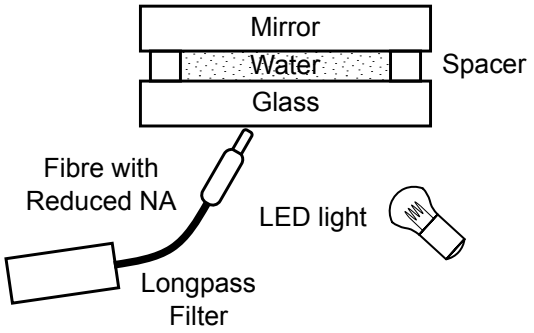

Figure 3.7: Measurement setup for model verification. Optical fibre's numerical aperture is reduced by adding a black tube with pinhole. The fibre is very close to the glass surface. LED light is far way from the glass to create a approximate collimated light source and equipped with a lens, reflector, and scatter-light reducing cone to create a well-defined beam. LED and fibre are positioned such that specular reflections on the glass are not in the fibre's numerical aperture.

spectrums agreed well with the ones found in the literature [33]. The peak, molar absorptivity for fluorescein is a_{fl} =6.6 × 10^6 L mol^{-1} m^{-1} which agreed well with literature [24]. Eosin's disagreed very much with the literature: $a_{\mathrm{ey}} = 9.0 \times 10^6$ L mol^{-1} m^{-1} versus a probable range of 1×10^7 L mol^{-1} m^{-1} to 2.2×10^7 L mol^{-1} m^{-1} [1, 33]—not directly given in the literature: requires some estimation from plots. A decision was made to trust the data from literature. a_{ey} was tuned to make model and a couple of measurements to agree. Then, the model was compared with the remaining measurements to see if it had any predictive power.

	Fluorescein	Eosin Y
q	0.85 [41]	0.2 [41]
a_{peak}	76.0e5 [24]	1×10^7 L mol^{-1} m^{-1} to 2.2×10^7 L mol^{-1} m^{-1} [1, 33]

To prevent concentration quenching or Förster resonance energy transfer, a series of solutions with different concentrations were made—0.125 mmol mol^{-1}, 0.25 mmol mol^{-1} and 0.5 mmol mol^{-1}. Emission spectrums were repeatedly measured for a very thin layers sandwiched between glass plates. The highest concentration showed a distinct red shift, the middle one was uncertain. Therefore, 0.125 mmol L^{-1} was chosen as the right concentration.

All resulting spectra can be found in Figure 3.6.

3.4.2. Fluorescent-layer experimental setup

A simple setup was built to see if the model can accurately predict a real system, see Figure 3.7. Fluorescein and Eosin Y were dissolved in water (pH 11) with $c = 0.125$ mmol L^{-1}, 1% deviation in concentration possible, not accounting for chemical purity. Solution was put on a very flat glass disk—waviness « 1 µm, 45 mm diameter, 12 mm thick, diffuse reflective sidewalls. The choice for glass is inspired by the low angular reflectivity between water and glass—see Figure 3.8—as can be calculated by the well-known Fresnel equations. Low reflectivity at the medium boundary is an assumption in the analytic model. On the glass, metal spacers held-up a mirror—Edmund Optics Zerodur mirror, 2 inch diameter, protected aluminium coating, waviness of <32 nm. An XPE - Starboard blue LED served as a light source—$\lambda_{\mathrm{max}} = 450$ nm, waveband $\pm$20 nm. It had a Ledil Lisa2-Clip16-XP lens to focus the beam—FWHM angle of $\pm 8°$—and a black cone to reduce stray light. It was put some distance away to approximate a locally collimated beam in the water. The light source could be put at an angle which caused an θ_{e} error of $\pm 5°$ inside the water layer. The optical fibre had a pinholed black tube on top to reduce the Numerical Aperture (NA) to 0.037, it could see the radiance inside the layer at an estimated, angular error $\theta_{\mathrm{v}} = \pm 6°$. LED and fibre were put in a cross-plane position to prevent specular reflections into the NA. Not all combinations of θ_{v} and θ_{e} are possible due to blocking of irradiance light by the fibre.

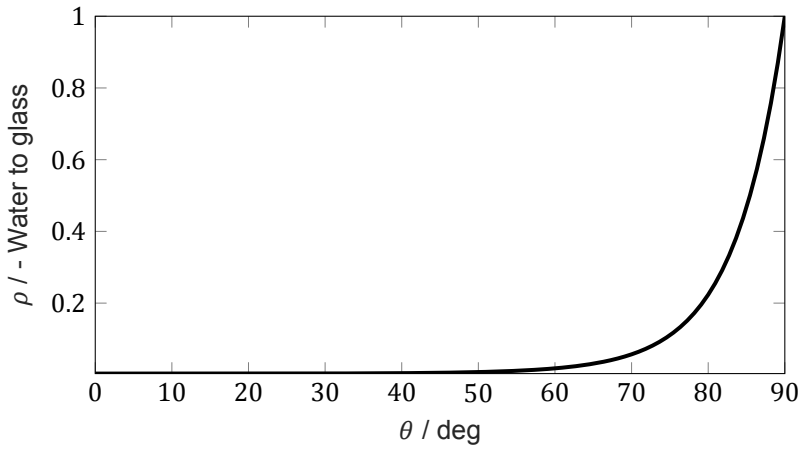

Figure 3.8: Angular reflectivity for rays on a water to glass refractive interface, as given by Fresnel Equations. Angle is between the ray, and refractive interfaces normal vector.

The following combination of layer thicknesses and viewing and irradiance angels where used. All angles are inside the water.

h ±50 µm	500	900	2000
θ_e ±5°	20	45	
θ_v ±6°	0	45	

Measurements were made over several days. Data was smoothed by a Gaussian filter—centred window of 15 samples. The comparative, analytic solution dataset was multiplied by T to add the transmission effects of the setup's filter and fibre transmission.

3.4.3. Monte Carlo method

A simple Monte Carlo model was implemented to verify the 2-generation assumption and to reproduce the output radiance spectrums from the analytic model for the same geometri and material inputs. The domain was a simple cylindrical medium with a round sensor on top, see Figure 3.9. The coordinate system flipped with respect to the analytic solution and is now centred on the sensor. The cylinders radius, r_d, was set such that the smallest view factor from any small control volume to the sensor was at least 0.01—factors obtained from [2]. This means that any part in the domain has at least a 1% change of creating a direct hit with a photon on the sensor, which makes sure all parts of the domain have a meaningful contribution to the simulation. For thick layers of $h > 400$ µm this radius was multiplied by 3 to account for intermediate absorption redirecting photon packages to the sensor. Scaling factor derived by checking for convergence. Photons are released perpendicular to the top surface. 8 different heights were investigated with $4 \cdot 10^9$ photon packages per height. The cylinder bottom is considered to have the same reflectivity as the protected aluminium, coated mirrors from Edmund Optics: the same mirror as used in practical experiments. To find the dependence on polar angle, an acceptance cone was introduced. Only the photon packages inside of the cone with half-apex angle $\theta_a = 10°$ where captured by the sensor with a radius of $r_s = 450$ µm. Polar rotation of the cone is defined by the view angle θ_v. The finite solid angle of the cone means that L can only be approximated. The model code was parallelized and ran on six cores of an Intel Core i7-9750H CPU clocked at 2.60GHz.

In the coming algorithm description, the uniform distribution $u \in [0, 1]$ is sampled. Every u is an unique realization of that distribution. A photon package simulation, see Figure 3.10, starts by setting the energy U and wavelength λ_e. The direction vector, $\hat{\mathbf{x}} =< \hat{x}, \hat{y}, \hat{z} >$, is set to be straight down. The position $\mathbf{x} =< x, y, z >$ is initialized on top of the cylinder head by sampling the radius and polar angle

$$\theta_d = 2\pi u, \quad r = r_d\sqrt{u}, \quad \mathbf{x}_0 = [r\cos(\theta_d),\, r\sin(\theta_d),\, 0]$$

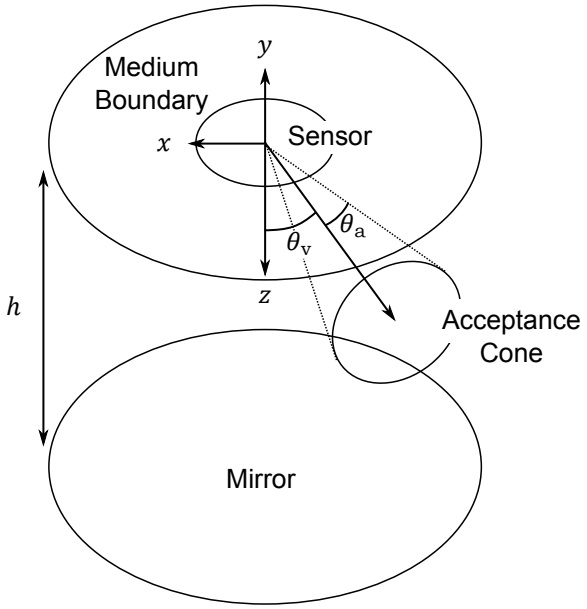

Figure 3.9: Domain for MC simulation. Coordinate systems are flipped with respect to the analytical domain

d is the distance travelled by the photonpackage. Obtain it by treating Lambert-Beer's law as a Probability Density Function (PDF), then find its Cumulative Distribution Function (CDF) and uniformly sample its inverse, to wit

$$L(d) = L(0)\mathrm{e}^{-\alpha_\lambda d}, \quad \mathrm{PDF} = \alpha_\lambda \mathrm{e}^{-\alpha_\lambda d}, \quad \mathrm{CDF} = 1 - \mathrm{e}^{-\alpha_\lambda d}, \quad d = -\frac{\ln(-u+1)}{\alpha_\lambda}$$

Update the new position by $\mathbf{x}_{\mathrm{new}} = \mathbf{x}_{\mathrm{old}} + d\hat{\mathbf{x}}$ and check if the package is still in the domain. If it is below the domain, reflection occurs, so remove some energy, update d, change the direction, and set the new position to the intersecting point with the mirror

$$U_{\mathrm{new}} = \rho_\lambda U_{\mathrm{old}}, \quad d_{\mathrm{new}} = d_{\mathrm{old}} - \frac{h - z_{\mathrm{old}}}{\hat{z}}, \quad \hat{z}_{\mathrm{new}} = -\hat{z}_{\mathrm{old}}, \quad \mathbf{x}_{\mathrm{new}} = \mathbf{x}_{\mathrm{old}} + \hat{\mathbf{x}}_{\mathrm{old}}(d_{\mathrm{old}} - d_{\mathrm{new}})$$

If the photons are above the domain, do two checks: first, did an intersection with the sensor occur and secondly, are the photons in the sensor's acceptance cone. Intersection happened if

$$t = -\frac{z}{\hat{z}}, \quad (x + \hat{x}t)^2 + (y + \hat{y}t)^2 - r_{\mathrm{s}}^2 \leq 0$$

Entry into the acceptance cone occurs if the ray's direction vector falls inside it. To check, rotate the direction vector into a coordinate system where the new, local z-axis coincides with the cone's symmetry axis. If the new z-direction is larger than cosine of θ_{a}, accept it

$$R = \begin{bmatrix} 1 & 0 & 0 \\ 0 & \cos(\theta_{\mathrm{v}}) & -\sin(\theta_{\mathrm{v}}) \\ 0 & \sin(\theta_{\mathrm{v}}) & \cos(\theta_{\mathrm{v}}) \end{bmatrix}, \quad \hat{\mathbf{x}}_{\mathrm{rot}} = R\,\hat{\mathbf{x}}, \quad \hat{z}_{\mathrm{rot}} > \cos(\theta_{\mathrm{a}})$$

Now, add U to the spectrum at λ and record the number of absorption events that happened before striking the sensor.

If after travelling distance d, the photon is in the domain, check which fluorophore absorbed it. We choose dye 1 if

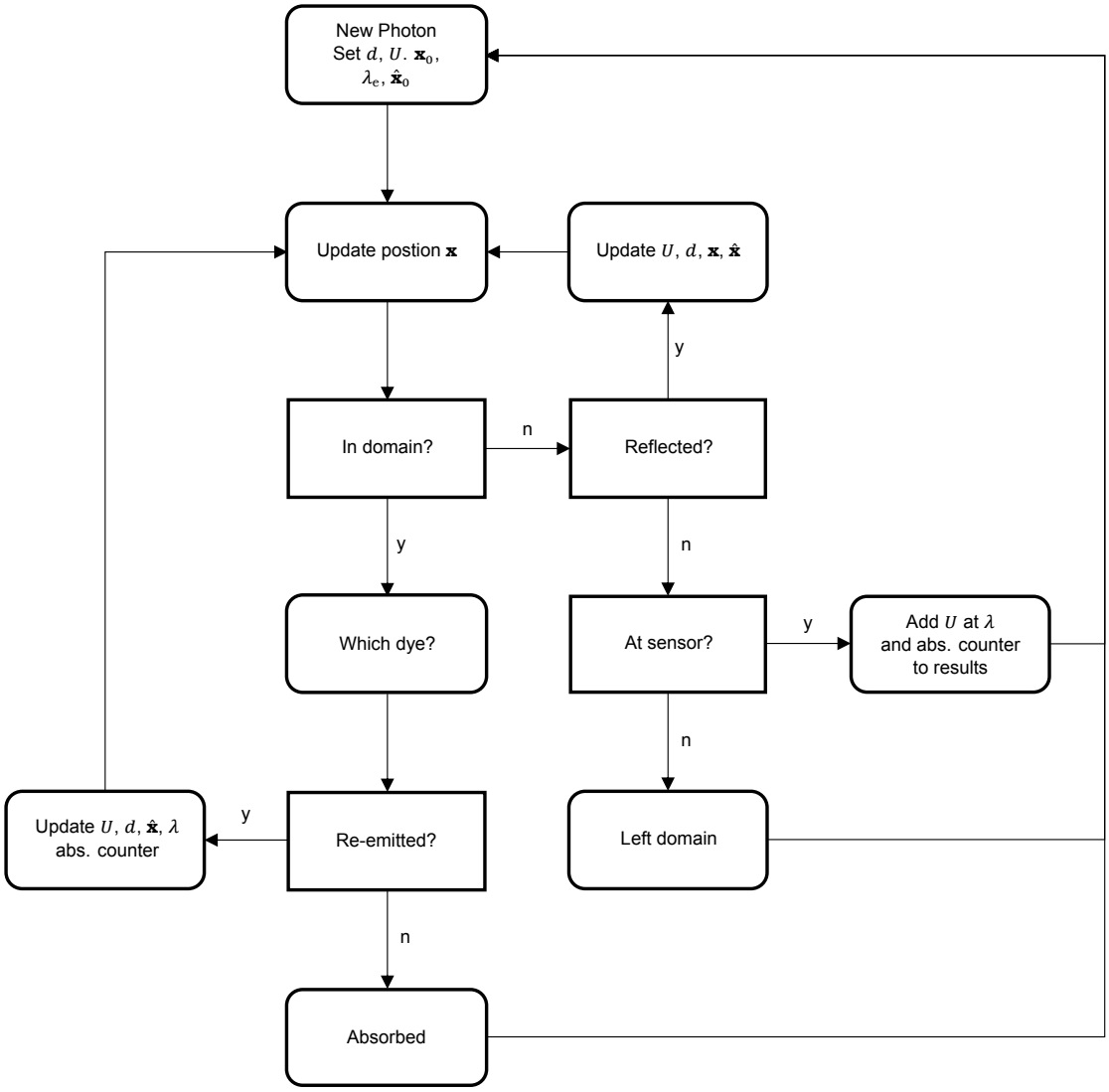

Figure 3.10: Flow chart for the Monte Carlo algorithm.

$$\frac{\alpha_{1\lambda}}{\alpha_{1\lambda} + \alpha_{2\lambda}} > u$$

and dye 2 otherwise. The chance of an absorption event without emission is determined by the quantum yield

$$q_{\text{dye}} < u$$

The photon is removed and a new one is emitted at the top of the layer, but when re-emission does happen, update λ and the number of absorption event counter by

$$\lambda_{\text{new}} = \text{CDF}_{\bar{\epsilon}}^{-1}(u) \qquad \text{abs. counter} = \text{abs. counter} + 1$$

With CDF^{-1} the inverse cumulative distribution function of the particular dye's normalized emission spectrum $\bar{\epsilon}$. Since there is no analytic inverse, a numerical inversion is needed. Then update d, and change the photons energy by

$$U_{\text{new}} = \frac{\lambda_{\text{old}}}{\lambda_{\text{new}}} U_{\text{old}},$$

Also, find the direction into which the photon is emitted by uniformly sampling on a sphere—fluorescence emits equally in all directions

$$\cos(\theta) = 1 - 2u \qquad \sin(\theta) = \sqrt{1 - \cos(\theta)^2}, \qquad \cos(\phi) = \cos(2\pi u)$$
$$\hat{x} = \sin(\theta)\cos(\phi) \qquad \hat{y} = \sin(\theta)\sin(\phi) \qquad \hat{z} = \cos(\theta)$$

This concludes the algorithm.

Several heights and viewing angles were simulated and compared to the analytic model

h / µm	20	100	200	400	800	1200	1600	2000
θ_{v} / radian	0	$\pi/8$	$\pi/4$	$3\pi/8$				

All viewing angles were checked simultaneously within each h run. After simulation, data was smoothed with a Gaussian filter—centred window of 15 samples — to remove statistical noise. Then it was transformed from the energy rate to photon rate domain and normalized to 1 for comparison with the analytic solution of the FRTE.

3.5. Results

3.5.1. Measurements

The comparison between the analytic model and the measurement can be found in Figure 3.11. The peak molar absorptivity was heuristically tuned to $a_{\text{peak}} = 1.67 \times 10^7$ L mol^{-1} m^{-1} by comparing analytic results and measurements of Figure 3.11a. This coefficient was then used to create the analytic solution for the 3 other figures. Both datasets agreed upon the existence of a shoulder at 500 nm to 530 nm that shrunk in height with increasing h and θ_{v}, yet the effect of θ_{e} is negligible. The model matches peak radiance well, but overestimates energy in the shoulder; an effect that is less pronounced for greater depth, were overestimation can turn in underestimation. Deviations with respect to the analytic model can be found in table 3.1

Varying θ_{v} red-shifts the measured emission peaks, with increasing effect strength for h. Excitation angle $\theta_{\text{e}} = 20°$ shows an approximative 1 nm, 6 nm and 6 nm shift for 500 µm, 900 µm and 2000 µm. $\theta_{\text{e}} = 45°$ shows an approximative 1 nm, 4 nm and 3 nm shift for 500 µm, 900 µm and 2000 µm.

Table 3.1: Maximal radiance measurement difference with respect to the analytic model in the shoulder at 500 nm to 530 nm

Figure	Error / %	Location / nm
3.11a	23, 12, 8	509.5, 510, 510
3.11b	19, 19, 9	510, 510, 525
3.11c	26, 12, 4	509.5, 509.5, 510
3.11d	21, 5, 5	508, no peak, 510

The measured emission peak variation between different θ_e was usually negligible, exceptions are approximately 2 nm and 4 nm for $\theta_v = 0°$, $h = 900$ µm and $\theta_v = 45°$, $h = 2000$ µm.

Analytic peak wavelengths are always within 3 nm of the measured peak. There seems to be no pattern between the differences.

3.5.2. Monte Carlo

Comparisons between the analytic model and MC simulations are plotted in Figures 3.12a and 3.12b. The first figure shows the $h = 20$ µm, 100 µm, 200 µm and 400 µm for different viewing angles and a perpendicular, collimated irradiance. It has the regular domain radius. Fit between both methods is good except for 400 µm where the analytic method has more energy at the longer wavelengths. This deviation is not visible for the larger h's, but the noise increases, however. The domain radius was scaled by 3 for these depths to help convergence. All plots show a red-shift of energy by the creation of a shoulder in the 500 nm to 530 nm waveband; very thin layers such as 20 µm have an emission peak at 515.5 nm while deep layer have one at 551 nm. All but the thinnest of layers have a more pronounced shoulder at greater viewing angles. At 100 µm, the peak broadens, and for greater thicknesses, the left flank develops the shoulder. Peaks of both spectrums are matched within less than 0.5 nm. Monte Carlo spectrums show for 800 µm a repeated bump around 515 nm for all viewing angles, which is absent in the analytic solutions.

Figure 3.13 shows the generational, fraction make-up of fluorescent photon packages that arrived at the sensor. The first two generations account for more than 90% of all packages. For deeper layers, the role of latter generations increases.

The MC model took longer to run for deeper layers. A comparison between MC the analytic solution runtimes for the deepest layer and all viewing angles is

$h = 2000$ µm, all θ_v	Monte Carlo	Analytic
runtime	1.7089×10^4 s	6.9171 s

The MC model calculates all θ_v in one go, while the analytic solution requires separate runs for each one.

3.5.3. Individual Contributions to the overall radiance

Figure 3.14 shows the individual contributions of all solutions to the total radiance. For 100 µm, Fluoresceine's direct solution dominates: its peak is 6 times larger than Eosin Y's. For 2000 µm, Eosine Y's direct and indirect results have a combined photon radiance that is equal to 60 % of Fluoresceine's at the 546 nm and 547 nm peak. Fluorescein shows the shoulder effect. Eosin Y is mostly composed of its direct term, and the indirect term fed by Fluorescein photon absorption. Other contributions are vanishingly small, especially the Eosin Y to Fluorescein solution. Noise affects the data for wavelengths roughly beyond 550 nm.

3.6. Discussion

Measurements and analytic model agree well, but for the shoulder at 500 nm to 530 nm, where the model usually overestimates the energy. The shoulder is centred at the absorption peak of Eosin Y. The disagreement is likely due to uncertainty in material data. Most of it is in the spectrometer measure-

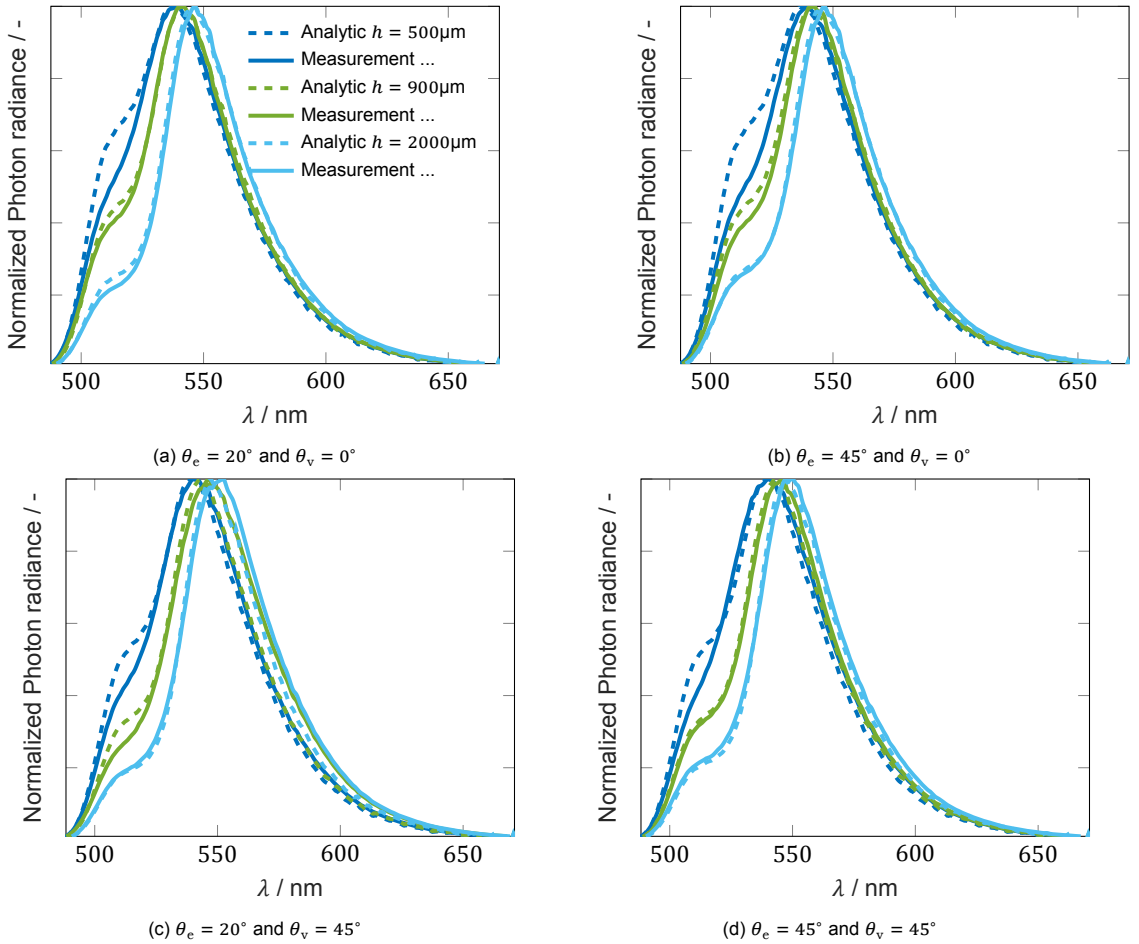

(a) $\theta_e = 20°$ and $\theta_v = 0°$

(b) $\theta_e = 45°$ and $\theta_v = 0°$

(c) $\theta_e = 20°$ and $\theta_v = 45°$

(d) $\theta_e = 45°$ and $\theta_v = 45°$

Figure 3.11: Measured and analytic emission spectrums of a parallel layer between glass and the mirror. Errors for measured data are $\theta_e \pm 5°$, $\theta_v \pm 6°$, $h \pm 50$ µm

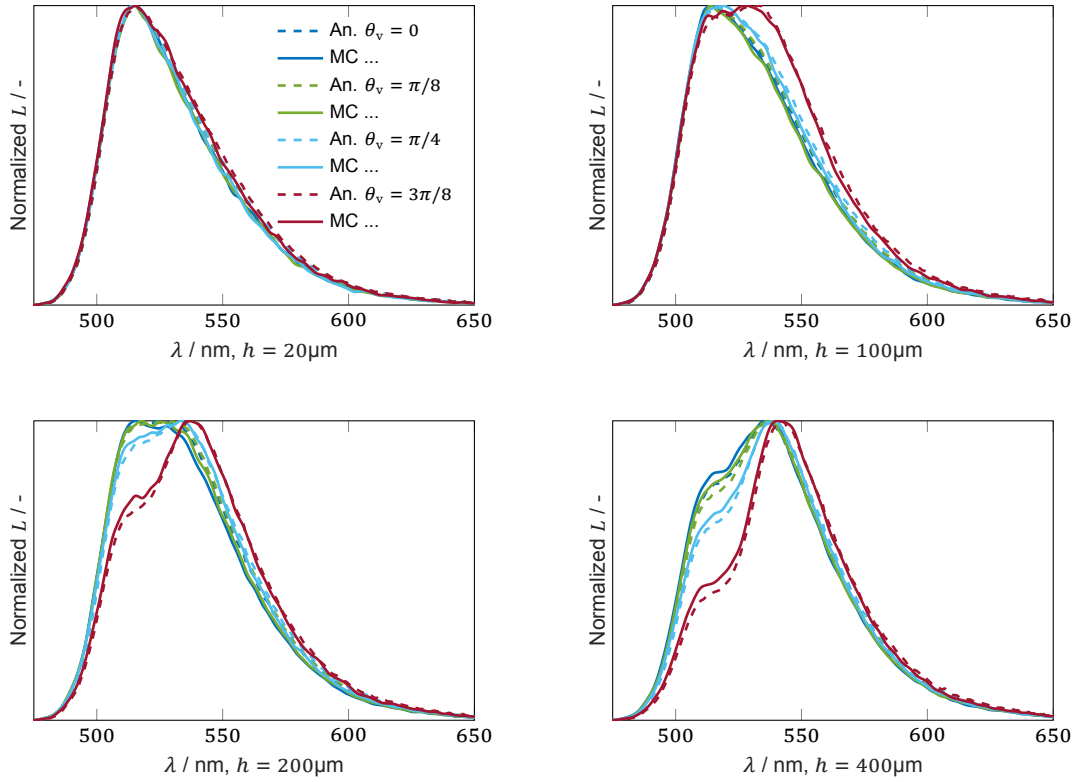

(a) Comparison between Monte Carlo simulations and analytic solution. $\theta_e = 0°$. Regular radius.

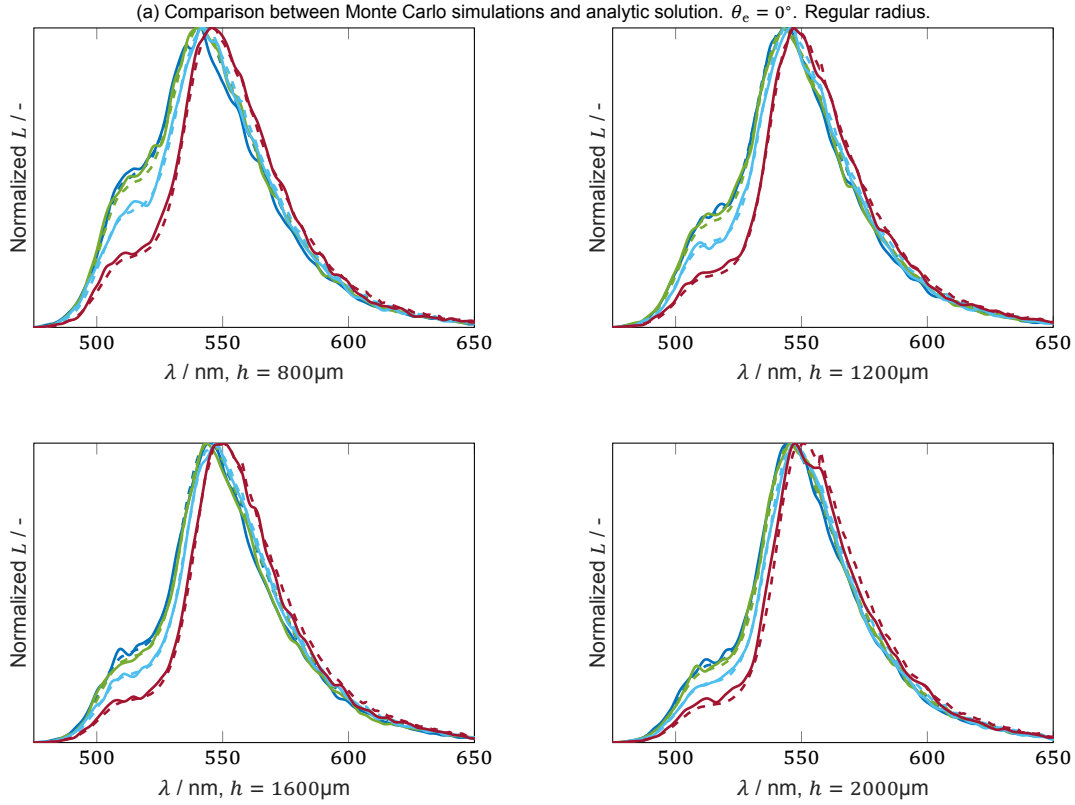

(b) Comparison between Monte Carlo simulations and analytic solution. $\theta_e = 0°$. 3 times larger radius than regular one.

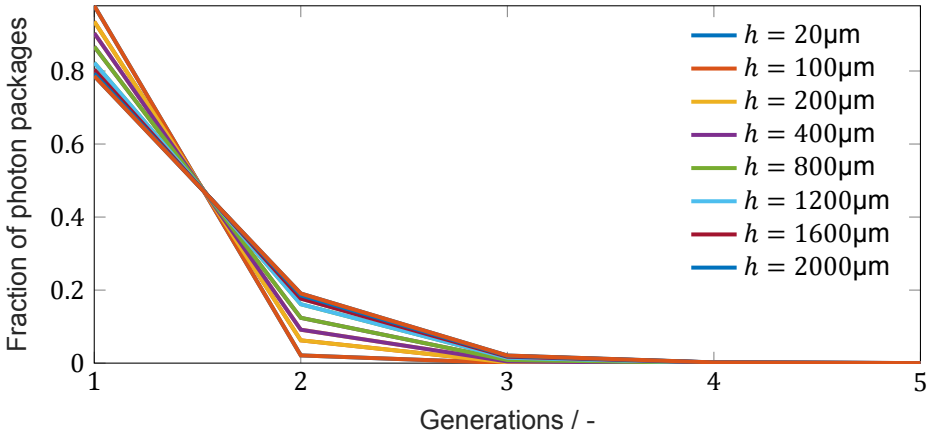

Figure 3.13: Generation fraction of all fluorescent photon packages arriving at the sensor.

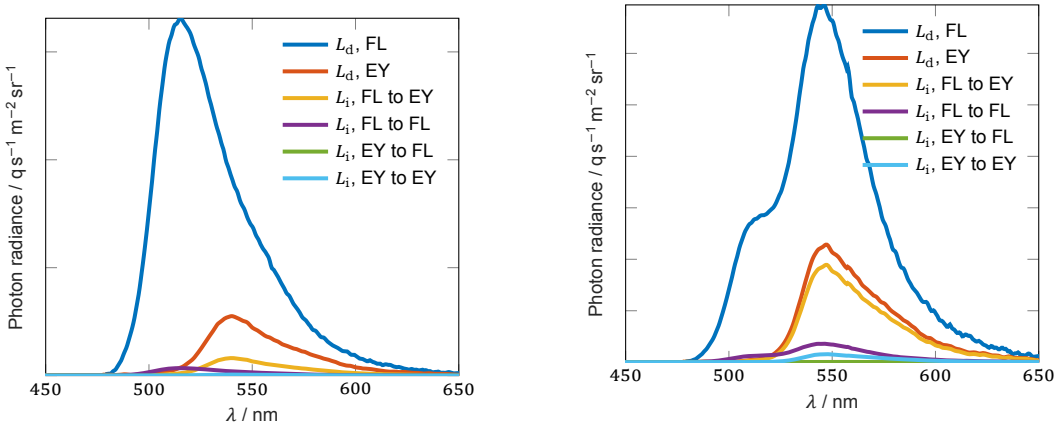

(a) 100 µm, $\theta_e = 0°$, and $\theta_v = 0°$

(b) 2000 µm, $\theta_e = 0°$, and $\theta_v = 0°$

Figure 3.14: Individual contributions of both dyes to the direct solution L_d and the indirect L_i solution. FL=Fluorescein EY=Eosine Y. Data not corrected for filter and fibre transmission T.

ment: the strong deviation between measured and literature Eosin Y's molar absorptivity. A different problem is the bleed through of fibre transmission and filter corner frequency in the emission spectra, see Figure 3.6. Other culprits are the lacking measurement conditions: measuring over multiple days under different environmental conditions, and absorption tests in a well-lit room. All are the unfortunate effect of a lack of time and resources.
A speculative cause might be that, even though minor, there are some reflection at the water-glass interface. Photons might not escape glass to the glass, whereafter they serve as a source for Eosin, and therefore enrich the peak in comparison to the shoulder.
A relatively minor effect of measurement uncertainness is the noise in the model beyond 550 nm— Figures 3.14, 3.12a, and 3.12b— which derives from measurement noise visible in Figure 3.6.
However, matching the peaks of emission is near perfect: usually a within 2 nm match, with an outlier to 3 nm. Thence, beyond the noise and shoulder, there is a very good agreement between model and measurement.

For 2000 µm layers, the emission peak at 547 nm becomes more and more pronounced, which is coincident with Eosin's emission peak at 546 nm. Meanwhile, the shoulder around 515 nm deepens, it is in this band that Eosin's absorption peak and Fluorescein's emissions peak resides. Therefore, we see that Eosin is actively absorbing Fluorescein photons. For greater viewing angles, the effective path-length photons travel increases, therefore the shoulder deepens, as Fluoresceine photons have a greater change to meet an Eosin molecule. This idea is reinforced by the split-up of the individual contributions of the dyes—Figure 3.14. For thin layers, Fluorescein with its high quantum yield, and strong absorption of excitation light dominates, while for thicker layers, the indirect solution to Eosin becomes very strong, enriching the 547 nm peak. Eosin contributes the most by absorbing fluorescein, and not so much as by emitting photons, for its quantum yield is small.

The Monte Carlo model and analytic solution show a great agreement between outputs for a great variety of h and view angles up to $3\pi/8$. Although, MC has some innate statistical noise for greater depths: the domain's radius is scaled by 3, lowering the chance of a photon reaching the sensor. The noise then creates a minor disagreement between the two. Both models capture the same physics, but MC can add more fluorescent photons beyond the first 2 generations. However, at least 90% of the photons tested for perpendicular irradiance are part of the first 2 generations, so the direct and indirect analytic solution captures the true physics well.
Individual contributions to the radiance can also show that the 2-generation assumption works. See Figure 3.14b, the Fluorescein to Fluorescein contribution is very small: photons are rarely re-absorbed and re-emitted and there is no significant fluorescent cascade. The same holds for the Eosin to Eosin contribution. If an absorption and emission spectrum overlap over a broad wavelength range and q is large, these contributions would increase significantly, and self-cascade would start. Another hint can be found in the indirect contributions between Fluorescein to Eosins: it is significant, but only for this 2000 µm thick layer, suggesting that their coupling is not that strong. For more than 2 dyes, the absence of multiple strong couplings from short to long wavelengths would be a good hint the 2-generation model holds.

The overall agreement between measured, Monte Carlo, and analytic emissions spectrums demonstrates that the model for irradiance works well. The equation derived by heuristics, 3.8, is adequate for modelling the light source exciting the layer. In general, the effect of irradiance angle θ_{e} seems small.

The analytic model offers a very fast way to calculate the emission spectrums at the top of the layer. In general, runtime reductions in the order of 1000's can be achieved with respect to the MC model. It should be noted that MC immediately returns the results for all viewing angles in one simulation, while the analytic model must run separate solution runs for each angle. If only one angle is necessary, then the current simulation could be almost 10000 times faster. In principal, the solution method can give the direct and indirect equation of all the dyes combined. Then the analytic model's run time would not depend on the number of dyes.

3.7. Conclusion

An analytic solution to the radiative transfer equation in a plane-parallel medium was derived. Derivation via computer algebra systems takes care of very difficult bookkeeping of solution. However, the derivation of identities which help find the solution is a strong upfront cost in time. Afterwards, calculating the solutions for a 2-dye system takes 1000's of times less than Monte Carlo simulation with time reductions up to 1×10^{04} are possible. Comparison between Monte Carlo method and solution show that for the same material inputs and geometry, they produce the same output. Measurements verified the solution. There was some uncertainty in material data fed to the solution however. This lead to an overestimation in the emission radiance at the location of one of the dye's absorption peaks. Better measurement conditions and equipment ought to solve this. Assuming two generations of by fluorescence produced photons for a practical system is verified by Monte Carlo simulations. By inspecting the individual contributions of all dyes to the overall emissions spectrum, we can spot a violation of the assumption.

3.8. Recommendations

Repeat the measurement with better material data to see if the shoulder overestimation disappears. Use regular fluorometer and absorption meters to obtain material data. Applied methods in the study were only used because they were time and resource viable.

An attempt has been made at replacing the mirror with a Lambertian surface. However, this was not finished beyond a first effort at L_{d}; many an interesting difficult integration problem arose when finding source terms.

The Monte Carlo method defined the domain radius by applying a minimal, view factor condition on a control volume. It has to make a significant photon contribution to the sensor. However, in thicker domains multiple re-absorptions happen. Ray paths are no longer straight, but a piecewise connected line. Therefore, the domain had to be scaled-up. This problem is also of concern to the analytic solution: if one can find dimensions of the contributing region surrounding a sensor, one can use them as a natural element to discretize more complex shaped media. For example, a curved surface could be approximated by multiple plane-parallel systems. We could predict as well if a wall in the medium influences the radiance.

It might be interesting if the FRET effect can be added. During the concentration test its onset was seen. One might add the effect strength by modifying quantum yields. The by FRET produces photons would be an extra radiance field.

4

Analysis of a Layer-Height Imaging Setup

Chapter 2 concluded that ERLIF is a promising method for the imaging of liquid films. However, it is a small area method, and thus needs an extension to larger areas typical for hydrostatic bearings. Larger areas create non-perpendicular camera viewing and light source angles, whose effects need consideration. For convenience, this large area method was called GERIF. Also, the hypothesis that it actually does depend on background reflectivity must be verified.

GERIF observes colour-shifts in the emission spectrum at the top of the layer; the shift serves a proxy for the layer thickness h. Colour-shifts are studied by taking the ratio between the radiant fluxes at different wavebands—see Chapter 2 equation 2.2. The intention is to study the effects on the ratio for differing reflectivity, film thicknesses, viewing angle and irradiance angle of the light source. Film thicknesses are extended beyond the original 10 µm to 600 µm range requirement out of interest. To explore the ratio's dependency on all the variables, numerical experiments are conducted with the analytic solution to the FRTE. Beyond the numerical experiments, a real, static measurement setup is build to verify the predictive power of the analytic model. Creating it led to key design insights for the realization of a dynamic, lubrication-film height imaging setup.

4.1. Method

In the coming sections, all material properties are the same as in section 3.4. Any part specification can be found there too unless it is newly introduced.

4.1.1. The ratio

Let us start with a deep dive in how height information can be obtained from camera images: an aspect usually treated superficially in the film height measurement literature. The upcoming discussion was in part inspired by the discussion on general sensor models in [39, p. 240-245]. In Chapter 2, h is approximated by a calibration function on the ratio between the radiant fluxes passing through two different filter bands. The fluxes go from a patch on the observed surface to a camera's pixel. They are captured during a given shutter time. The equation is repeated here

$$h = f\left(\frac{\int_{T_1} \Phi_{\text{waveband 1}}\,\mathrm{d}t}{\int_{T_2} \Phi_{\text{waveband 2}}\,\mathrm{d}t}\right)$$

f is a calibration function depending, in part, on camera sensitivity and the filter transmissions. Assume now that a single camera is observing a liquid patch, and that the filters are swapped with an filter changer, just like in Figure 2.6. Lets rewrite f to a new calibration function to reflect that fact

$$h = g\left(\frac{\sum_\lambda \int_{T_1} \mathcal{R}_\lambda \tau_{1\lambda} \Phi_\lambda \, \mathrm{d}t}{\sum_\lambda \int_{T_2} \mathcal{R}_\lambda \tau_{2\lambda} \Phi_\lambda \, \mathrm{d}t}\right)$$

$\mathcal{R}_\lambda$ is the camera spectral responsivity, τ_λ's are the spectral transmissivities of the filters. We sum contributions at all the wavelength-bands centred on wavelength λ to obtain the total pixel grey value. Now, it will be shown that we can swap out Φ for radiance L_λ, which we readily obtain from the analytic solution to the FRTE. We reason as follows. Φ_λ depends on the geometry of the measurement setup such as: size of the entrance aperture, the size of the observed surface patch, distance between the two, and the angles between both surfaces. Geometrical constructs drop out when we ratio both radiant fluxes, as the geometry does not change between taking the photos. The camera and observed area are standing still after all. A small amount of radiant flux normalized over geometry is the radiance, L, as we encountered in Chapter 3.

$$L = \frac{\mathrm{d}^2\Phi}{\mathrm{d}\omega \mathrm{d}s}$$

L depends both on direction and location. The surface s defines the bearing's observed projected liquid patch. ω is the solid angle spanned by the entrance aperture. It defines the rays' directions of travel from patch to camera. The cancellation of geometry only happens when L does not vary too much with direction or over the observed liquid patch. The latter is likely for a fine enough camera resolution. The former happens if all rays travelling from patch to the camera's entrance aperture are nearly parallel. This can be explained by geometry: a physical entrance aperture has a diameter of mm's to cm's while the distance to the observed area is in the orders of 10's of centimetres. The cone spanned by this geometry has a very small apex angle. Therefore, rays are near parallel, and L is constant over this emission cone.

Finally write this as

$$h = g\left(\frac{\sum_\lambda \int_{T_1} \mathcal{R}_\lambda \tau_{1\lambda} L_\lambda(\theta, h) \, \mathrm{d}t}{\sum_\lambda \int_{T_2} \mathcal{R}_\lambda \tau_{2\lambda} L_\lambda(\theta, h) \, \mathrm{d}t}\right)$$

Now, define the ratio Ξ

$$\Xi = \frac{\sum_\lambda \int_{T_1} \mathcal{R}_\lambda \tau_{1\lambda} L_\lambda(\theta, h) \, \mathrm{d}t}{\sum_\lambda \int_{T_2} \mathcal{R}_\lambda \tau_{2\lambda} L_\lambda(\theta, h) \, \mathrm{d}t}$$

This is the fundamental quantity that is obtained from processing camera photos and the analytic solution.

4.1.2. Numerical experiments

Numerical studies with help form the analytic solution were conducted. They give insight into the method's sensitivities. Four experiments with different, constant mirror reflectivity, and different irradiance angles were done: $\rho_\lambda = 1$ and $\rho_\lambda = 0$; $\theta_\mathrm{e} = 0°$ and $\theta_\mathrm{e} = 45°$. The irradiance angle of the light source exciting the fluorophores is an important design choice. See Figure for a sketch of the domain 3.3. Correlation surfaces of Ξ for different viewing angles θ and thicknesses h are studied.

The ratio in numerical studies is

$$\Xi = \frac{\sum_{\lambda=515}^{525} L_\lambda(\theta, h)}{\sum_{\lambda=527}^{537} L_\lambda(\theta, h)}$$

The wavelengths correspond closely to the wavelengths of the applied filter in the real measurement setup but idealized as a perfect band-pass. The camera is also considered ideal, and the shutter times are equal.

The analytic solutions studies mirror like reflection. It is interesting to contrast with a Lambert reflection solution. Such a surface reflects radiance equally into all hemispherical directions and is thus the opposite of mirror reflection: a mirror has a one-to-one correspondence between angle of incidence and reflection, while a Lambertian surface has a one-to-all directions coupling. They are opposites in directionality. A Lambertian surface is simulated with the Monte Carlo method by adding a sampling method for a new direction after reflection—derived from [12]; see section 3.4.3 for an intro into Monte Carlo methods

$$\theta = \arcsin(\sqrt{u}), \quad \phi = 2\pi u$$
$$\hat{x} = \sin(\theta)\cos(\phi), \quad \hat{y} = \sin(\theta)\sin(\phi), \quad \hat{z} = -\cos(\theta)$$

Every u is a different realization of the uniform distribution. $\hat{z}$ has an extra minus, as the direction of the z-axis is normal to the sensor. 1×10^9 photon packages per h were used. After simulation, data was smoothed with a Gaussian filter—centred window of 15 samples— to remove statistical noise. Then the solution was transformed from the energy rate to the photon rate domain. Hereafter, it was normalized to 1 for comparison with the analytic solution to the FRTE.

4.1.3. Measurement setup

The ratio

A measurement setup was built which included a Pixelink PL-D795 RGB camera with a spectral green-channel responsivity of $\mathcal{R}_\lambda$; two filters were put on a filter changer to observe different wavebands—FLH532-10, FBH520-10 from Thorlabs—so only static imaging can be achieved

$$\Xi = \frac{\sum_{\lambda=510}^{528} \mathcal{R}_\lambda \tau_{1\lambda} L(\theta, h)_\lambda \lambda^{-1}}{\sum_{\lambda=523.5}^{539.5} \mathcal{R}_\lambda \tau_{2\lambda} L(\theta, h)_\lambda \lambda^{-1}}$$

They waveband of the 520 filter resides in the shoulder wavelengths of figure 3.11, so overestimation by the analytic solution is to be expected. Also, a conversion from photon to energy domain was done by applying

$$E = h\frac{c}{\lambda}$$

h is Planck's constant and c the speed of light in vacuum. The formula is the energy carried per photon. The camera's pixels gather energy and do not count photons.

The setup

An overall picture of the setup can be found in appendix A. A calibration device was made, see Figure 4.1, which consists of the aforementioned Edmund Optics mirror and glass disk. Both objects are placed at an angle with a 1 mm gauge block to create a well-defined, wedge-shaped water layer. Glass and mirror were put in a 2-part, PLA, 3D printed clamp; the two parts were put around the glass and bolted together. The mirror was held in place by 3 spring-loaded plungers fixed to the clamp, they prevent relative movement between glass and mirror and accidental damage by excessive holding forces. Friction held the gauge block in place. The entire clamp was then suspended with springs to the metrology frame to prevent any shocks from disturbing the water wedge. Inside the water layer, Eosin Y and Fluorescein were dissolved at a concentration of 0.125 mmol L^{-1}. In Figure 4.2, the device can be seen as viewed by the camera. Blue light is from the LED which made an irradiance angle in the water of $20°$. The camera was placed once straight below wedge, and once at an angle of $45°$. The refracted viewing angle inside the water must then be $\approx 32°$, which can be obtained from Snell's law. Ignoring angle effects of a finite entrance pupil.

Data processing

To obtain Ξ, one hundred pictures were snapped at a framerate of 10 s^{-1} for both filters and the dark image. A region of interest was then made by selecting pixel columns and rows, and within there, the mean value of each pixel over all pictures calculated. Thereafter, the averaged dark image was

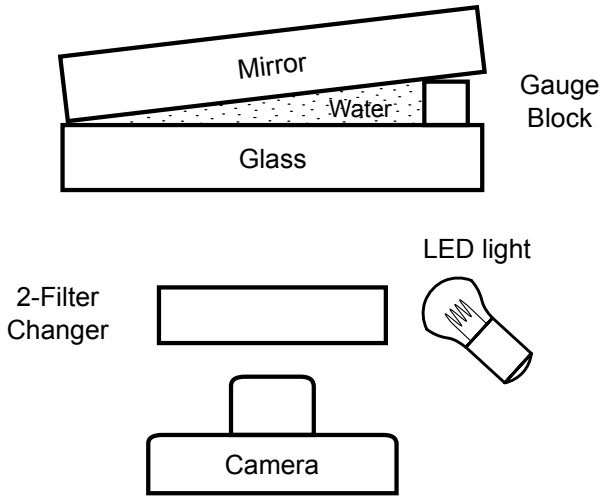

Figure 4.1: Measurement setup for verification of Ξ. Camera and LED light are actually in cross-planes to prevent specular reflection of the LED into the camera's field of view. Water has dissolved Fluorescein and Eosine Y.

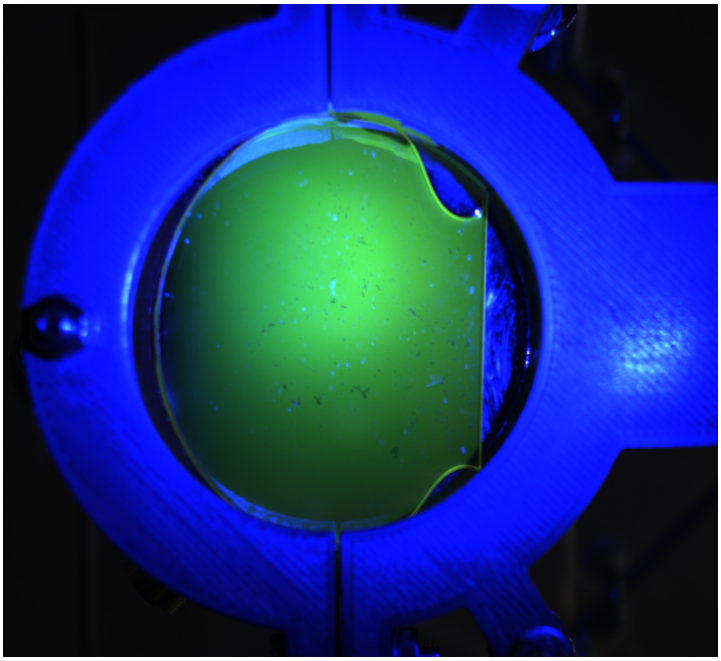

Figure 4.2: Underside of the water wedge. The mirror is spotted by chemical deterioration. Metallic strip at the right is the gauge block.

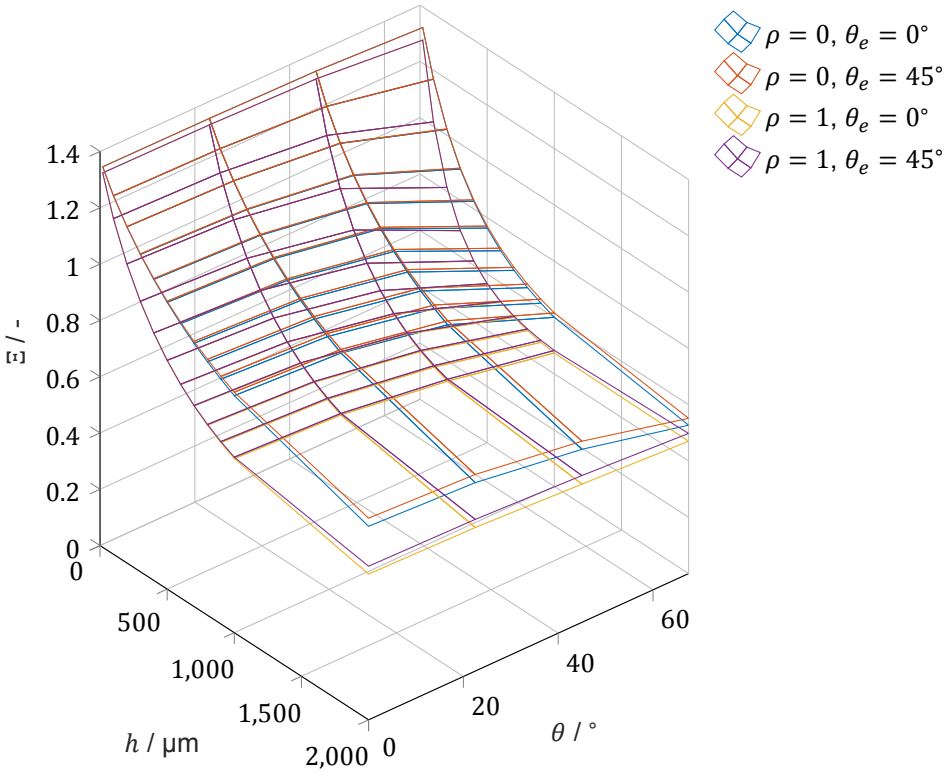

Figure 4.3: Ratios predicted by the analytic solution of the FRTE.

subtracted from the filtered images. The two resulting composite pictures—one for each filter band—were divided on a pixel basis to obtain the ratios. A 2-D Gaussian smoothing kernel with a standard deviation of two sigma removed random noise. The last step was taking the mean per pixel column, this gives a line of composite pixel values that represent Ξ versus h.
To get a better understanding of the noise. A raw Ξ picture for the region of interest was made. Two photos' pixel values were directly divided by another. No processing was applied except dark image removal.

4.2. Results

4.2.1. Numerical results

Figure 4.3 presents a comparison between the numerical experiments. The light source's irradiance is of small influence: a maximal deviation of only 2.3% and 3.0% for the full absorbing and full reflecting background.
The full reflection case depends weakly on view angle. A maximal error of 9% occurs. The full absorption case depends strongly on view angle beyond $20°$. For $\theta_e = 45°$, $\theta = 67.5°$, a Ξ reduction of 24% happens. In general, the difference between no and fully reflective cases increases with h and can run up to 36%.

Figure 4.4 depicts the analytic solution for a mirror and the MC simulation of a Lambertian surface. Both results are the same for thin layers while the Lambertian case has a 0% to 11.8% lower response at thicker layers. In general, the response form is the same. When we inspect some spectrums for comparison—see Figure 4.8— we see that for Lambertian reflection there is less radiation in the shoulder. Strong statistical noise is present.

4.2.2. Measurement setup

While measuring, it was observed that the mirror broke down, and the water wedge did not fully fill all space—see Figure 4.5. Grey spots are the locations where the reflective coating is removed. At the gauge block, water leaked away and this reduced pixel values in adjacent parts, such as the encircled

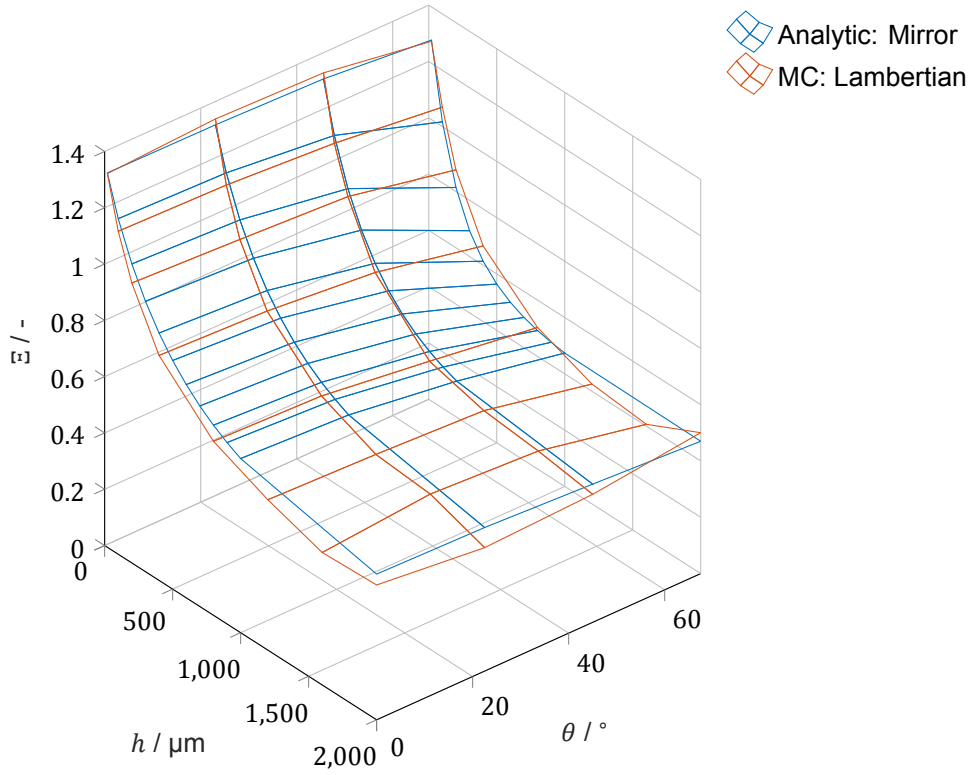

Figure 4.4: Ratios predicted by the analytic solution and MC simulation. Both for full reflectivity.

green area. The water was sucked away by capillary action into to slit between the glass and clamp. The region of interest for data processing, in yellow, was reduced in size by the onward creeping leak. In the far left of the region, the wedge never filled up with water.

Figure 4.6 demonstrates the comparison between measured and predicted Ξ. The shape is similar but overestimated by the model. The very thin and very thick parts data deviate strongly; the thin part is in the not-filled area, and the thick part is adjacent to the gauge block. For $\theta = 32°$, a dip at 590 µm is present; inspection of the gain-added camera images revealed the presence of a bubble. Both curves do not change strongly with altering view angle.

Figure 4.7 demonstrates the raw ratio between two images. Random noise is present along with several significant outliers.

4.3. Discussion

4.3.1. Numerical experiments

Angle of irradiance has only a weak influence on Ξ. One can use the most convenient light source, and even combine multiple sources as the FRTE is linear in irradiance. It is advisable to keep the viewing angle inside the layer not too large. Luckily, refraction helps here: the camera in the test was at $45°$ while the radiance in the layer was $32°$. The ramification is that camera angular alignment is of limited influence.

Numerical experiments showed similar behaviour as the re-drawn responses of the ERLIF study—Figure 2.8. No reflection increases the ratio. Reflection allows more photons to be re-absorbed and re-emitted by the Eosin, therefore the energy at longer wavelengths increases which in turn decreases the ratio. Reflectivity of the background matters as does the type of reflection. Reflectivity has the much stronger effect, producing differences up to 36%. Lambertian reflection is very different in character to the mirror, but the Ξ response was only 11.8% lower. Inspecting the spectrums does not give a conclusive answer if this is generally true: the filters are present in the shoulder of the analytic emission spectrums, the Lambertian shoulder has the same form, but is systematically lower. So, the Ξ is mea-

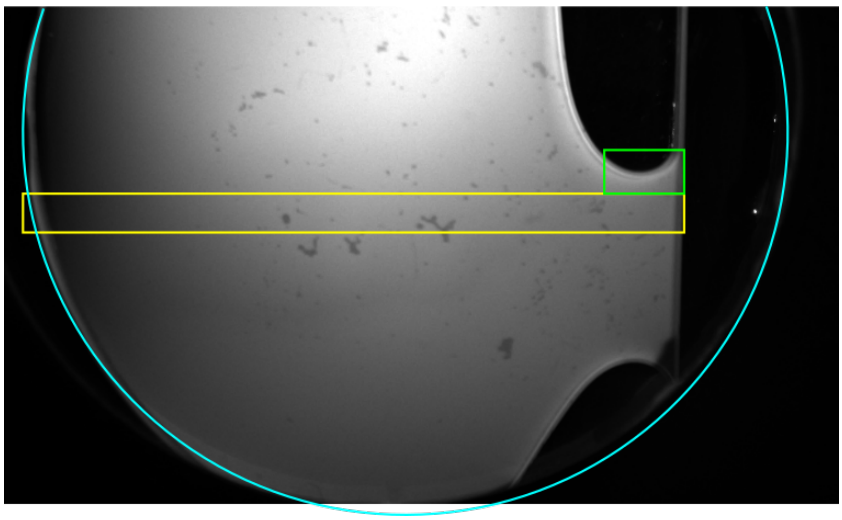

Figure 4.5: Camera
still for 532 nm filter. Light blue is the circumference of the mirror. Yellow is the region of interest used for data processing, that at its edges is not filled with water. Green shows the incursion zone of air influencing the radiance. Mirror coating loss caused the spots.

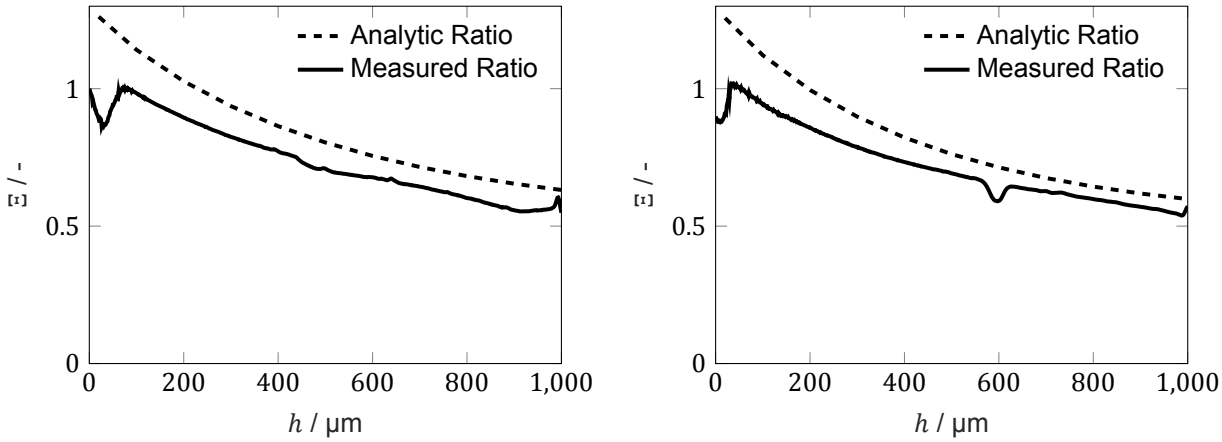

(a) $\theta_e = 20 \pm 5°$, $\theta = 0 \pm 5°$.

(b) $\theta_e = 20 \pm 5°$, $\theta = 32 \pm 5°$

Figure 4.6: Comparison of real measurement ratio and predicted ratio.

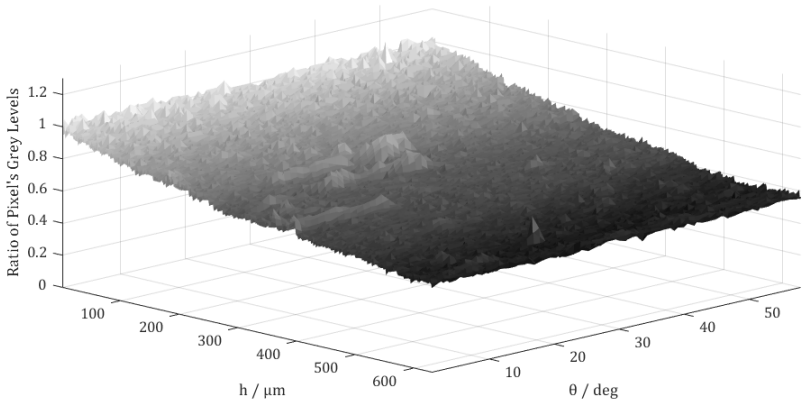

Figure 4.7: The raw, unprocessed ratio between 2 photos' grey values.
Some noise is present. Large, positive deviations are from the deterioration of the reflective layer.

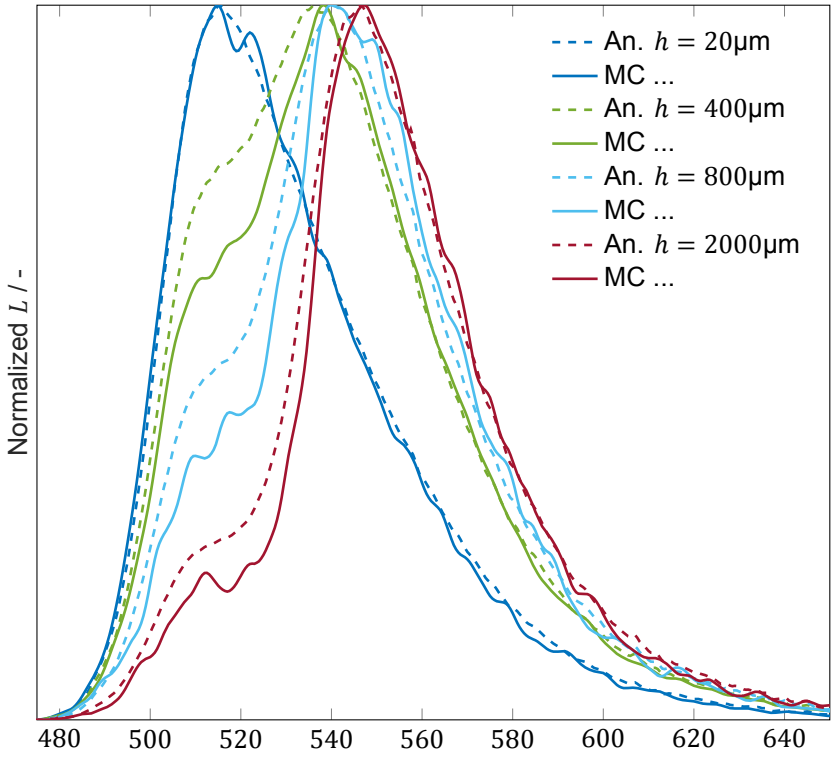

Figure 4.8: Emissions spectrum comparison between the Lambertian Monte Carlo simulation and the analytic specular solution.

sured for a fundamentally different radiance spectrum. The notable exception is 20 µm, were the layer is so thin, that average path-lengths are the same and thus both reflection conditions produces the same emission spectrums. Lambertian reflection will on average lengthen the photon path distance and thus more absorption takes place, so the shoulder deepens with respect to the analytic solution. Only the position of the peaks seem predictable by the analytic solution. Predictive power is expected increase for systems with lower ρ, as the effect of the reflecting boundary weakens. Fortunately, hydrostatic bearings will have a reflection type more closely resembling a mirror than a Lambertian reflector.

4.3.2. Measurement setup

The analytic model did overestimate the response as expected: the short wavelength filter at 520 nm is precisely in the waveband were the analytic FRTE showed the most uncertainty. It is likely that if better material spectra can be used, the model and measurements would agree much better. The shape is well matched, however. Figure 4.9 shows how good the analytic data matches the measured data when we correct it. To do so, multiply by 1.1389, which is the ratio between the mean values of the analytic and measured spectrums in the filter band—see Figure 3.11a with the h =500 µm lines.

Measurement data swings in the thin and thick limit are the results of the: unfilled tip of the wedge, air bubble presence, or the proximity of the gauge block. Relying on surface tension to keep the liquid in the device is not enough. Degradation of the coating and air bubbles are the probable cause for the outliers in the raw image. Degradation means more absorptive surface, and thus a larger ratio as is seen from Figure 4.3. However, the raw-image has a pleasantly small noise, suggesting that static imaging is possible with a very simple camera.

The overall system was successfully simplified to a simple camera with filter changer and a LED light source. Compare the system in appendix A to Figure 2.7. Observing larger surface than an US mint quarter coin is certainly doable. The laser is successfully swapped for a diverging LED-beam light.

4.3.3. Applicability of results to other measurement conditions

A particular combination of dyes and filters were used. Eosin's absorption spectrum has a near perfect overlap to Fluorescein's emission spectrum. Both dyes are archetypical fluorophores with one, narrow

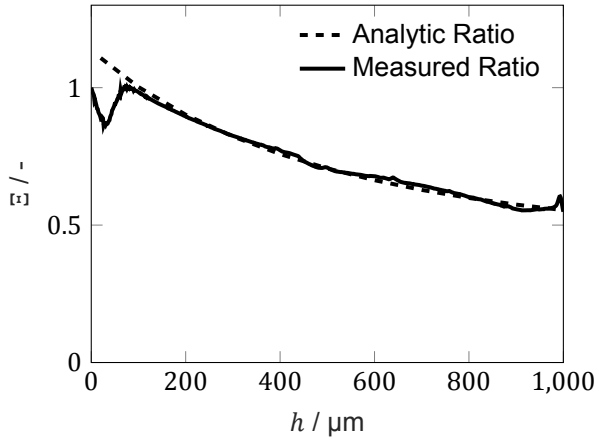

Figure 4.9: $\theta_e = 20 \pm 5°$, $\theta = 0 \pm 5°$. Comparison of real measurement ratio and predicted ratio that is corrected for deviations: material data uncertainty makes the analytic model overestimate radiance in the 520 nm filterband. Correction factor, 1.1389, derived by the division of the mean values found in Figure 3.11a, $h = 500$ µm lines.

absorption and emissions peak without substantial spectral overlap and significant quantum yields. They are well-excited by the LED's blue light, as their photon absorption is strong there, and their peak molar absorption coefficient is of the same order. It is hypothesised that for similar dyes, equal results are found: low-influence of irradiance angle and view angle. Of course, some variation is to be expected. One could use this variation to tune the system and try different dye combinations, concentrations, or different filter sets.

4.4. Conclusion

Numerical experiments for this particular set of dyes and filters show that the effect of a light source on the measurement is small for angles up to at least 45%. The camera angle with the normal to the layer's surface is not that important. Keep the camera such, that observed radiance about to leave the layer is not at angles larger then several 10's of degrees.

Background reflectivity matters. Large deviations up to 36% were found between a full reflective mirror and a completely absorbing background. Lambertian reflection has a similar measurement response as for the mirror case, with the largest error being 11.8%. This might have been a coincidence for this particular set of dyes and filters, as the emission spectrums at the top of the layer were very different: the absorption shoulder at Eosin's absorption peak was much lower than the mirror one's. The analytic model to the solution has limited predictive power for such a surface. For mirror like surfaces, the model can be used to optimize the measurement system. A very good fit is expected if material data for the analytic model was better.

Similar dyes and filter sets are assumed to lead roughly the same measurement system behaviour. Some tune-ability is possible here.

The test object consisting of a mirror at an angle with glass needs a redesign. The mirror layer was deteriorating in the water. The water wedge could not entirely fill up the wedge between mirror and glass: at the thick end, water leaked away due to capillary suction between clamp and glass; the thin part of the wedge was never filled, cause unknown. The test object could serve as a calibration vessel like depicted in Figure 2.5.

The static, simple camera setup with LED light showed that a simpler design is viable for hydrostatic bearing imaging.

5

Practical Measurements

This thesis introduced many theoretically important concepts and methods. However, the ultimate goal was to build a functioning layer imaging system for hydrostatic bearings. A lofty goal not reached, but we do now have enough understanding of the physics to suggest what the ultimate setup will look like. Its concept will be introduced here.
Many important, practical lessons about dye selection and building the setup were learned. Most of those lessons do not quite fit the scientific nature of the previous chapters or are just mentioned in passing. It is helpful if some are stated explicitly, as new projects with the method are foreseen.

5.1. Concept of a dynamic imaging Setup for hydrostatic bearings

Figure 5.1 shows the proposed concept for a dynamic imaging system that can film the lubrication layer underneath the hydrostatic bearing. It uses multiple light sources and two cameras.

We know that the radiance leaving the layer is linear in the light source's irradiance and that its angle is not that important. So, combining multiple light sources that add up their irradiances is possible. It prevents shadow formation and improves signal to noise: a single source will likely create light and dark areas, which causes a brightness contrast in radiant flux for a camera. Quite like taking a portrait photo against direct sunlight. Likewise, there are upper limits on how strongly fluorophores can be irradiated before non-linearities occur. A homogenous light source can take the layer right to this very limit, ensuring maximal utilization of all fluorophores. The non-linearities, photobleaching and saturation, are treated in the next section.

Viewing angles of the camera can be, with some care, kept within several 10's of degrees without altering the measurement ratio Ξ. Observing the large area of a bearing is no problem. Furthermore, two cameras with each their own filter can be put together and image the same lubrication-film patches. Filming an actual moving bearing is a possibility. A long-held interest of the research group. This is not possible with the previous built measurement setup, where a filter changer was used—see A. After taking a photograph with filter 1, it was swapped for filter 2. This takes time, and therefore only static imaging can be done. There is, nevertheless, a catch to using two cameras: the ratio Ξ assumes that both photo's are made with the same setup geometry between camera and object plane—read section 4.1.1. Two cameras are spaced a bit apart, so the angle by which they observe a film patch is slightly different. That angle is actually a great design challenge in achieving even image illumination on a camera's sensor chip. Some typical problems are: field darkening, the cosine fourth power law, and vignetting. These effects do not matter for a single camera setup: both pictures suffer equally from the same effects, taking their ratio makes them drop out. It is thence advisable to place the cameras very close together and some distance away from the layer to keep the angular difference between the pixels small. Another aspect is that the same patch is observed by a different pixel in each camera with each their own differing sensitivity. Hence, calibration is necessary. A strategy could be to observe an evenly-illuminated, flat sheet of non-glossy white paper—a Lambertian reflector—and tune the individual pixel gains. A standard procedure available in camera control software.

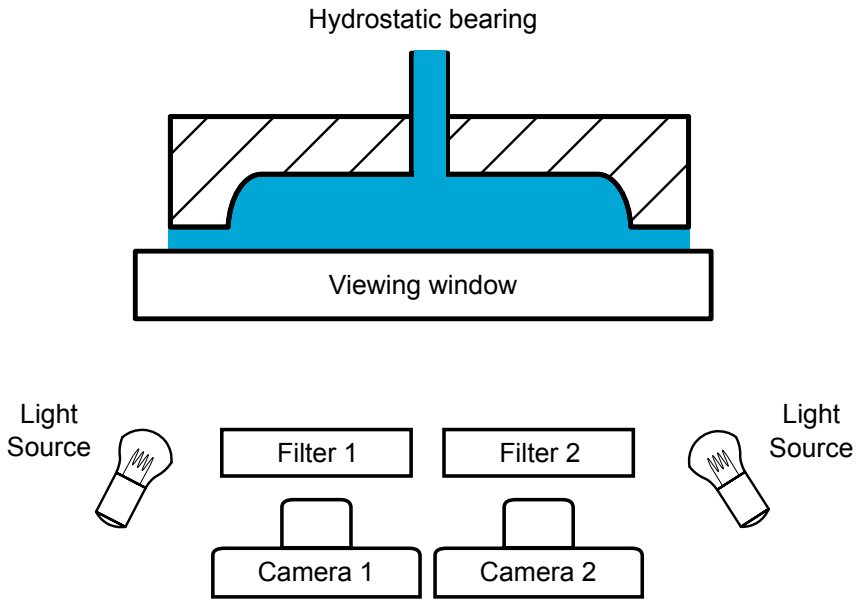

Figure 5.1: Suggested setup for dynamic imaging. Distributed lighting for a more even irradiance improves noise and removes shadows. Two closely spaced cameras simultaneously film the film the lubrication layer.

5.2. Practical aspects in design and dye selection

5.2.1. Dye selection and material properties

If one wants to use different dyes there are some aspects to consider. Toxicity: many dyes are known or suspected of being dangerous. Sensitivity to environment: all dyes exchange energy with their molecular environment, it can shift spectra and quantum yields. Some factors are: solvent, pH, contaminants, and temperature. Literature studies can give some insight into these, but be aware that the conditions under which experiments are conducted can vary significantly [41]. You will likely require cheaper bulk chemicals, which are less pure than the analytic standards used in the literature. Hence, measuring their properties under the circumstances expected in the bearing is needed.
When material properties are required, measure them on proper fluorometers. The methods used in the previous chapters were adequate to verify the models under the limited time available, but not good enough for true measurement setup simulations.

5.2.2. Photobleaching and fluorescence saturation

Photobleaching and fluorescence saturation limits how strong we can excite the fluorescent layer. Fluorescence saturation happens when the irradiance becomes so large that the number of dyes in the ground state become depleted, which alters the absorptivity, and thus influences the fluorescent radiance. This breaks down Ξ, no longer making it independent of variation in the light source. A criterion to prevent the phenomenon's onset can be derived from the model of [27][1]

[1] Here is a quick sketch how one can derive the criterion, starting from their main governing equation. Assume that the number of molecules in the excited state n_2 does not change

$$\frac{\mathrm{d}n_2}{\mathrm{d}t} = n_0\, B\, \rho - n_2\, (A + B\, \rho) \quad n_0 = n_1 + n_2$$
$$0 = n_0\, B\, \rho - n_2\, (A + B\, \rho)$$
$$n_2 = \frac{B\rho}{A} n_1$$

Now assume that the ground state molecules, n_1, are much more numerous than in n_2, and thus

$$\frac{B\rho}{A} << 1$$

Rewrite this criteria now to the quantities used in this work.

$$\frac{\alpha_{\lambda_e} \tau E_{e0}}{1000\, c\, N_a} << 1$$

α_{λ_e} is a dye's absorptivity at the beam's wavelength in m^{-1}. E_{e0} the photon irradiance, $q\, s^{-1}\, m^{-2}$, τ the fluorescent lifetime s, c the molar concentration in $mol\, L^{-1}$, 1000 a conversion constant with units of $L\, m^{-3}$, and N_a Avogrado's constant.
Photobleaching is the destruction of fluorophores by light. Its mechanisms are varied and to difficult for us to predict. The countermeasure is to test for it: put a layer in the setup, and observe it over a prolonged time: say the length of time needed to do a hydrostatic bearing test. Fluorescence should not diminish. New inflow of liquid underneath the bearing could help here by ”refreshing” the fluorophores.

5.2.3. Concentration depended effects and FRET

Concentration depended or FRET effects can radically change emission behaviour, which might not immediately be obvious when experimenting. It actually delayed the project for some time and put the entire modelling effort in question. There is a simple way to catch the problem by analysing the so-called optical thin limit. Here, layers are so thin, that re-absorption and reflection effects do not matter and the layer's emission spectrum is the sum of the dye's emission spectrums. If we measure such a thin layer, and that spectrum differs, something is off. For example, emission peak are several nanometres shifted. The equation to predict the optical thin limit spectrum is

$$\epsilon = \alpha_{1e}\, q_1\, \bar{\epsilon}_1 + \alpha_{2e}\, q_2\, \bar{\epsilon}_2$$

q are the quantum yields for dye 1 and 2, α_e, the representative absorptivity for the excitation irradiance, $\bar{\epsilon}$ are the dyes' emission spectrum. Optically thin is defined as $(\alpha_{1e} + \alpha_{2e})h < 0.01$. This relation can be derived by doing a linear expansion of all exponents in L_d, equation B.9, and keeping only the first term. Such a layer can be easily made by placing a drop between two microscope objective glasses and then rubbing them together. There is a catch here: concentrations are used to scale the absorptivity. Therefore, the strength of photon re-absorption is affected, which determines the upper- and lower limit of h's that can be measured. Concentrations are no free chosen variable, but are tuned to a specific h range. If the concentration is weak, only thicker layer can be analysed.

5.2.4. Light source design

The light source needs to be strongly directional to maximize irradiance in the layer while minimizing stray light. Especially the direct specular reflection of the light source into the camera's field of view should be prohibited. The light reflected from the viewing window is strong enough to pass through the filters and disturb the measurement. Therefore, the light source—see Figure 5.2— could adjust its angle with the layer, and swivel around its base. A composite lens and reflector were used to focus the light only on the layer. An extra, 3D-printed hood was clipped onto the optics to remove the last bit of stray light. Its double-walled, angled structure effectively traps light by letting it reflect multiple times, each time removing some energy. A simple single-walled design was not effective enough to prevent stray light.

5.3. Tuning the system with the analytic solution

The scripts for running the analytic solution and calculating the measurement response Ξ are attached in the appendices. They only need material properties, height, and viewing angles to run. The method assumed that all spectrums are sampled at the same wavelength. It is only valid for mirror like surfaces. Before using the script check if your layer has vanishingly small scattering. The reflection from the layer into the glass should be irrelevant, which can be checked by the well-known Fresnel equations—see Figure 3.8 for an example of water to glass for an acceptable reflection. The model can easily be used to tune the system to your specific needs. Be careful, all the inputs and outputs that depend on an angle are defined inside the medium. The viewing window, and air add two refractive interfaces; use Snell's law whenever necessary. Always check if the model is still valid: it assumes that only two generations of fluorescent photons can exist. A simple check is to see if all the indirect solution spectrums are approaching the same magnitude as the direct solutions at heights below the maximum height you intend to measure.

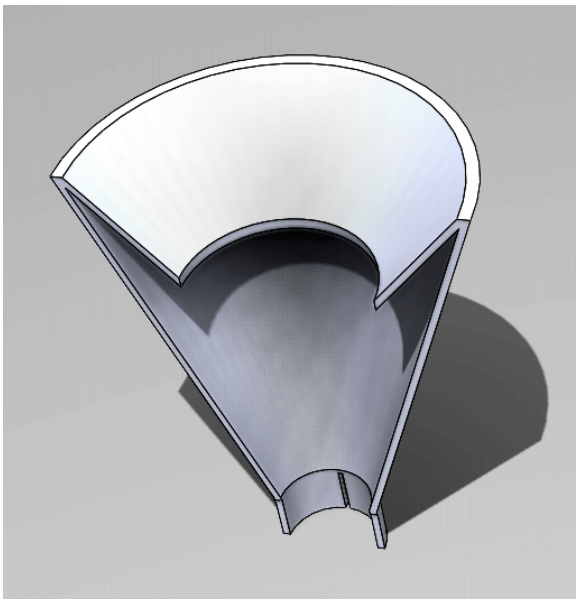

Figure 5.2: Left: the light armature with a XPE - Starboard blue LED and Lisa2-Clip16-XP lens. Direction of the light can be set with the screw and rotating the base. Right: cut-through of the stray light hood

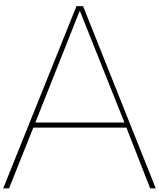

Appendix: Setup Picture

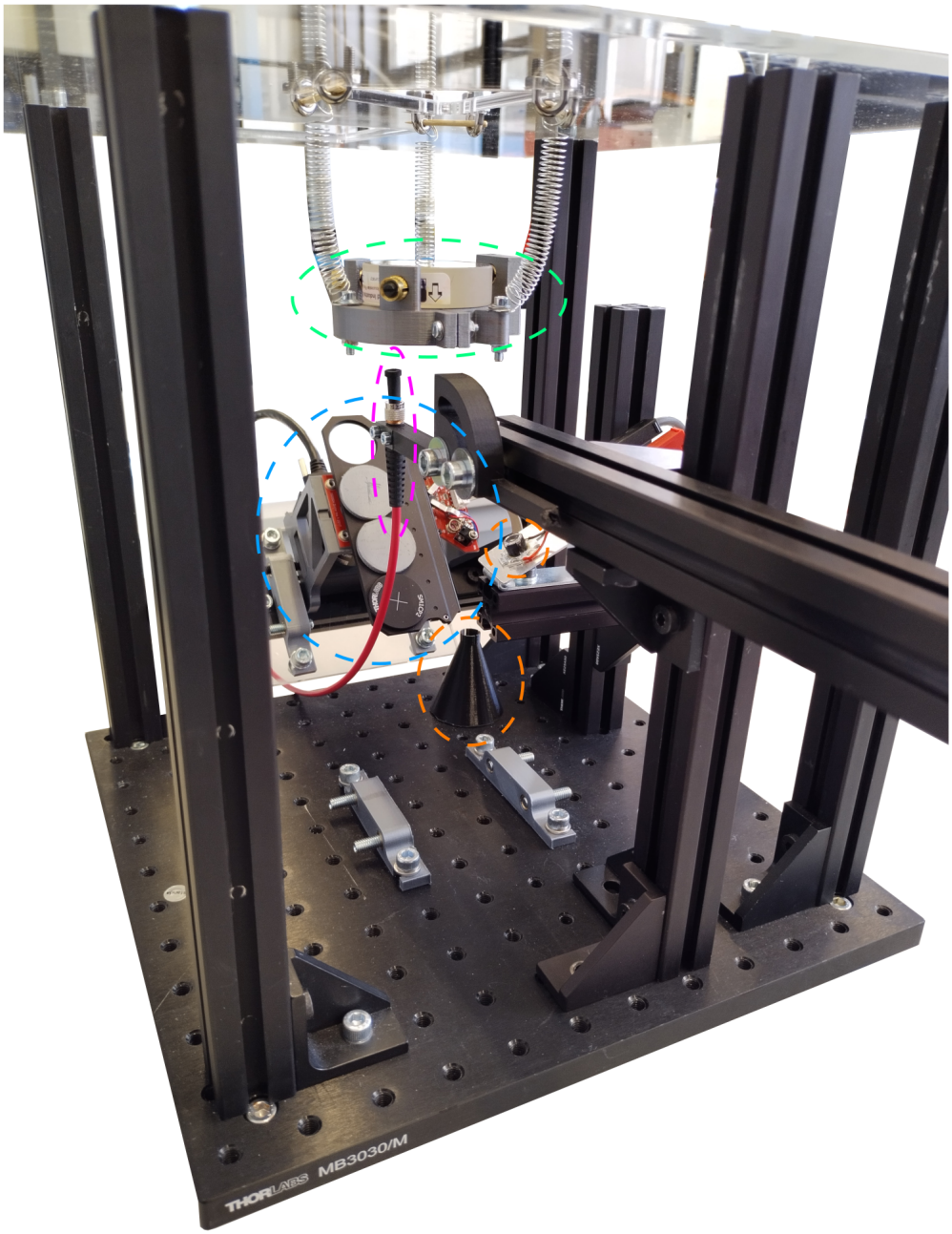

Figure A.1: Measurement setup without its blackout cloth. Light blue: camera with filter changer inside the 45° clamp. Magenta: optical fibre with numerical aperture reducer. Light green: suspended test vessel made from a glass disk—not visible due to the grey clamp—and flat mirror held in place by black spring plungers screwed into brass thread inserts. Orange: LED light and its detached stray light cap.

B

Appendices to the Analytic Solution

B.1. Appendix: Derivation of the Fluorescent Radiative Transfer Equation

This chapter derives the FRTE in three forms: along a ray path; in a Cartesian coordinate system; for a plane-parallel system. Derivation follows in a way similar to the non-fluorescent one in [28, 42]. We do not regard scattering.

B.1.1. The FRTE along a ray path

Consider the cylindrical infinitesimal volume in figure B.1. At ray coordinate l, a light ray passes in the direction $\mathbf{l}$ which is perpendicular through the cylinder head. The ray's spectral photon radiance, L_λ , is defined as $\mathrm{q\,s^{-1}\,m^{-2}\,sr^{-1}\,nm^{-1}}$ at λ: a photon flux density per unit surface area and unit solid angle at a specific colour [39, p. 24]. Along a small path length $\mathrm{d}l$, L_λ changes by

$$\frac{\mathrm{d}L_\lambda(l,\mathbf{l})}{\mathrm{d}l} + \alpha_{\mathrm{m}\lambda}L_\lambda(l,\mathbf{l}) + \sum_{k=1}^{N}\alpha_{\mathrm{f}_k\lambda}L_\lambda(l,\mathbf{l}) = \underbrace{\sum_{k=1}^{N}\frac{q_{\mathrm{f}_k\lambda}}{4\pi}\int_{\lambda'}\alpha_{\mathrm{f}_k\lambda'}\int_{\omega}L_{\lambda'}(l,\mathbf{l}')\mathrm{d}\omega\mathrm{d}\lambda'}_{S_\lambda} \tag{B.1}$$

This is the FRTE in one-dimensional Lagrangian coordinates. L_λ gets absorbed by the medium, for this use the absorption coefficient $\alpha_{\mathrm{m}\lambda}$. Furthermore, there are N fluorophores available where each has their own unique absorption coefficient $\alpha_{\mathrm{f}_k\lambda}$. They also add to the radiance of the ray, and thus include a source term S_λ on the right-hand side of the equation. It works by absorbing radiance $L_{\lambda'}(l,\mathbf{l}')$ coming in from all directions $\mathbf{l}'$ surrounding the volume. This is represented as an integration over the entirety of all small solid angles $\mathrm{d}\omega$. Since fluorophores can alter wavelengths of in-and-out-going photons, we need to do this solid angle gathering over every wavelength λ'. The fluorescent process of absorbing photons at wavelengths λ' and re-emitting them at wavelength λ is not perfect: so add an efficiency term called the spectral quantum yield $q_{\mathrm{f}_k\lambda}$. Lastly, fluorescence is an isotropic emission process in all directions and thus divide all gathered radiance by the solid angle of a sphere: 4π.

Emission is captured by the spectral quantum yield with the following definition

$$q_{\mathrm{f}_k\lambda} = q_{\mathrm{k}}\bar{\epsilon}_{\mathrm{k},\lambda}$$

q_{k} is the "regular" quantum yield for a fluorophore: the ratio of photons emitted to photons absorbed and it is generally independent of wavelength but does depend on the environment of the molecule [10, 18, p3; p. 7-9]. In this work, $\bar{\epsilon}_\lambda$ is a fluorohore's emission spectrum normalized such that the area under the curve equals 1. $\bar{\epsilon}_\lambda$ behaves, essentially, as a probability density function for the change of a photon emission at λ. It too depends on environment, but not the wavelength of the absorbed photon[10, 18, ;p. 3, p. 7].

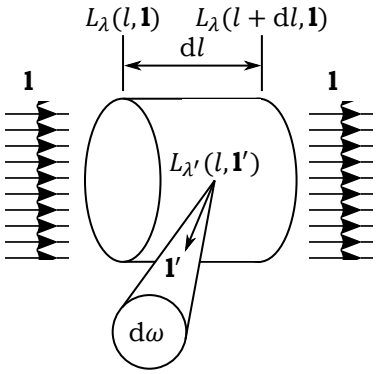

Figure B.1: Ray passing through a small cylinder volume along a path l

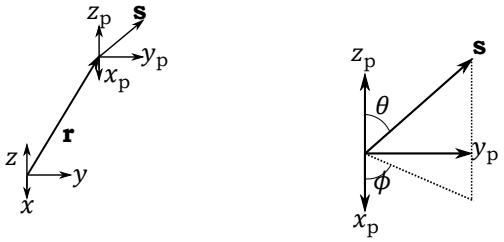

Figure B.2: The
coordinate systems for radiation transfer: a fixed, Cartesian one, and a local, spherical one—denoted by subscript p. Local is for direction of the photons.

B.1.2. The FRTE in a Cartesian coordinate system

The Langrangian frame of reference is not useful for a practical situation: one observes the medium at a fixed location and not along a ray path. Hence, an Eulerian description with cartesian coordinates is necessary, see figure B.2. The coordinates are put in a vector $\mathbf{r} =< x, y, z >$, then the time stationary derivative is

$$\begin{aligned}\frac{\mathrm{d}L}{\mathrm{d}l} &= \frac{\mathrm{d}x}{\mathrm{d}l}\frac{\partial L}{\partial x} + \frac{\mathrm{d}y}{\mathrm{d}l}\frac{\partial L}{\partial y} + \frac{\mathrm{d}z}{\mathrm{d}l}\frac{\partial L}{\partial z} \\ &= \mathbf{s}\cdot\nabla L\end{aligned}$$

$\mathbf{s}$ is the direction vector composed of the direction cosines on the local projection of the coordinate system; see the right part of Figure B.2 for a magnification of the projected system. Combining the direction vector and equation B.1 gives the FRTE in the Eulerian frame

$$\mathbf{s}\cdot\nabla L_\lambda(\mathbf{r},\mathbf{s}) + \alpha_{\mathrm{m}\lambda}L_\lambda(\mathbf{r},\mathbf{s}) + \sum_{k=1}^{N}\alpha_{\mathrm{f_k}\lambda}L_\lambda(\mathbf{r},\mathbf{s}) = \underbrace{\sum_{k=1}^{N}\frac{q_{\mathrm{f_k},\lambda}}{4\pi}\int_{\lambda'}\alpha_{\mathrm{f_k}\lambda'}\int_{\omega}L_{\lambda'}(\mathbf{r},\mathbf{s}')\mathrm{d}\omega\mathrm{d}\lambda'}_{S_\lambda} \tag{B.2}$$

It is very convenient to express the direction cosines in coordinates on a unit sphere θ and ϕ.

$$\mathbf{s} =< \sin(\theta)\cos(\phi),\ \sin(\theta)\sin(\phi),\ \cos(\theta) >$$

The reason for this expression is that the integral in source term S_λ simplifies a lot since the unit sphere coordinates form the natural domain for a solid angle integral, so let us define an infinitesimally small solid angle

$$\mathrm{d}\omega = \sin(\theta)\mathrm{d}\theta\mathrm{d}\phi$$

The general integration for a full unit sphere is

$$\int_0^{2\pi}\int_0^{\pi} \sin(\theta)\mathrm{d}\theta\mathrm{d}\phi \ = 4\pi$$

B.1.3. The FRTE in a plane-parallel system

In the case of plane-parallel system, only the z direction matters and L no longer depends on ϕ. As a result, equation B.2 reduces to

$$\cos(\theta)\frac{\partial L_\lambda}{\partial z} + \alpha_{\mathrm{m}_\lambda} L_\lambda(z,\theta) + \sum_{k=1}^{N} \alpha_{\mathrm{f_k}\lambda} L_\lambda(z,\theta) = \underbrace{\sum_{k=1}^{N} \frac{q_{\mathrm{f_k}\lambda}}{2} \int_{\lambda'} \alpha_{\mathrm{f_k}\lambda'} \int_0^{\pi} L_{\lambda'}(z,\theta')\sin(\theta')\,\mathrm{d}\theta'}_{S_\lambda} \qquad \text{(B.3)}$$

And 4π reduces to 2 by partial evaluation of the source term, to wit

$$\int_0^{2\pi} \sin(\phi)\mathrm{d}\phi = 2\pi$$

In practice, the integral over all wavelength is a summation term, as material data is given in tabulated form; there are no simple functions describing the spectrums. Photon radiance quantities such as L, E, and Φ are then no longer in the derivative form with units $\mathrm{q\,s^{-1}\,m^{-2}\,sr^{-1}\,nm^{-1}}$, but they are defined on a waveband centred on λ, and are now given in units $\mathrm{q\,s^{-1}\,m^{-2}\,sr^{-1}}$. λ subscripts change from a derivative to an index. This concludes the derivation of the FRTE as given in 3.7.

B.2. Appendix: Constructing spectrums with the solutions

Solutions to the FRTE are found by MATLAB's symbolic toolbox. The symbolic solution are then converted to numeric functions, they form the basis of practical simulations. Although the method of section 3.3 can find the overall solution of all N fluorophores all at once, it might be interesting to investigate the solutions for the individual dyes, so their individual contributions to the overall emission spectrum and couplings can be better understood. A final summation for all dyes gives the complete solution. Summation comes at the cost of extra computation time. For a full spectrum calculation, the contribution of all fluorophores at every relevant wavelength needs to be added. Start by defining the following absorption coefficients

$$\alpha_{\mathrm{e}} = \alpha_{\mathrm{m}} + \sum_{\mathrm{k}=1}^{\mathrm{N}} \alpha_{\mathrm{e_k}} \quad \alpha_{\mathrm{d}\lambda} = \alpha_{\mathrm{m}\lambda} + \sum_{\mathrm{k}=1}^{\mathrm{N}} \alpha_{\mathrm{d_k}\lambda} \quad \alpha_{\mathrm{i}\lambda} = \alpha_{\mathrm{m}\lambda} + \sum_{\mathrm{k}=1}^{\mathrm{N}} \alpha_{\mathrm{i_k}\lambda}$$

Subscripts $\mathrm{e, d, i}$ denote the excitation, direct, and indirect solutions. Since the excitation light is monochromatic, the wavelength subscript is dropped and just treated as constant. Please read section B.3 for the precise definition behind α_{e}.

Now, for the direct solution part at wavelength λ, sum the contribution of all dyes. The k subscript denotes the individual dye's spectral material properties, s means the absorption coefficient inside source term S_λ.

$$L_{\mathrm{d,tot}}(z,\theta,\lambda) = \sum_{\mathrm{k}=1}^{\mathrm{N}} L_{\mathrm{d}}\{\alpha_{\mathrm{e}}, \alpha_{\mathrm{es_k}}, \alpha_{\mathrm{ds_k}\lambda}, \alpha_{\mathrm{d}\lambda}, q_{\mathrm{d_k}\lambda}, \rho_{\mathrm{d}\lambda}, \rho_{\mathrm{e}}, E_{\mathrm{e0}}\} \tag{B.4}$$

The indirect contributions are bit more difficult, since for every dye the influence of all other N dyes for every wavelength λ' needs to be added up. The next equation can be read as: for a give dye l, calculate for all wavelengths the influence it has on another dye called k. Then take the influence of the next dye l on dye k, and so fort. Repeat this process until the influence of all dyes on dye k are calculated, then repeat this process for a new dye k.

$$L_{\mathrm{i,tot}}(z,\theta,\lambda) = \sum_{\mathrm{k}=1}^{\mathrm{N}} \sum_{\mathrm{l}=1}^{\mathrm{N}} \sum_{\lambda'} L_{\mathrm{i}}\{\alpha_{\mathrm{e}}, \alpha_{\mathrm{es_l}}, \alpha_{\mathrm{ds_k}\lambda'}, \alpha_{\mathrm{d}\lambda'}, \alpha_{\mathrm{i_k}\lambda}, q_{\mathrm{l}\lambda'}, q_{\mathrm{k}\lambda}, \rho_{\mathrm{d}\lambda'}, \rho_{\mathrm{i}\lambda}, \rho_{\mathrm{e}}, E_{\mathrm{e0}}\} \tag{B.5}$$

After the calculation of the direct and indirect terms for a single wavelength λ , we can sum them together to obtain the total photon radiance.

$$L_{\mathrm{tot}}(z,\theta,\lambda) = L_{\mathrm{i,tot}}(z,\theta,\lambda) + L_{\mathrm{d,tot}}(z,\theta,\lambda) \tag{B.6}$$

The method needs to be refined since the indirect solutions for the fluorescent cascading regime cannot always be applied as described in section B.6. The no-source term regime is simple: set the contribution to zero. For the other regime, no absorption, use the limit case equations B.16, B.17, and B.18 to construct the solution. During a numerical implementation, a case-switch can easily be implemented: If $\alpha_{\mathrm{d}\lambda}$ is very small, set $L_{\mathrm{i},\lambda}$ in B.5 to zero. If $\alpha_{\mathrm{i}\lambda}$ is very small, use the limit solution of L_{i}.

B.3. Appendix: Solving for excitation photon irradiance E

The fluorescent radiative transfer is driven by an external light source; we need to have mathematical description of its photon flux inside the layer. Take as an excitation source a monochromatic beam of photon irradiance hitting the top of the layer with magnitude E_{e0} and angle θ_{e}. The physics is best modelled with the Lambert-Beer Law, equation 3.3, repeated here for convenience

$$E_{\lambda}(l) = E_{\lambda}(0)\,\mathrm{e}^{-\alpha_{\lambda} l}$$

The beam is monochromatic, so drop the λ subscripts. α_{eh} is the sum of all fluorophore absorptivities plus the medium's one's. The path length, l, for the beam heading towards the mirror is

$$l = \frac{h - z}{||\cos(\theta_{\mathrm{e}})||}$$

With ||…|| the absolute value of the direction cosine, which for convenience will now be added to the absorptivity by defining

$$\alpha_{\mathrm{e}} = \frac{\alpha_{\mathrm{eh}}}{||\cos(\theta_{\mathrm{e}})||}$$

Hence, the downward irradiance towards the mirror is.

$$E_{\mathrm{d}}(z) = E_{\mathrm{e0}}\,\mathrm{e}^{-\alpha_{\mathrm{e}}(h-z)}$$

The boundary condition for the upwards radiation at the mirror is: upward irradiance is equal to the reflected irradiance of the downward solution

$$E_{\mathrm{u}}(0) = \rho_{\mathrm{e}} E_{\mathrm{u}}(0) = \rho_{\mathrm{e}} E_{\mathrm{e0}}\,\mathrm{e}^{-\alpha_{\mathrm{e}} h}$$

The upwards irradiance travels a path-length $z/|| \cos(\theta_{\mathrm{e}}) ||$. Use Lambert-Beer Law and find

$$E_{\mathrm{u}}(z) = \rho_{\mathrm{e}} E_{\mathrm{e}0}\, \mathrm{e}^{-\alpha_{\mathrm{e}}(h+z)}$$

We need to sum both solutions together to find the total irradiance through a surface. This is different to radiance, which depends on the direction of travel thus is a direction dependent density. E on the other hand is a density flux through a surface, fluxes from both sides of the surface add-up their photons.

$$E(z) = E_{\mathrm{d}}(z) + E_{\mathrm{u}}(z)$$

The end result is then obtained

$$E(z) = E_{\mathrm{e}0}\, \mathrm{e}^{-\alpha_{\mathrm{e}}(h-z)} + \rho_{\mathrm{e}}\, E_{\mathrm{e}0}\, \mathrm{e}^{-\alpha_{\mathrm{e}}(h+z)} \tag{B.7}$$

B.4. Appendix: Solving for direct photon radiance L_{d}

The direct RTFE describes the fluorescent photon-radiance caused by light beam excitation, and it includes the absorption by the fluorophores and medium. It is the first generation of fluorescent photons. We could, in principle, find the result for all the fluorophores at once. Instead, we look at the solution for one dye. The overall solution is then the sum of all dyes. This is useful, as we can study their individual contributions. Apply now the full solution strategy of section 3.3.1. Start by defining the differential equation describing the system. As the source term, use the $E(z)$ result B.7 in conjunction with the definition of 3.8. Dropping the wavelength dependence λ, see that

$$\cos(\theta)\, \frac{\partial}{\partial z} L_{\mathrm{d}}(z,\theta) + \alpha_{\mathrm{d}} L_{\mathrm{d}}(z,\theta) = \frac{\alpha_{\mathrm{es}}\, q_{\mathrm{d}}}{4\pi} \left[E_0\, \mathrm{e}^{-\alpha_{\mathrm{e}}(h-z)} + E_0\, \rho_{\mathrm{e}}\, \mathrm{e}^{-\alpha_{\mathrm{e}}(h+z)} \right]$$

α_{es} is the individual fluorphore's absorptivity. α_{e} is the combined one of all fluorophores and the medium for the collimated excitation beam. Both are evaluated at the wavelength of excitation: λ_{e}. q_{d} is the fluorophore's specific quantum yield. α_{d} is the combined absorptivity of all dyes and medium. ρ_{d} is reflectivity. These quantities are evaluated at λ. Apply the boundary conditions of no fluorescent light heading into the layer, and the radiance moving away from the mirror equals the reflected downwards radiance

$$\begin{aligned} L_{\mathrm{d}}(h, \Theta_{\mathrm{d}}) &= 0 \\ L_{\mathrm{d}}(0, \Theta_{\mathrm{u}}) &= \rho_{\mathrm{d}}\, \mathcal{R}\{ L_{\mathrm{d}}(0, \Theta_{\mathrm{d}}) \} \end{aligned} \tag{B.8}$$

The integrating factor is

$$\mu(z,\theta) = \mathrm{e}^{\int p(z,\theta)\, \mathrm{d}z}$$
$$\mu(z,\theta) = \mathrm{e}^{\frac{\alpha_{\mathrm{d}} z}{\cos(\theta)}}$$

After applying the solution method with help from MATLAB, the up and down solutions are found

$$
\begin{aligned}
L_{\mathrm{d}}\left(z,\Theta_{\mathrm{u}}\right) = & \frac{E_0\,\alpha_{\mathrm{es}}\,q_{\mathrm{d}}\,\mathrm{e}^{-\alpha_{\mathrm{e}}\left(h-z\right)}}{4\pi\left(\alpha_{\mathrm{d}}+\alpha_{\mathrm{e}}\,\cos\left(\theta\right)\right)} - \frac{E_0\,\alpha_{\mathrm{es}}\,q_{\mathrm{d}}\,\mathrm{e}^{-\alpha_{\mathrm{e}}\,h}\,\mathrm{e}^{-\frac{\alpha_{\mathrm{d}}\,z}{\cos(\theta)}}}{4\pi\left(\alpha_{\mathrm{d}}+\alpha_{\mathrm{e}}\,\cos\left(\theta\right)\right)} \\
& + \frac{E_0\,\alpha_{\mathrm{es}}\,q_{\mathrm{d}}\,\rho_{\mathrm{e}}\,\mathrm{e}^{-\alpha_{\mathrm{e}}\left(h+z\right)}}{4\pi\left(\alpha_{\mathrm{d}}-\alpha_{\mathrm{e}}\,\cos\left(\theta\right)\right)} - \frac{E_0\,\alpha_{\mathrm{es}}\,q_{\mathrm{d}}\,\rho_{\mathrm{d}}\,\mathrm{e}^{-\frac{\alpha_{\mathrm{d}}\left(h+z\right)}{\cos(\theta)}}}{4\pi\left(\alpha_{\mathrm{d}}-\alpha_{\mathrm{e}}\,\cos\left(\theta\right)\right)} \\
& + \frac{E_0\,\alpha_{\mathrm{es}}\,q_{\mathrm{d}}\,\rho_{\mathrm{d}}\,\mathrm{e}^{-\alpha_{\mathrm{e}}\,h}\,\mathrm{e}^{-\frac{\alpha_{\mathrm{d}}\,z}{\cos(\theta)}}}{4\pi\left(\alpha_{\mathrm{d}}-\alpha_{\mathrm{e}}\,\cos\left(\theta\right)\right)} - \frac{E_0\,\alpha_{\mathrm{es}}\,q_{\mathrm{d}}\,\rho_{\mathrm{e}}\,\mathrm{e}^{-\alpha_{\mathrm{e}}\,h}\,\mathrm{e}^{-\frac{\alpha_{\mathrm{d}}\,z}{\cos(\theta)}}}{4\pi\left(\alpha_{\mathrm{d}}-\alpha_{\mathrm{e}}\,\cos\left(\theta\right)\right)} \\
& + \frac{E_0\,\alpha_{\mathrm{es}}\,q_{\mathrm{d}}\,\rho_{\mathrm{d}}\,\rho_{\mathrm{e}}\,\mathrm{e}^{-\alpha_{\mathrm{e}}\,h}\,\mathrm{e}^{-\frac{\alpha_{\mathrm{d}}\,z}{\cos(\theta)}}}{4\pi\left(\alpha_{\mathrm{d}}+\alpha_{\mathrm{e}}\,\cos\left(\theta\right)\right)} - \frac{E_0\,\alpha_{\mathrm{es}}\,q_{\mathrm{d}}\,\rho_{\mathrm{d}}\,\rho_{\mathrm{e}}\,\mathrm{e}^{-4\pi\,\alpha_{\mathrm{e}}\,h}\,\mathrm{e}^{-\frac{\alpha_{\mathrm{d}}\left(h+z\right)}{\cos(\theta)}}}{4\pi\left(\alpha_{\mathrm{d}}+\alpha_{\mathrm{e}}\,\cos\left(\theta\right)\right)}
\end{aligned}
\tag{B.9}
$$

$$
\begin{aligned}
L_{\mathrm{d}}\left(z,\Theta_{\mathrm{d}}\right) = & \frac{E_0\,\alpha_{\mathrm{es}}\,q_{\mathrm{d}}\,\mathrm{e}^{-\alpha_{\mathrm{e}}\left(h-z\right)}}{4\pi\left(\alpha_{\mathrm{d}}+\alpha_{\mathrm{e}}\,\cos\left(\theta\right)\right)} - \frac{E_0\,\alpha_{\mathrm{es}}\,q_{\mathrm{d}}\,\mathrm{e}^{\frac{\alpha_{\mathrm{d}}\left(h-z\right)}{\cos(\theta)}}}{4\pi\left(\alpha_{\mathrm{d}}+\alpha_{\mathrm{e}}\,\cos\left(\theta\right)\right)} \\
& + \frac{E_0\,\alpha_{\mathrm{es}}\,q_{\mathrm{d}}\,\rho_{\mathrm{e}}\,\mathrm{e}^{-\alpha_{\mathrm{e}}\left(h+z\right)}}{4\pi\left(\alpha_{\mathrm{d}}-\alpha_{\mathrm{e}}\,\cos\left(\theta\right)\right)} - \frac{E_0\,\alpha_{\mathrm{es}}\,q_{\mathrm{d}}\,\rho_{\mathrm{e}}\,\mathrm{e}^{\frac{\alpha_{\mathrm{d}}\left(h-z\right)}{\cos(\theta)}-2\,\alpha_{\mathrm{e}}\,h}}{4\pi\left(\alpha_{\mathrm{d}}-\alpha_{\mathrm{e}}\,\cos\left(\theta\right)\right)}
\end{aligned}
\tag{B.10}
$$

B.5. Appendix: Solving for indirect photon radiance L_{i}

The indirect solution describes the second generation of fluorescent photons, who are driven by absorption of the direct generation. Solving for the indirect photon radiance is difficult: the source-term is a complicated integral; thereafter the integrating factor method from 3.3.1 leads to integrands of products between exponential functions and exponential integrals. Lets solve both problems one by one. Once again, we consider the solution to a single dye. The results for all dyes, is the summations of all the dyes' solutions.

B.5.1. Differential equation and boundary conditions

For the indirect photon radiance L_{i} at wavelength λ caused by absorption at λ', define the differential equation

$$
\begin{aligned}
\cos\left(\theta\right)\,\frac{\partial}{\partial z}\,L_{\mathrm{i}}\left(z,\theta\right) &= S_{\mathrm{i}}(z)\,-\alpha_{\mathrm{i}}\,L_{\mathrm{i}}\left(z,\theta\right) \\
S_{\mathrm{i}} &= \frac{q_{\mathrm{i}}\,\alpha_{\mathrm{ds}}}{2}\int_0^{\pi} L_{\mathrm{d}}\left(z,\theta'\right)\,\sin(\theta')\,\mathrm{d}\theta'
\end{aligned}
\tag{B.11}
$$

The source term is fed by the solution of the first generation photons L_{d}. α_{i} is the total absorptivity of all dyes and the medium at wavelength λ. α_{ds} is a dye's specific absorptivity on the direct photon radiance L_{d} at wavelength λ'. q_{i} is the dye's specific quantum yield at wavelength λ. Apply the boundary conditions of no fluorescent light heading into the layer, and the radiance moving away from the mirror equals the reflected downwards radiance

$$
\begin{aligned}
L_{\mathrm{i}}\left(h,\Theta_{\mathrm{d}}\right) &= 0 \\
L_{\mathrm{i}}\left(0,\Theta_{\mathrm{u}}\right) &= \rho_{\mathrm{i}}\,\mathcal{R}\{\,L_{\mathrm{i}}\left(0,\Theta_{\mathrm{d}}\right)\}
\end{aligned}
$$

The integrating factor is

$$
\begin{aligned}
\mu\left(z,\theta\right) &= \mathrm{e}^{\int p(z,\theta)\,\mathrm{i}z} \\
\mu\left(z,\theta\right) &= \mathrm{e}^{\frac{\alpha_{\mathrm{i}}z}{\cos(\theta)}}
\end{aligned}
$$

B.5.2. The source term

S_i, from equation B.11 poses a non-trivial problem for it contains several integrals of the following form

$$\int_0^{\frac{\pi}{2}} \frac{\mathrm{e}^{\frac{-a}{\cos(\theta)}}}{b + c\cos(\theta)} \sin(\theta)\,\mathrm{d}\theta \quad \text{and} \quad \int_{\frac{\pi}{2}}^{\pi} \frac{\mathrm{e}^{\frac{a}{\cos(\theta)}}}{b + c\cos(\theta)} \sin(\theta)\,\mathrm{d}\theta$$

Their solution processes can be found in sections B.8 and B.7, which colliminate in the integration identities of equation B.24 and B.29. The identities are used in MATLAB to solve for the source term. Other integrand terms in there can be found by simple, straightforward integration. The resulting source term is

$$\begin{aligned} S_\mathrm{i} = & \frac{E_0\,\alpha_\mathrm{ds}\,\alpha_\mathrm{es}\,q_\mathrm{d}\,q_\mathrm{i}}{8\pi\,\alpha_\mathrm{e}}\,\Re\Bigg[\ln\left(\frac{\alpha_d+\alpha_e}{\alpha_d-\alpha_e}\right)\left(\mathrm{e}^{-\alpha_e(h-z)}+\rho_e\,\mathrm{e}^{-\alpha_e(h+z)}\right) \\ & +\left(\mathrm{E}_1\left(\alpha_d(h-z)\right)-\mathrm{e}^{-\alpha_e(h-z)}\,\mathrm{E}_1\left((\alpha_d-\alpha_e)(h-z)\right)\right) \\ & +\mathrm{e}^{-\alpha_e h}\left(\mathrm{e}^{\alpha_e z}\,\mathrm{E}_1\left(z(\alpha_d+\alpha_e)\right)-\mathrm{E}_1\left(\alpha_d z\right)\right) \\ & -\rho_d\left(\mathrm{e}^{-\alpha_e(h+z)}\,\mathrm{E}_1\left((h+z)(\alpha_d-\alpha_e)\right)-\mathrm{E}_1\left(\alpha_d(h+z)\right)\right) \\ & +\rho_e\,\mathrm{e}^{-2\alpha_e h}\left(\mathrm{e}^{\alpha_e(h-z)}\,\mathrm{E}_1\left((\alpha_d+\alpha_e)(h-z)\right)-\mathrm{E}_1\left(\alpha_d(h-z)\right)\right) \\ & -\rho_d\,\mathrm{e}^{-\alpha_e h}\left(\mathrm{E}_1\left(\alpha_d z\right)-\mathrm{e}^{-\alpha_e z}\,\mathrm{E}_1\left(z(\alpha_d-\alpha_e)\right)\right) \\ & +\rho_e\,\mathrm{e}^{-\alpha_e h}\left(\mathrm{E}_1\left(\alpha_d z\right)-\mathrm{e}^{-\alpha_e z}\,\mathrm{E}_1\left(z(\alpha_d-\alpha_e)\right)\right) \\ & -\rho_d\,\rho_e\,\mathrm{e}^{-2\alpha_e h}\left(\mathrm{E}_1\left(\alpha_d(h+z)\right)-\mathrm{e}^{\alpha_e(h+z)}\,\mathrm{E}_1\left((\alpha_d+\alpha_e)(h+z)\right)\right) \\ & -\rho_d\,\rho_e\,\mathrm{e}^{-\alpha_e h}\left(\mathrm{e}^{\alpha_e z}\,\mathrm{E}_1\left(z(\alpha_d+\alpha_e)\right)-\mathrm{E}_1\left(\alpha_d z\right)\right)\Bigg] \end{aligned} \tag{B.12}$$

$\Re$ meaning: "select only te real part of". $E_1(\cdot)$ is the so-called exponential integral, as defined by equation B.20.

B.5.3. The general solution for the indirect photon radiance

The general solution can be found by using the source term of B.12 and then applying the solution method of section 3.3. However, there is a problem when using the integrating factor method, equations 3.11, which are repeated here for convenience

$$\begin{aligned} & \frac{\mathrm{d}L(z,\theta)}{\mathrm{d}z} + p(z,\theta)\,L(z,\theta) = q(z,\theta) \\ & L_\mathrm{p}(z,\theta) = \mu^{-1}(z,\theta)\int \mu(z,\theta)\,q(z,\theta)\,\mathrm{d}z + C\mu^{-1}(z,\theta) \\ & \mu(z,\theta) = \mathrm{e}^{\int p(z,\theta)\,\mathrm{d}z} \end{aligned}$$

When we plug in the differential equation B.11, this gives us

$$\begin{aligned} & L_\mathrm{p}(z,\theta) = \mu^{-1}(z,\theta)\int \mu(z,\theta)\,S_\mathrm{i}(z,\theta)\,\mathrm{d}z + C\mu^{-1}(z,\theta) \\ & \mu(z,\theta) = \mathrm{e}^{\frac{\alpha_\mathrm{i} z}{\cos(\theta)}} \end{aligned}$$

This is an indefinite integral with products between $E_1(\pm ax)$ and e^{bx}. In section B.9, solution identities are derived and summarized in equations B.31. They are applied in MATLAB Symbolic Toolbox as an extra set of integration rules. Finally, we are able to formulate the solution of L_i. Although easily obtained by computer algebra, it is not convenient to give the particular solution directly, as it would be very difficult to fit on the page, instead we express it the form of the general solutions $L_\mathrm{g}(z,\Theta_\mathrm{d})$ and $L_\mathrm{g}(z,\Theta_\mathrm{u})$, whose equations 3.13, 3.16 are repeated here

$$L_{\mathrm{p}}(z,\Theta_{\mathrm{d}}) = L_{\mathrm{g}}(z,\Theta_{\mathrm{d}}) - \mu(h,\Theta_{\mathrm{d}})\, L_{\mathrm{g}}(h,\Theta_{\mathrm{d}})\, \mu^{-1}(z,\Theta_{\mathrm{d}})$$
$$L_{\mathrm{p}}(z,\Theta_{\mathrm{u}}) = L_{\mathrm{g}}(z,\Theta_{\mathrm{u}}) + \left[\rho\, \mathcal{R}\{ L_{\mathrm{g}}(0,\Theta_{\mathrm{d}}) - L_{\mathrm{g}}(h,\Theta_{\mathrm{d}})\, \mu(h,\Theta_{\mathrm{d}}) \} - L_{\mathrm{g}}(0,\Theta_{\mathrm{u}}) \right] \mu^{-1}(z,\Theta_{\mathrm{u}})$$

Here is the general solution

$$\begin{aligned}
L_{\mathrm{gi}}(z,\theta) = & \frac{E_0\, \alpha_{\mathrm{ds}}\, \alpha_{\mathrm{es}}\, q_{\mathrm{d}}\, q_{\mathrm{i}}}{8\pi\, \alpha_{\mathrm{e}}} \Re\left[\left(\frac{\mathrm{e}^{-\alpha_{\mathrm{e}}(h-z)}}{\alpha_{\mathrm{i}} + \alpha_{\mathrm{e}}\cos(\theta)} + \frac{\rho_{\mathrm{e}}\, \mathrm{e}^{-\alpha_{\mathrm{e}}(h+z)}}{\alpha_{\mathrm{i}} + \alpha_{\mathrm{e}}\cos(\theta)} \right) \ln\left(\frac{\alpha_{\mathrm{d}} + \alpha_{\mathrm{e}}}{\alpha_{\mathrm{d}} - \alpha_{\mathrm{e}}} \right) \right. \\
& + \frac{\rho_{\mathrm{d}}}{\alpha_{\mathrm{i}}} \left(1 - \rho_{\mathrm{e}}\, \mathrm{e}^{-2\alpha_{\mathrm{e}} h} \right) \mathrm{E}_1(\alpha_{\mathrm{d}}(h+z)) + \frac{\rho_{\mathrm{e}}\, \mathrm{e}^{-(h+z)\alpha_{\mathrm{e}}}}{\alpha_{\mathrm{i}} - \alpha_{\mathrm{e}}\cos(\theta)} \mathrm{E}_1((\alpha_{\mathrm{d}} + \alpha_{\mathrm{e}})(h-z)) \\
& - \frac{\rho_{\mathrm{d}}\, \mathrm{e}^{-(h+z)\alpha_{\mathrm{e}}}}{\alpha_{\mathrm{i}} - \alpha_{\mathrm{e}}\cos(\theta)} \mathrm{E}_1((h+z)(\alpha_{\mathrm{d}} - \alpha_{\mathrm{e}})) + \frac{\mathrm{e}^{-\alpha_{\mathrm{e}} h}}{\alpha_{\mathrm{i}}} (\rho_{\mathrm{e}} - \rho_{\mathrm{d}} - 1 + \rho_{\mathrm{d}}\, \rho_{\mathrm{e}})\, \mathrm{E}_1(\alpha_{\mathrm{d}} z) \\
& + \frac{(\rho_{\mathrm{d}} - \rho_{\mathrm{e}})\, \mathrm{e}^{-\alpha_{\mathrm{e}}(h+z)}}{\alpha_{\mathrm{i}} - \alpha_{\mathrm{e}}\cos(\theta)} \mathrm{E}_1(z(\alpha_{\mathrm{d}} - \alpha_{\mathrm{e}})) + \frac{\left(1 - \rho_{\mathrm{e}}\, \mathrm{e}^{-2\alpha_{\mathrm{e}} h}\right)}{\alpha_{\mathrm{i}}} \mathrm{E}_1(\alpha_{\mathrm{d}}(h-z)) \\
& - \frac{\mathrm{e}^{-(h-z)\alpha_{\mathrm{e}}}}{\alpha_{\mathrm{i}} + \alpha_{\mathrm{e}}\cos(\theta)} \mathrm{E}_1((\alpha_{\mathrm{d}} - \alpha_{\mathrm{e}})(h-z)) + \frac{\rho_{\mathrm{d}}\, \rho_{\mathrm{e}}\, \mathrm{e}^{-\alpha_{\mathrm{e}}(h-z)}}{\alpha_{\mathrm{i}} + \alpha_{\mathrm{e}}\cos(\theta)} \mathrm{E}_1((\alpha_{\mathrm{d}} + \alpha_{\mathrm{e}})(h+z)) \\
& + \left(\frac{1 + \rho_{\mathrm{d}} - \rho_{\mathrm{e}} - \rho_{\mathrm{d}}\rho_{\mathrm{e}}}{\alpha_{\mathrm{i}}} - \frac{1 - \rho_{\mathrm{d}}\, \rho_{\mathrm{e}}}{\alpha_{\mathrm{i}} + \alpha_{\mathrm{e}}\cos(\theta)} - \frac{\rho_{\mathrm{d}} - \rho_{\mathrm{e}}}{\alpha_{\mathrm{i}} - \alpha_{\mathrm{e}}\cos(\theta)} \right) \mathrm{e}^{-\alpha_{\mathrm{e}} h - \frac{\alpha_{\mathrm{i}} z}{\cos(\theta)}}\, \mathrm{E}_1\left(z\left(\alpha_{\mathrm{d}} - \frac{\alpha_{\mathrm{i}}}{\cos(\theta)} \right) \right) \\
& + \left(\frac{1}{\alpha_{\mathrm{i}} + \alpha_{\mathrm{e}}\cos(\theta)} - \frac{\rho_{\mathrm{e}}\, \mathrm{e}^{-2\alpha_{\mathrm{e}} h}}{\alpha_{\mathrm{i}} - \alpha_{\mathrm{e}}\cos(\theta)} + \frac{\rho_{\mathrm{e}}\, \mathrm{e}^{-2\alpha_{\mathrm{e}} h} - 1}{\alpha_{\mathrm{i}}} \right) \mathrm{e}^{-\frac{\alpha_{\mathrm{i}}(z-h)}{\cos(\theta)}}\, \mathrm{E}_1\left((h-z)\left(\alpha_{\mathrm{d}} + \frac{\alpha_{\mathrm{i}}}{\cos(\theta)} \right) \right) \\
& + \rho_{\mathrm{d}} \left(\frac{1}{\alpha_{\mathrm{i}} - \alpha_{\mathrm{e}}\cos(\theta)} - \frac{1}{\alpha_{\mathrm{i}}} - \frac{\rho_{\mathrm{e}}\, \mathrm{e}^{-2\alpha_{\mathrm{e}} h}}{\alpha_{\mathrm{i}} + \alpha_{\mathrm{e}}\cos(\theta)} + \frac{\rho_{\mathrm{e}}\, \mathrm{e}^{-2\alpha_{\mathrm{e}} h}}{\alpha_{\mathrm{i}}} \right) \mathrm{e}^{-\frac{\alpha_{\mathrm{i}}(h+z)}{\cos(\theta)}}\, \mathrm{E}_1\left((h+z)\left(\alpha_{\mathrm{d}} - \frac{\alpha_{\mathrm{i}}}{\cos(\theta)} \right) \right) \\
& \left. + \frac{(1 - \rho_{\mathrm{d}}\rho_{\mathrm{e}})\, \mathrm{e}^{-\alpha_{\mathrm{e}}(h-z)}}{\alpha_{\mathrm{i}} + \alpha_{\mathrm{e}}\cos(\theta)} \mathrm{E}_1(z(\alpha_{\mathrm{d}} + \alpha_{\mathrm{e}})) \right]
\end{aligned} \tag{B.13}$$

Here is the $z = 0$ limit

$$\begin{aligned}
L_{\mathrm{gi}}(0,\theta) = & \frac{E_0\, \alpha_{\mathrm{ds}}\, \alpha_{\mathrm{es}}\, q_{\mathrm{d}}\, q_{\mathrm{i}}}{8\pi\, \alpha_{\mathrm{e}}} \Re\left[(1 + \rho_d - \rho_{\mathrm{e}} - \rho_d\, \rho_{\mathrm{e}}) \frac{\mathrm{e}^{-\alpha_{\mathrm{e}} h}}{\alpha_{\mathrm{i}}} \ln(\alpha_{\mathrm{d}}) \right. \\
& + \left(\frac{\rho_{\mathrm{e}}}{\alpha_{\mathrm{i}} - \alpha_{\mathrm{e}}\cos(\theta)} + \frac{\rho_d\, \rho_{\mathrm{e}}}{\alpha_{\mathrm{i}} + \alpha_{\mathrm{e}}\cos(\theta)} \right) \mathrm{e}^{-\alpha_{\mathrm{e}} h} \ln(\alpha_{\mathrm{d}} + \alpha_{\mathrm{e}}) \\
& - \left(\frac{1}{\alpha_{\mathrm{i}} + \alpha_{\mathrm{e}}\cos(\theta)} + \frac{\rho_d}{\alpha_{\mathrm{i}} - \alpha_{\mathrm{e}}\cos(\theta)} \right) \mathrm{e}^{-\alpha_{\mathrm{e}} h} \ln(\alpha_{\mathrm{d}} - \alpha_{\mathrm{e}}) \\
& + \left(\frac{1 - \rho_d\, \rho_{\mathrm{e}}}{\alpha_{\mathrm{i}} + \alpha_{\mathrm{e}}\cos(\theta)} + \frac{\rho_d - \rho_{\mathrm{e}}}{\alpha_{\mathrm{i}} - \alpha_{\mathrm{e}}\cos(\theta)} + \frac{-1 - \rho_d + \rho_{\mathrm{e}} + \rho_d\, \rho_{\mathrm{e}}}{\alpha_{\mathrm{i}}} \right) \mathrm{e}^{-\alpha_{\mathrm{e}} h} \ln\left(\alpha_{\mathrm{d}} - \frac{\alpha_{\mathrm{i}}}{\cos(\theta)} \right) \\
& + \frac{1}{\alpha_{\mathrm{i}}} \left(1 + \rho_{\mathrm{d}} - \rho_{\mathrm{e}}\, \mathrm{e}^{-2\alpha_{\mathrm{e}} h} - \rho_{\mathrm{d}}\, \rho_{\mathrm{e}}\, \mathrm{e}^{-2\alpha_{\mathrm{e}} h} \right) \mathrm{E}_1(\alpha_{\mathrm{d}} h) \\
& - \left(\frac{1}{\alpha_{\mathrm{i}} + \alpha_{\mathrm{e}}\cos(\theta)} + \frac{\rho_{\mathrm{d}}}{\alpha_{\mathrm{i}} - \alpha_{\mathrm{e}}\cos(\theta)} \right) \mathrm{e}^{-h\alpha_{\mathrm{e}}}\, \mathrm{E}_1((\alpha_{\mathrm{d}} - \alpha_{\mathrm{e}})\, h) \\
& + \left(\frac{\rho_{\mathrm{e}}}{\alpha_{\mathrm{i}} - \alpha_{\mathrm{e}}\cos(\theta)} + \frac{\rho_{\mathrm{d}}\, \rho_{\mathrm{e}}}{\alpha_{\mathrm{i}} + \alpha_{\mathrm{e}}\cos(\theta)} \right) \mathrm{e}^{-\alpha_{\mathrm{e}} h}\, \mathrm{E}_1((\alpha_{\mathrm{d}} + \alpha_{\mathrm{e}})\, h) \\
& + \left(\frac{1}{\alpha_{\mathrm{i}} + \alpha_{\mathrm{e}}\cos(\theta)} - \frac{\rho_{\mathrm{e}}\, \mathrm{e}^{-2\alpha_{\mathrm{e}} h}}{\alpha_{\mathrm{i}} - \alpha_{\mathrm{e}}\cos(\theta)} + \frac{\rho_{\mathrm{e}}\, \mathrm{e}^{-2\alpha_{\mathrm{e}} h} - 1}{\alpha_{\mathrm{i}}} \right) \mathrm{e}^{\frac{\alpha_{\mathrm{i}} h}{\cos(\theta)}}\, \mathrm{E}_1\left(h\left(\alpha_{\mathrm{d}} + \frac{\alpha_{\mathrm{i}}}{\cos(\theta)} \right) \right) \\
& \left. + \rho_{\mathrm{d}} \left(\frac{1}{\alpha_{\mathrm{i}} - \alpha_{\mathrm{e}}\cos(\theta)} - \frac{1}{\alpha_{\mathrm{i}}} - \frac{\rho_{\mathrm{e}}\, \mathrm{e}^{-2\alpha_{\mathrm{e}} h}}{\alpha_{\mathrm{i}} + \alpha_{\mathrm{e}}\cos(\theta)} + \frac{\rho_{\mathrm{e}}\, \mathrm{e}^{-2\alpha_{\mathrm{e}} h}}{\alpha_{\mathrm{i}}} \right) \mathrm{e}^{-\frac{\alpha_{\mathrm{i}} h}{\cos(\theta)}}\, \mathrm{E}_1\left(h\left(\alpha_{\mathrm{d}} - \frac{\alpha_{\mathrm{i}}}{\cos(\theta)} \right) \right) \right]
\end{aligned} \tag{B.14}$$

And here is the limit for $z = h$

$$
\begin{aligned}
L_{\mathrm{gi}}(h,\theta) = & \frac{E_0\, a_{\mathrm{ds}}\, a_{\mathrm{es}}\, q_\mathrm{d}\, q_\mathrm{i}}{8\pi\, \alpha_\mathrm{e}} \Re\left[\frac{\rho_\mathrm{e}\, \mathrm{e}^{-2\,\alpha_\mathrm{e}\, h} - 1}{\alpha_\mathrm{i}} \ln(a_\mathrm{d}) + \frac{1}{\alpha_\mathrm{i} + \alpha_\mathrm{e}\, \cos(\theta)}\, \ln(a_\mathrm{d} + \alpha_\mathrm{e}) \right. \\
& - \frac{\rho_\mathrm{e}\, \mathrm{e}^{-2\,\alpha_\mathrm{e}\, h}}{\alpha_\mathrm{i} - \alpha_\mathrm{e}\, \cos(\theta)}\, \ln(a_\mathrm{d} - \alpha_\mathrm{e}) \\
& + \left(\frac{1 - \rho_\mathrm{e}\, \mathrm{e}^{-2\,\alpha_\mathrm{e}\, h}}{\alpha_\mathrm{i}} - \frac{1}{\alpha_\mathrm{i} + \alpha_\mathrm{e}\, \cos(\theta)} + \frac{\rho_\mathrm{e}\, \mathrm{e}^{-2\,\alpha_\mathrm{e}\, h}}{\alpha_\mathrm{i} - \alpha_\mathrm{e}\, \cos(\theta)} \right) \ln\left(a_\mathrm{d} + \frac{\alpha_\mathrm{i}}{\cos(\theta)} \right) \\
& - \frac{\rho_\mathrm{d}\, \mathrm{e}^{-2\,\alpha_\mathrm{e} h}}{\alpha_\mathrm{i} - \alpha_\mathrm{e}\, \cos(\theta)}\, \mathrm{E}_1(2\,(a_\mathrm{d} - \alpha_\mathrm{e})h) \; + \; \frac{\mathrm{e}^{-\alpha_\mathrm{e}\, h}}{\alpha_\mathrm{i}} (\rho_\mathrm{e} - \rho_\mathrm{d} - 1 + \rho_\mathrm{d}\, \rho_\mathrm{e})\, \mathrm{E}_1(a_\mathrm{d}\, h) \\
& + \frac{(\rho_\mathrm{d} - \rho_\mathrm{e})\, \mathrm{e}^{-\alpha_\mathrm{e}\, 2\, h}}{\alpha_\mathrm{i} - \alpha_\mathrm{e}\, \cos(\theta)} \mathrm{E}_1(h\,(a_\mathrm{d} - \alpha_\mathrm{e})) + \frac{(1 - \rho_\mathrm{d}\rho_\mathrm{e})}{\alpha_\mathrm{i} + \alpha_\mathrm{e}\, \cos(\theta)}\, \mathrm{E}_1(h\,(a_\mathrm{d} + \alpha_\mathrm{e})) \\
& + \frac{\rho_\mathrm{d}\, \rho_\mathrm{e}}{\alpha_\mathrm{i} + \alpha_\mathrm{e}\, \cos(\theta)}\, \mathrm{E}_1(2\,(a_\mathrm{d} + \alpha_\mathrm{e})\, h) + \frac{\rho_\mathrm{d}}{\alpha_\mathrm{i}} \left(1 - \rho_\mathrm{e}\, \mathrm{e}^{-2\,\alpha_\mathrm{e}\, h} \right) \mathrm{E}_1(2 a_\mathrm{d}\, h) \\
& + \rho_\mathrm{d} \left(\frac{1}{\alpha_\mathrm{i} - \alpha_\mathrm{e}\, \cos(\theta)} - \frac{1}{\alpha_\mathrm{i}} - \frac{\rho_\mathrm{e}\, \mathrm{e}^{-2\,\alpha_\mathrm{e}\, h}}{\alpha_\mathrm{i} + \alpha_\mathrm{e}\, \cos(\theta)} + \frac{\rho_\mathrm{e}\, \mathrm{e}^{-2\,\alpha_\mathrm{e}\, h}}{\alpha_\mathrm{i}} \right) \mathrm{e}^{-\frac{2\,\alpha_\mathrm{i}\, h}{\cos(\theta)}}\, \mathrm{E}_1\left(2h \left(a_\mathrm{d} - \frac{\alpha_\mathrm{i}}{\cos(\theta)} \right) \right) \\
& \left. + \left(\frac{1 + \rho_\mathrm{d} - \rho_\mathrm{e} - \rho_\mathrm{d}\rho_\mathrm{e}}{\alpha_\mathrm{i}} - \frac{1 - \rho_\mathrm{d}\, \rho_\mathrm{e}}{\alpha_\mathrm{i} + \alpha_\mathrm{e}\, \cos(\theta)} - \frac{\rho_\mathrm{d} - \rho_\mathrm{e}}{\alpha_\mathrm{i} - \alpha_\mathrm{e}\, \cos(\theta)} \right) \mathrm{e}^{-\alpha_\mathrm{e}\, h - \frac{\alpha_\mathrm{i}\, h}{\cos(\theta)}}\, \mathrm{E}_1\left(h \left(a_\mathrm{d} - \frac{\alpha_\mathrm{i}}{\cos(\theta)} \right) \right) \right]
\end{aligned}
\tag{B.15}
$$

B.6. Appendix: Special and limit cases of the L_d and L_i solution

The L_d and L_i solution cannot be directly applied to a numerical computation scheme, as there are some absorption coefficient combinations that break-down the solutions. For the L_d solution, see equations B.9 and B.10, it are the denominator terms becoming zero for $\alpha_\mathrm{d} = \pm\alpha_\mathrm{e} \cos(\theta)$. Luckily, in practical calculations this situation did not occur and is therefore ignored for now. However, L_i terms should be treated more carefully. The building blocks of the solution, see B.13, B.14 and B.15 have some peculiar aspects. Firstly, the α_d term cannot be zero, as there would be no photon input to ”force” the differential equation, which may return NaN when applied in a numerical scheme as E_1's arguments are zero. Secondly, α_i can be zero, which leads to division by zero while a physically valid solution actually does exist: it means that emitted photons do not get re-absorbed. To solve both cases, any calculation schema needs to skip the cases where $\alpha_\mathrm{d} = 0$, and for $\alpha_\mathrm{i} = 0$ we need to take the limit and use that result to calculate the propor photon radiance. To wit, using a computer algebra program, the proper limits are

The general solution

$$
\begin{aligned}
L_{\mathrm{gi},0}(z,\theta) = & \frac{E_0\, \alpha_{\mathrm{ds}}\, \alpha_{\mathrm{es}}\, q_\mathrm{d}\, q_\mathrm{i}}{8\pi\, \alpha_\mathrm{e}^2 \cos(\theta)} \Re\left[(\mathrm{e}^{-\alpha_\mathrm{e}(h-z)} - \rho_\mathrm{e}\mathrm{e}^{-\alpha_\mathrm{e}(h+z)}) \ln\left(\frac{\alpha_\mathrm{d} + \alpha_\mathrm{e}}{\alpha_\mathrm{d} - \alpha_\mathrm{e}} \right) \right. \\
& + \frac{\alpha_\mathrm{e}}{\alpha_\mathrm{d}} \left(\mathrm{e}^{-\alpha_\mathrm{d}(h-z)} + \mathrm{e}^{-\alpha_\mathrm{e}h - \alpha_\mathrm{d}z} - \rho_\mathrm{d}\mathrm{e}^{-\alpha_\mathrm{d}(h+z)} + \rho_\mathrm{d}\mathrm{e}^{-\alpha_\mathrm{e}h - \alpha_\mathrm{d}z} - \rho_\mathrm{e}\mathrm{e}^{-\alpha_\mathrm{e}h - \alpha_\mathrm{d}z} \right. \\
& \left. - \rho_\mathrm{e}\mathrm{e}^{-2\alpha_\mathrm{e}h - \alpha_\mathrm{d}(h-z)} - \rho_\mathrm{d} red\mathrm{e}^{-\alpha_\mathrm{e}h - \alpha_\mathrm{d}z} + \rho_\mathrm{d}\rho_\mathrm{e}\mathrm{e}^{-\alpha_\mathrm{d}(h+z) - 2\alpha_\mathrm{e}h} \right) \\
& + (1 - \rho_\mathrm{d}\rho_\mathrm{e})\mathrm{e}^{-\alpha_\mathrm{e}(h-z)} \mathrm{E}_1((\alpha_\mathrm{d} + \alpha_\mathrm{e})z) + \rho_\mathrm{d}\rho_\mathrm{e}\mathrm{e}^{-\alpha_\mathrm{e}(h-z)} \mathrm{E}_1((\alpha_\mathrm{d} + \alpha_\mathrm{e})(h+z)) \\
& + \left(1 - \alpha_\mathrm{e}(h-z) + \rho_\mathrm{e}\mathrm{e}^{-2\alpha_\mathrm{e}h} \alpha_\mathrm{e}\rho_\mathrm{e}\mathrm{e}^{-2\alpha_\mathrm{e}h}(h-z) \right) \mathrm{E}_1(\alpha_\mathrm{d}(h-z)) \\
& + (\rho_\mathrm{d} - \rho_\mathrm{e})\mathrm{e}^{-\alpha_\mathrm{e}(h+z)} \mathrm{E}_1((\alpha_\mathrm{d} - \alpha_\mathrm{e})z) - \mathrm{e}^{-\alpha_\mathrm{e}(h-z)} \mathrm{E}_1((\alpha_\mathrm{d} - \alpha_\mathrm{e})(h-z)) \\
& - \rho_\mathrm{e}\mathrm{e}^{-\alpha_\mathrm{e}(h+z)} \mathrm{E}_1(\alpha_\mathrm{d}(h+z)) + \rho_\mathrm{d}\mathrm{e}^{-\alpha_\mathrm{e}(h+z)} \mathrm{E}_1((\alpha_\mathrm{d} - \alpha_\mathrm{e})(h+z)) \\
& + (\rho_\mathrm{d} - 1 - \rho_\mathrm{e} - \alpha_\mathrm{e}z + \rho_\mathrm{d}\rho_\mathrm{e} - \alpha_\mathrm{e}\rho_\mathrm{d}z + \alpha_\mathrm{e}\rho_\mathrm{e}z + \alpha_\mathrm{e}\rho_\mathrm{d}\rho_\mathrm{e}z)\, \mathrm{e}^{-\alpha_\mathrm{e}h} \mathrm{E}_1(\alpha_\mathrm{d}z) \\
& \left. + \left(\alpha_\mathrm{e}\rho_\mathrm{d}(h+z) - \rho_\mathrm{d} - \rho_\mathrm{d}\rho_\mathrm{e}\mathrm{e}^{-2\alpha_\mathrm{e}h} - \rho_\mathrm{d}\rho_\mathrm{e}\alpha_\mathrm{e}\mathrm{e}^{-2\alpha_\mathrm{e}h}(h+z) \right) \mathrm{E}_1(\alpha_\mathrm{d}(h+z)) \right]
\end{aligned}
\tag{B.16}
$$

The $z = 0$ limit

$$
\begin{aligned}
L_{\mathrm{gi},0}\,(0,\theta) =& \frac{E_0\,\alpha_{\mathrm{ds}}\,\alpha_{\mathrm{es}}\,q_{\mathrm{d}}\,q_{\mathrm{i}}}{8\pi\,\alpha_{\mathrm{e}}^2\cos\,(\theta)}\,\Re\left[(\rho_{\mathrm{d}}\rho_{\mathrm{e}}-\rho_{\mathrm{e}})\mathrm{e}^{-\alpha_{\mathrm{e}}h}\mathrm{E}_1((\alpha_{\mathrm{d}}-\alpha_{\mathrm{e}})h)+(\rho_{\mathrm{d}}-1)\mathrm{e}^{-\alpha_{\mathrm{e}}h}\mathrm{E}_1((\alpha_{\mathrm{d}}+\alpha_{\mathrm{e}})h)\right.\\
&+(1-\alpha_{\mathrm{e}}h-\rho_{\mathrm{d}}+\alpha_{\mathrm{e}}\rho_{\mathrm{d}}h+\rho_{\mathrm{e}}\mathrm{e}^{-2\alpha_{\mathrm{e}}h}+\alpha_{\mathrm{e}}\rho_{\mathrm{e}}h\mathrm{e}^{-2\alpha_{\mathrm{e}}h}-\rho_{\mathrm{d}}\rho_{\mathrm{e}}\mathrm{e}^{-2\alpha_{\mathrm{e}}h}-\alpha_{\mathrm{e}}\rho_{\mathrm{d}}\rho_{\mathrm{e}}h\mathrm{e}^{-2\alpha_{\mathrm{e}}h})\mathrm{E}_1(\alpha_{\mathrm{d}}h)\\
&+(1-\rho_{\mathrm{d}}+\rho_{\mathrm{e}}-\rho_{\mathrm{d}}\rho_{\mathrm{e}})\mathrm{e}^{-\alpha_{\mathrm{e}}h}\ln(\alpha_{\mathrm{d}})+(\rho_{\mathrm{d}}\rho_{\mathrm{e}}-\rho_{\mathrm{e}})\mathrm{e}^{-\alpha_{\mathrm{e}}h}\ln(\alpha_{\mathrm{d}}+\alpha_{\mathrm{e}})+(\rho_{\mathrm{d}}-1)\mathrm{e}^{-\alpha_{\mathrm{e}}h}\ln(\alpha_{\mathrm{d}}-\alpha_{\mathrm{e}})\\
&+\frac{\alpha_{\mathrm{e}}}{\alpha_{\mathrm{d}}}\left(\mathrm{e}^{-\alpha_{\mathrm{d}}h}+\mathrm{e}^{-\alpha_{\mathrm{e}}h}-\rho_{\mathrm{d}}\mathrm{e}^{-\alpha_{\mathrm{d}}h}+\rho_{\mathrm{d}}\mathrm{e}^{-\alpha_{\mathrm{e}}h}-\rho_{\mathrm{e}}\mathrm{e}^{-\alpha_{\mathrm{e}}h}-\rho_{\mathrm{d}}\rho_{\mathrm{e}}\mathrm{e}^{-\alpha_{\mathrm{e}}h}-\rho_{\mathrm{e}}\mathrm{e}^{-\alpha_{\mathrm{d}}h}\mathrm{e}^{-2\alpha_{\mathrm{e}}h}\right.\\
&\left.\left.+\ \rho_{\mathrm{d}}\rho_{\mathrm{e}}\mathrm{e}^{-\alpha_{\mathrm{d}}h}\mathrm{e}^{-2\alpha_{\mathrm{e}}h}\right)\right]
\end{aligned}
\tag{B.17}
$$

The $z = h$ limit

$$
\begin{aligned}
L_{\mathrm{gi},0}\,(h,\theta) =& \frac{E_0\,\alpha_{\mathrm{ds}}\,\alpha_{\mathrm{es}}\,q_{\mathrm{d}}\,q_{\mathrm{i}}}{8\pi\,\alpha_{\mathrm{e}}^2\cos(\theta)}\,\Re\left[(-1-\rho_{\mathrm{e}}\mathrm{e}^{-2\alpha_{\mathrm{e}}h})\ln(\alpha_{\mathrm{d}})+\ln(\alpha_{\mathrm{d}}+\alpha_{\mathrm{e}})-\rho_{\mathrm{e}}\mathrm{e}^{-2\alpha_{\mathrm{e}}h}\ln(\alpha_{\mathrm{d}}-\alpha_{\mathrm{e}})\right.\\
&+(\rho_{\mathrm{e}}-\rho_{\mathrm{d}})\mathrm{e}^{-2\alpha_{\mathrm{e}}h}\mathrm{E}_1((\alpha_{\mathrm{d}}-\alpha_{\mathrm{e}})h)+\rho_{\mathrm{d}}\mathrm{e}^{-2\alpha_{\mathrm{e}}h}\mathrm{E}_1(2(\alpha_{\mathrm{d}}-\alpha_{\mathrm{e}})h)+(1-\rho_{\mathrm{d}}\rho_{\mathrm{e}})\mathrm{E}_1((\alpha_{\mathrm{d}}+\alpha_{\mathrm{e}})h)\\
&+(2ae\rho_{\mathrm{d}}h-\rho_{\mathrm{d}}-\rho_{\mathrm{d}}\rho_{\mathrm{e}}\mathrm{e}^{-2\alpha_{\mathrm{e}}h}-2\alpha_{\mathrm{e}}\rho_{\mathrm{d}}\rho_{\mathrm{e}}h\mathrm{e}^{-2\alpha_{\mathrm{e}}h})\mathrm{E}_1(2adh)+\rho_{\mathrm{d}}\rho_{\mathrm{e}}\mathrm{E}_1(2(\alpha_{\mathrm{d}}+\alpha_{\mathrm{e}})h)\\
&+(\rho_{\mathrm{d}}-\alpha_{\mathrm{e}}h-1-\rho_{\mathrm{e}}-\alpha_{\mathrm{e}}\rho_{\mathrm{d}}h+\alpha_{\mathrm{e}}\rho_{\mathrm{e}}h+\rho_{\mathrm{d}}\rho_{\mathrm{e}}+\alpha_{\mathrm{e}}\rho_{\mathrm{d}}\rho_{\mathrm{e}}h)\mathrm{e}^{-\alpha_{\mathrm{e}}h}\mathrm{E}_1(\alpha_{\mathrm{d}}h)\\
&+\frac{\alpha_{\mathrm{e}}}{\alpha_{\mathrm{d}}}\left(1-\rho_{\mathrm{d}}\mathrm{e}^{-2\alpha_{\mathrm{d}}h}-\rho_{\mathrm{e}}\mathrm{e}^{-2\alpha_{\mathrm{e}}h}+\mathrm{e}^{-\alpha_{\mathrm{d}}h}\mathrm{e}^{-\alpha_{\mathrm{e}}h}+\rho_{\mathrm{d}}\mathrm{e}^{-\alpha_{\mathrm{d}}h}\mathrm{e}^{-\alpha_{\mathrm{e}}h}-\rho_{\mathrm{e}}\mathrm{e}^{-\alpha_{\mathrm{d}}h}\mathrm{e}^{-\alpha_{\mathrm{e}}h}-\rho_{\mathrm{d}}\rho_{\mathrm{e}}\mathrm{e}^{-\alpha_{\mathrm{d}}h}\mathrm{e}^{-\alpha_{\mathrm{e}}h}\right.\\
&\left.\left.+\ \rho_{\mathrm{d}}\rho_{\mathrm{e}}\mathrm{e}^{-2adh}\mathrm{e}^{-2aeh}\right)\right]
\end{aligned}
\tag{B.18}
$$

All limits are the building blocks to construct the particular solution as outlined in section 3.3.

B.7. Appendix: Upper hemisphere identity for the source-term integral

Many terms in the upper hemisphere source term integral of the FRTE can be solved after some manipulation. Computer Algebra systems will find those readily. However, some terms do not have an obvious solution, so an integration identity for those is developed. First, the case without a singularity is considered. Second, the case with a pole is investigated. Third, the results are combined into a single identity.

B.7.1. Identity in absence of a denominator singularity

Ignoring constants, the problematic upper hemisphere integrals have the following form

$$
\begin{aligned}
&\int_0^{\frac{\pi}{2}} \frac{\mathrm{e}^{\frac{-a}{\cos(\theta)}}}{b+c\cos\,(\theta)}\sin\,(\theta)\,\mathrm{d}\theta\\
&\{a,b\in\mathbb{R}\,|\,a,b>0\}\\
&\{c\in\mathbb{R}\,|\,c\neq 0\}\\
&b+c\cos(\theta)>0
\end{aligned}
\tag{B.19}
$$

Use substitution $t = \cos\,(\theta)$ and $\mathrm{d}t = -\sin\,(\theta)\,\mathrm{d}\theta$ to obtain

$$
\int_0^1 \frac{\mathrm{e}^{\frac{-a}{t}}}{b+ct}\mathrm{d}t
$$

Notice the change of upper- and lower boundary. Now use $t = \frac{1}{u}$ and $\mathrm{d}t = -\frac{1}{u^2}\mathrm{d}u$

$$\int_1^\infty \frac{\mathrm{e}^{-au}}{u(bu+c)}\mathrm{d}u$$

A partial fraction expansion is applied

$$\frac{1}{c}\int_1^\infty \frac{\mathrm{e}^{-au}}{u} - \frac{b\mathrm{e}^{-au}}{bu+c}\mathrm{d}u$$

Apply the substitution $u = \frac{t}{a}$, $\mathrm{d}u = \frac{\mathrm{d}t}{a}$

$$\frac{1}{c}\int_a^\infty \frac{\mathrm{e}^{-t}}{t}\mathrm{d}t - \frac{b}{c}\int_a^\infty \frac{\mathrm{e}^{-t}}{bt+ac}\mathrm{d}t$$

At last, use $t = v - \frac{ac}{b}$ with $\mathrm{d}t = \mathrm{d}v$

$$\frac{1}{c}\int_a^\infty \frac{\mathrm{e}^{-t}}{t}\mathrm{d}t - \frac{\mathrm{e}^{\frac{ac}{b}}}{c}\int_{a+\frac{ac}{b}}^\infty \frac{\mathrm{e}^{-v}}{v}\mathrm{d}v$$

These are so-called exponential integrals, see [3, Eq. 6.2.1], whose *pricipal value* is defined as

$$\mathrm{E}_1(z) = \int_z^\infty \frac{\mathrm{e}^{-t}}{t}\mathrm{d}t \quad z \in \mathbb{C}\setminus 0 \tag{B.20}$$

Where z is complex, but does not include the origin. It has no known analytic solution, yet is a well-studied function that regularly pops-up in radiative transfer problems. The final result is

$$\begin{aligned}&\int_0^{\frac{\pi}{2}} \frac{\mathrm{e}^{\frac{-a}{\cos(\theta)}}}{b+c\cos(\theta)}\sin(\theta)\,\mathrm{d}\theta = \frac{1}{c}\left(\mathrm{E}_1(a) - \mathrm{e}^{\frac{ac}{b}}\,\mathrm{E}_1\left(a+\frac{ac}{b}\right)\right)\\ &\{a,b\in\mathbb{R}\,|\,a,b>0\}\\ &\{c\in\mathbb{R}\,|\,c\neq 0\}\\ &b+c\cos(\theta)>0\end{aligned} \tag{B.21}$$

B.7.2. Identity in presence of a denominator singularity

Reconsider equation B.19, but now without the condition of positivity on the denominator

$$\begin{aligned}&\int_0^{\frac{\pi}{2}} \frac{\mathrm{e}^{\frac{-a}{\cos(\theta)}}}{b+c\cos(\theta)}\sin(\theta)\,\mathrm{d}\theta\\ &\{a,b\in\mathbb{R}\,|\,a,b>0\}\\ &\{c\in\mathbb{R}\,|\,c\neq 0\}\end{aligned}$$

now $b + c\cos(\theta)$ is somewhere positive and somewhere negative on the open domain of $\theta \in 0, \frac{\pi}{2}$, thus $c < 0$ and $|c| > |b|$. This all leads to the existence of a pole in the denominator and the integral is improper, so solve it by assigning a Cauchy principal value; to start

$$\lim_{\epsilon\to 0^+}\left[\int_0^{\arccos\left(\frac{-b}{c}\right)-\epsilon} \frac{\mathrm{e}^{\frac{-a}{\cos(\theta)}}}{b+c\cos(\theta)}\sin(\theta)\,\mathrm{d}\theta + \int_{\arccos\left(\frac{-b}{c}\right)+\epsilon}^{\frac{\pi}{2}} \frac{\mathrm{e}^{\frac{-a}{\cos(\theta)}}}{b+c\cos(\theta)}\sin(\theta)\,\mathrm{d}\theta\right]$$

Apply u-substitution $t = \cos(\theta)$, $\mathrm{d}t = -\sin(\theta)\,\mathrm{d}\theta$ and introduce the following abbreviations $f(-\epsilon) = \cos\left(\arccos\left(\frac{-b}{c}\right) - \epsilon\right)$ and $f(\epsilon) = \cos\left(\arccos\left(\frac{-b}{c}\right) + \epsilon\right)$

$$\lim_{\epsilon \to 0^+} \left[\int_{f(-\epsilon)}^{1} \frac{\mathrm{e}^{\frac{-a}{t}}}{b + ct} \mathrm{d}t + \int_{0}^{f(\epsilon)} \frac{\mathrm{e}^{\frac{-a}{t}}}{b + ct} \mathrm{d}t \right]$$

Now use $t = \frac{1}{u}$ and $\mathrm{d}t = -\frac{1}{u^2}\mathrm{d}u$ to see that

$$\lim_{\epsilon \to 0^+} \left[\int_{1}^{\frac{1}{f(-\epsilon)}} \frac{\mathrm{e}^{-au}}{u(bu + c)} \mathrm{d}u + \int_{\frac{1}{f(\epsilon)}}^{\infty} \frac{\mathrm{e}^{-au}}{u(bu + c)} \mathrm{d}u \right]$$

A partial fraction expansion is applied

$$\lim_{\epsilon \to 0^+} \left[\frac{1}{c} \int_{1}^{\frac{1}{f(-\epsilon)}} \frac{\mathrm{e}^{-au}}{u} - \frac{b\mathrm{e}^{-au}}{bu + c} \mathrm{d}u + \frac{1}{c} \int_{\frac{1}{f(\epsilon)}}^{\infty} \frac{\mathrm{e}^{-au}}{u} - \frac{b\mathrm{e}^{-au}}{bu + c} \mathrm{d}u \right]$$

Now use this substitution $u = \frac{t}{a}$, $\mathrm{d}u = \frac{\mathrm{d}t}{a}$

$$\lim_{\epsilon \to 0^+} \left[\frac{1}{c} \int_{a}^{\frac{a}{f(-\epsilon)}} \frac{\mathrm{e}^{-t}}{t} \mathrm{d}t - \frac{b}{c} \int_{a}^{\frac{a}{f(-\epsilon)}} \frac{\mathrm{e}^{-t}}{bt + ac} \mathrm{d}t + \frac{1}{c} \int_{\frac{a}{f(\epsilon)}}^{\infty} \frac{\mathrm{e}^{-t}}{t} \mathrm{d}t - \frac{b}{c} \int_{\frac{a}{f(\epsilon)}}^{\infty} \frac{\mathrm{e}^{-t}}{bt + ac} \mathrm{d}t \right]$$

At last, use $t = v - \frac{ac}{b}$ with $\mathrm{d}t = \mathrm{d}v$

$$\lim_{\epsilon \to 0^+} \left[\frac{1}{c} \int_{a}^{\frac{a}{f(-\epsilon)}} \frac{\mathrm{e}^{-t}}{t} \mathrm{d}t - \frac{\mathrm{e}^{\frac{ac}{b}}}{c} \int_{a + \frac{ac}{b}}^{\frac{a}{f(-\epsilon)} + \frac{ac}{b}} \frac{\mathrm{e}^{-v}}{v} \mathrm{d}v + \right.$$
$$\left. \frac{1}{c} \int_{\frac{a}{f(\epsilon)}}^{\infty} \frac{\mathrm{e}^{-t}}{t} \mathrm{d}t - \frac{\mathrm{e}^{\frac{ac}{b}}}{c} \int_{\frac{a}{f(\epsilon)} + \frac{ac}{b}}^{\infty} \frac{\mathrm{e}^{-v}}{v} \mathrm{d}v \right]$$

This results can be simplified: convince for yourself with help of definition of E_1 B.20 that

$$\int_{f}^{g} \frac{\mathrm{e}^{-x}}{x} \mathrm{d}x = \mathrm{E}_1(f) - \mathrm{E}_1(g)$$

Apply this formula and get

$$\lim_{\epsilon \to 0^+} \left[\frac{1}{c}\mathrm{E}_1(a) - \frac{1}{c}\mathrm{E}_1\left(\frac{a}{f(-\epsilon)}\right) - \frac{\mathrm{e}^{\frac{ac}{b}}}{c}\mathrm{E}_1\left(a + \frac{ac}{b}\right) + \frac{\mathrm{e}^{\frac{ac}{b}}}{c}\mathrm{E}_1\left(\frac{a}{f(-\epsilon)} + \frac{ac}{b}\right) \right.$$
$$\left. + \frac{1}{c}\mathrm{E}_1\left(\frac{a}{f(\epsilon)}\right) - \frac{\mathrm{e}^{\frac{ac}{b}}}{c}\mathrm{E}_1\left(\frac{a}{f(\epsilon)} + \frac{ac}{b}\right) \right]$$

With the definition of $f(\pm\epsilon)$ and the properties of a, b, c rewrite to

$$\frac{1}{c}\mathrm{E}_1(a) - \frac{\mathrm{e}^{\frac{ac}{b}}}{c}\mathrm{E}_1\left(a+\frac{ac}{b}\right) + \lim_{\epsilon\to 0^+}\left[\frac{\mathrm{e}^{\frac{ac}{b}}}{c}\mathrm{E}_1\left(\frac{a}{f(-\epsilon)}+\frac{ac}{b}\right) - \frac{\mathrm{e}^{\frac{ac}{b}}}{c}\mathrm{E}_1\left(\frac{a}{f(\epsilon)}+\frac{ac}{b}\right)\right]$$

The last ϵ limit poses some problem as the arguments approach zero; the exponential integral contains a singularity at the origin. To solve, use a series expansion [3, Eq. 6.6.2] and take the asymptote for z approaching zero

$$\mathrm{E}_1(z) = -\gamma - \ln(z) - \sum_{n=1}^{\infty}\frac{(-1)^n z^n}{n!n}$$
$$\mathrm{E}_1(z) \approx -\gamma - \ln(z) \quad \text{for } z\to 0$$

Use this asymptote and $\ln a - \ln b = \ln\frac{a}{b}$ to write

$$\frac{1}{c}\mathrm{E}_1(a) - \frac{\mathrm{e}^{\frac{ac}{b}}}{c}\mathrm{E}_1\left(a+\frac{ac}{b}\right) - \frac{\mathrm{e}^{\frac{ac}{b}}}{c}\lim_{\epsilon\to 0^+}\ln\left[\frac{\frac{a}{\cos\left(\arccos\left(\frac{-b}{c}\right)-\epsilon\right)}+\frac{ac}{b}}{\frac{a}{\cos\left(\arccos\left(\frac{-b}{c}\right)+\epsilon\right)}+\frac{ac}{b}}\right] =$$
$$\frac{1}{c}\mathrm{E}_1(a) - \frac{\mathrm{e}^{\frac{ac}{b}}}{c}\mathrm{E}_1\left(a+\frac{ac}{b}\right) - \frac{\mathrm{e}^{\frac{ac}{b}}}{c}\ln[-1] =$$
$$\frac{1}{c}\mathrm{E}_1(a) - \frac{\mathrm{e}^{\frac{ac}{b}}}{c}\mathrm{E}_1\left(a+\frac{ac}{b}\right) - i\frac{\mathrm{e}^{\frac{ac}{b}}}{c}\pi$$

It is possible to change the sign of the imaginary term by un-careful algebraic manipulation, but this would be the incorrect principal value: a simple verification for this is checking the signs of the E_1's arguments and applying the following identity, see [3, Eq. 6.5.1]

$$\mathrm{E}_1(-x \pm i0) = -\mathrm{Ei}(x) \mp i\pi \quad x>0 \tag{B.22}$$

Where Ei is the exponential integral for non-complex arguments. Closer inspection of this identity and the fact that $a+\frac{ac}{b} < 0$ leads to a remarkable conclusion, namely, the cancellation of imaginary terms

$$\frac{1}{c}\mathrm{E}_1(a) - \frac{\mathrm{e}^{\frac{ac}{b}}}{c}\mathrm{E}_1\left(a+\frac{ac}{b}+i0\right) - i\frac{\mathrm{e}^{\frac{ac}{b}}}{c}\pi$$
$$\frac{1}{c}\mathrm{E}_1(a) - \frac{\mathrm{e}^{\frac{ac}{b}}}{c}\mathrm{Ei}\left(-a-\frac{ac}{b}\right) + i\frac{\mathrm{e}^{\frac{ac}{b}}}{c}\pi - i\frac{\mathrm{e}^{\frac{ac}{b}}}{c}\pi$$
$$\frac{1}{c}\mathrm{E}_1(a) - \frac{\mathrm{e}^{\frac{ac}{b}}}{c}\mathrm{Ei}\left(-a-\frac{ac}{b}\right)$$

This is the solution to the integral.

$$\int_0^{\frac{\pi}{2}}\frac{\mathrm{e}^{\frac{-a}{\cos(\theta)}}}{b+c\cos(\theta)}\sin(\theta)\,\mathrm{d}\theta = \frac{1}{c}\mathrm{E}_1(a) - \frac{\mathrm{e}^{\frac{ac}{b}}}{c}\mathrm{Ei}\left(-a-\frac{ac}{b}\right)$$
$$\{a,b\in\mathbb{R}\,|\,a,b>0\}$$
$$\{c\in\mathbb{R}\,|\,c<0\}$$
$$b+c\,\cos(\theta)=0 \quad \text{for } \theta\in\left(0,\frac{\pi}{2}\right) \tag{B.23}$$

B.7.3. The general identity

It is possible to combine both solution equations B.21, B.23 into one identity by considering only the real parts of the identities

$$\begin{aligned}
&\int_0^{\frac{\pi}{2}} \frac{\mathrm{e}^{\frac{-a}{\cos(\theta)}}}{b + c\cos(\theta)} \sin(\theta)\,\mathrm{d}\theta = \frac{1}{c}\left(\mathrm{E}_1(a) - \Re\left[\mathrm{e}^{\frac{ac}{b}}\,\mathrm{E}_1\left(a + \frac{ac}{b}\right)\right]\right) \\
&\{a, b \in \mathbb{R} \mid a, b > 0\} \\
&\{c \in \mathbb{R} \mid c \neq 0\} \\
&b + c\cos(\theta) \neq 0 \quad \text{if } \theta = 0 \vee \frac{\pi}{2}
\end{aligned} \tag{B.24}$$

Essentially, the pole must be inside the domain of integration and not on its bounds. The implications of a pole on the boundary domain have not been investigated. Only the real part of the solution is considered, which is denoted by the symbol $\Re$.

B.8. Appendix: lower hemisphere identity for the source-term integral

Many terms in the lower hemisphere source term integral of the FRTE can be solved after some manipulation. Computer algebra systems will find those readily. However, some terms do not have an obvious solution, so an integration identity for those is developed. First, the case without a singularity is considered. Second, the case with a pole is investigated. Third, the results are combined into a single identity.

B.8.1. Identity in absence of a denominator singularity

The problematic integrand of the source terms with cosines in the exponent, and in the absence of a pole, takes the form

$$\begin{aligned}
&\int_{\frac{\pi}{2}}^{\pi} \frac{\mathrm{e}^{\frac{a}{\cos(\theta)}}}{b + c\cos(\theta)} \sin(\theta)\,\mathrm{d}\theta \\
&\{a, b \in \mathbb{R} \mid a, b > 0\} \\
&\{c \in \mathbb{R} \mid c \neq 0\} \\
&b + c\cos(\theta) > 0
\end{aligned} \tag{B.25}$$

Use $t = \cos(\theta)$ and $\mathrm{d}t = -\sin(\theta)\,\mathrm{d}\theta$

$$\int_{-1}^{0} \frac{\mathrm{e}^{\frac{a}{t}}}{b + ct}\mathrm{d}t$$

Then apply $t = \frac{1}{u}$ and $\mathrm{d}t = -\frac{1}{u^2}\mathrm{d}u$

$$\int_{-\infty}^{-1} \frac{\mathrm{e}^{au}}{bu^2 + cu}\mathrm{d}u$$

Apply a partial fraction expansion

$$\frac{1}{c}\int_{-\infty}^{-1} \frac{\mathrm{e}^{au}}{u} - \frac{b\mathrm{e}^{au}}{bu + c}\mathrm{d}u$$

Now utilise $u = -\frac{t}{a}$, $\mathrm{d}u = -\frac{\mathrm{d}t}{a}$

$$\frac{1}{c}\int_a^\infty \frac{\mathrm{e}^{-t}}{t}\mathrm{d}t + \frac{b}{c}\int_a^\infty \frac{\mathrm{e}^{-t}}{bt+ac}\mathrm{d}t$$

At last, on the right term use $t = v - \frac{ac}{b}$ with $\mathrm{d}t = \mathrm{d}v$

$$\frac{1}{c}\int_a^\infty \frac{\mathrm{e}^{-t}}{t}\mathrm{d}t + \frac{\mathrm{e}^{\frac{ac}{b}}}{c}\int_{a+\frac{ac}{b}}^\infty \frac{\mathrm{e}^{-v}}{v}\mathrm{d}v$$

Finally, this gives the following identity

$$\begin{aligned}&\int_{\frac{\pi}{2}}^{\pi} \frac{\mathrm{e}^{\frac{a}{\cos(\theta)}}}{b + c\cos(\theta)}\sin(\theta)\,\mathrm{d}\theta = \frac{1}{c}\left(\mathrm{E}_1(a) + \mathrm{e}^{\frac{ac}{b}}\mathrm{E}_1\left(a+\frac{ac}{b}\right)\right)\\ &\{a, b \in \mathbb{R} \mid a, b > 0\}\\ &\{c \in \mathbb{R} \mid c \neq 0\}\\ &b + c\cos(\theta) > 0\end{aligned} \tag{B.26}$$

B.8.2. Identity in presence of a denominator singularity

Reconsider equation B.25, but now without the condition of positivity on the denominator

$$\begin{aligned}&\int_{\frac{\pi}{2}}^{\pi} \frac{\mathrm{e}^{\frac{a}{\cos(\theta)}}}{b + c\cos(\theta)}\sin(\theta)\,\mathrm{d}\theta\\ &\{a, b \in \mathbb{R} \mid a, b > 0\}\\ &\{c \in \mathbb{R} \mid c > 0\}\end{aligned}$$

now $b + c\cos(\theta)$ is somewhere positive and somewhere negative on the open domain of $\theta \in \frac{\pi}{2}, \pi$, thus $c > 0$ and $c > b$. This all leads to the existence of a pole in the denominator and the integral is improper, so solve it by assigning a Cauchy principal value; to start

$$\lim_{\epsilon\to 0^+}\left[\int_{\frac{\pi}{2}}^{\arccos\left(\frac{-b}{c}\right)-\epsilon} \frac{\mathrm{e}^{\frac{a}{\cos(\theta)}}}{b + c\cos(\theta)}\sin(\theta)\,\mathrm{d}\theta + \int_{\arccos\left(\frac{-b}{c}\right)+\epsilon}^{\pi} \frac{\mathrm{e}^{\frac{a}{\cos(\theta)}}}{b + c\cos(\theta)}\sin(\theta)\,\mathrm{d}\theta\right]$$

Apply u-substitution $t = \cos(\theta)$, $\mathrm{d}t = -\sin(\theta)\,\mathrm{d}\theta$ and introduce the following abbreviations $f(-\epsilon) = \cos\left(\arccos\left(\frac{-b}{c}\right) - \epsilon\right)$ and $f(\epsilon) = \cos\left(\arccos\left(\frac{-b}{c}\right) + \epsilon\right)$

$$\lim_{\epsilon\to 0^+}\left[\int_{f(-\epsilon)}^{0} \frac{\mathrm{e}^{\frac{a}{t}}}{b+ct}\mathrm{d}t + \int_{-1}^{f(\epsilon)} \frac{\mathrm{e}^{\frac{a}{t}}}{b+ct}\mathrm{d}t\right]$$

Now use $t = \frac{1}{u}$ and $\mathrm{d}t = -\frac{1}{u^2}\mathrm{d}u$ to see that

$$\lim_{\epsilon\to 0^+}\left[\int_{-\infty}^{\frac{1}{f(-\epsilon)}} \frac{\mathrm{e}^{au}}{u(bu+c)}\mathrm{d}u + \int_{\frac{1}{f(\epsilon)}}^{-1} \frac{\mathrm{e}^{au}}{u(bu+c)}\mathrm{d}u\right]$$

A partial fraction expansion is applied

$$\lim_{\epsilon\to 0^+}\left[\frac{1}{c}\int_{-\infty}^{\frac{1}{f(-\epsilon)}}\frac{\mathrm{e}^{au}}{u}-\frac{b\mathrm{e}^{au}}{bu+c}\mathrm{d}u+\frac{1}{c}\int_{\frac{1}{f(\epsilon)}}^{-1}\frac{\mathrm{e}^{au}}{u}-\frac{b\mathrm{e}^{au}}{bu+c}\mathrm{d}u\right]$$

Now use this substitution $u=\frac{-t}{a}$, $\mathrm{d}u=\frac{-\mathrm{d}t}{a}$

$$\lim_{\epsilon\to 0^+}\left[-\frac{1}{c}\int_{-\frac{a}{f(-\epsilon)}}^{\infty}\frac{\mathrm{e}^{-t}}{t}\mathrm{d}t-\frac{b}{c}\int_{-\frac{a}{f(-\epsilon)}}^{\infty}\frac{\mathrm{e}^{-t}}{ac-bt}\mathrm{d}t-\frac{1}{c}\int_{a}^{-\frac{a}{f(\epsilon)}}\frac{\mathrm{e}^{-t}}{t}\mathrm{d}t-\frac{b}{c}\int_{a}^{-\frac{a}{f(-\epsilon)}}\frac{\mathrm{e}^{-t}}{ac-bt}\mathrm{d}t\right]$$

At last, use $t=v+\frac{ac}{b}$ with $\mathrm{d}t=\mathrm{d}v$

$$\begin{aligned}\lim_{\epsilon\to 0^+}\Bigg[&-\frac{1}{c}\int_{-\frac{a}{f(-\epsilon)}}^{\infty}\frac{\mathrm{e}^{-t}}{t}\mathrm{d}t+\frac{\mathrm{e}^{-\frac{ac}{b}}}{c}\int_{-\frac{a}{f(-\epsilon)}-\frac{ac}{b}}^{\infty}\frac{\mathrm{e}^{-v}}{v}\mathrm{d}v+\\&-\frac{1}{c}\int_{a}^{-\frac{a}{f(\epsilon)}}\frac{\mathrm{e}^{-t}}{t}\mathrm{d}t+\frac{\mathrm{e}^{-\frac{ac}{b}}}{c}\int_{a-\frac{ac}{b}}^{-\frac{a}{f(\epsilon)}-\frac{ac}{b}}\frac{\mathrm{e}^{-v}}{v}\mathrm{d}v\Bigg]\end{aligned}$$

This results can be simplified: convince for yourself with help of definition of E_1 in equation B.20 that

$$\int_f^g\frac{\mathrm{e}^{-x}}{x}\mathrm{d}x=\mathrm{E}_1(f)-\mathrm{E}_1(g)$$

Apply this formula and get

$$\begin{aligned}\lim_{\epsilon\to 0^+}\Bigg[&-\frac{1}{c}\mathrm{E}_1(a)+\frac{1}{c}\mathrm{E}_1\left(-\frac{a}{f(-\epsilon)}\right)+\frac{\mathrm{e}^{-\frac{ac}{b}}}{c}\mathrm{E}_1\left(a-\frac{ac}{b}\right)+\frac{\mathrm{e}^{-\frac{ac}{b}}}{c}\mathrm{E}_1\left(-\frac{a}{f(-\epsilon)}-\frac{ac}{b}\right)\\&-\frac{1}{c}\mathrm{E}_1\left(-\frac{a}{f(\epsilon)}\right)-\frac{\mathrm{e}^{-\frac{ac}{b}}}{c}\mathrm{E}_1\left(-\frac{a}{f(\epsilon)}-\frac{ac}{b}\right)\Bigg]\end{aligned}$$

With the definition of $f(\pm\epsilon)$, the properties of a,b,c rewrite to

$$-\frac{1}{c}\mathrm{E}_1(a)+\frac{\mathrm{e}^{-\frac{ac}{b}}}{c}\mathrm{E}_1\left(a-\frac{ac}{b}\right)+\lim_{\epsilon\to 0^+}\left[\frac{\mathrm{e}^{-\frac{ac}{b}}}{c}\mathrm{E}_1\left(-\frac{a}{f(-\epsilon)}-\frac{ac}{b}\right)-\frac{\mathrm{e}^{-\frac{ac}{b}}}{c}\mathrm{E}_1\left(-\frac{a}{f(\epsilon)}-\frac{ac}{b}\right)\right]$$

The last ϵ limit poses some problem as the arguments approach zero; the exponential integral contains a singularity at the origin. To solve, use a series expansion [3, Eq. 6.6.2] and take the asymptote for z approaching zero

$$\begin{aligned}\mathrm{E}_1(z)&=-\gamma-\ln(z)-\sum_{n=1}^{\infty}\frac{(-1)^n z^n}{n!n}\\\mathrm{E}_1(z)&\approx-\gamma-\ln(z)\quad\text{for } z\to 0\end{aligned}$$

Use this asymptote and $\ln a-\ln b=\ln\frac{a}{b}$ to write

$$
\begin{aligned}
&-\frac{1}{c}\mathrm{E}_1(a)+\frac{\mathrm{e}^{-\frac{ac}{b}}}{c}\mathrm{E}_1\left(a-\frac{ac}{b}\right)+\frac{\mathrm{e}^{-\frac{ac}{b}}}{c}\lim_{\epsilon\to 0^+}\ln\left[\frac{-\frac{a}{\cos\left(\arccos\left(\frac{-b}{c}\right)-\epsilon\right)}-\frac{ac}{b}}{-\frac{a}{\cos\left(\arccos\left(\frac{-b}{c}\right)+\epsilon\right)}-\frac{ac}{b}}\right]=\\
&-\frac{1}{c}\mathrm{E}_1(a)+\frac{\mathrm{e}^{-\frac{ac}{b}}}{c}\mathrm{E}_1\left(a-\frac{ac}{b}\right)+\frac{\mathrm{e}^{-\frac{ac}{b}}}{c}\ln[-1]=\\
&-\frac{1}{c}\mathrm{E}_1(a)+\frac{\mathrm{e}^{-\frac{ac}{b}}}{c}\mathrm{E}_1\left(a-\frac{ac}{b}\right)+i\frac{\mathrm{e}^{-\frac{ac}{b}}}{c}\pi
\end{aligned}
$$

It is possible to change the sign of the imaginary term by un-careful algebraic manipulation, but this would be the incorrect principal value: a simple verification for this is checking the signs of the E_1's arguments and applying the following identity, see [3, Eq. 6.5.1]

$$\mathrm{E}_1(-x\pm i0)=-\mathrm{Ei}(x)\mp i\pi\quad x>0 \tag{B.27}$$

Where Ei is the exponential integral for non-complex arguments. Closer inspection of this identity and the fact that $a-\frac{ac}{b}<0$ leads to a remarkable conclusion, namely, the cancellation of imaginary terms

$$
\begin{aligned}
&-\frac{1}{c}\mathrm{E}_1(a)+\frac{\mathrm{e}^{-\frac{ac}{b}}}{c}\mathrm{E}_1\left(a-\frac{ac}{b}+i0\right)+i\frac{\mathrm{e}^{-\frac{ac}{b}}}{c}\pi\\
&-\frac{1}{c}\mathrm{E}_1(a)+\frac{\mathrm{e}^{-\frac{ac}{b}}}{c}\mathrm{Ei}\left(-a+\frac{ac}{b}\right)-i\frac{\mathrm{e}^{-\frac{ac}{b}}}{c}\pi+i\frac{\mathrm{e}^{-\frac{ac}{b}}}{c}\pi\\
&-\frac{1}{c}\mathrm{E}_1(a)+\frac{\mathrm{e}^{-\frac{ac}{b}}}{c}\mathrm{Ei}\left(-a+\frac{ac}{b}\right)
\end{aligned}
$$

This is the solution to the integral.

$$
\begin{aligned}
&\int_{\frac{\pi}{2}}^{\pi}\frac{\mathrm{e}^{\frac{a}{\cos(\theta)}}}{b+c\cos(\theta)}\sin(\theta)\,\mathrm{d}\theta=-\frac{1}{c}\mathrm{E}_1(a)+\frac{\mathrm{e}^{-\frac{ac}{b}}}{c}\mathrm{Ei}\left(-a+\frac{ac}{b}\right)\\
&\{a,b\in\mathbb{R}\,|\,a,b>0\}\\
&\{c\in\mathbb{R}\,|\,c>0\}\\
&b+c\,\cos(\theta)=0\quad\text{for}\;\theta\;\in\left(0,\frac{\pi}{2}\right)
\end{aligned}
\tag{B.28}
$$

B.8.3. The general identity

It is possible to combine both solution B.26 and B.28 into one identity

$$
\begin{aligned}
&\int_{\frac{\pi}{2}}^{\pi}\frac{\mathrm{e}^{\frac{a}{\cos(\theta)}}}{b+c\cos(\theta)}\sin(\theta)\,\mathrm{d}\theta=-\frac{1}{c}\left(\mathrm{E}_1(a)-\Re\left[\mathrm{e}^{-\frac{ac}{b}}\,\mathrm{E}_1\left(a-\frac{ac}{b}\right)\right]\right)\\
&\{a,b\in\mathbb{R}\,|\,a,b>0\}\\
&\{c\in\mathbb{R}\,|\,c\neq 0\}\\
&b+c\cos(\theta)\neq 0\quad\text{if}\;\theta=\frac{\pi}{2}\vee\pi
\end{aligned}
\tag{B.29}
$$

Essentially, the pole must be inside the domain of integration and not on its bounds. The implications of a pole on the boundary domain have not been investigated. Only the real part of the solution is considered, which is denoted by the symbol $\Re$.

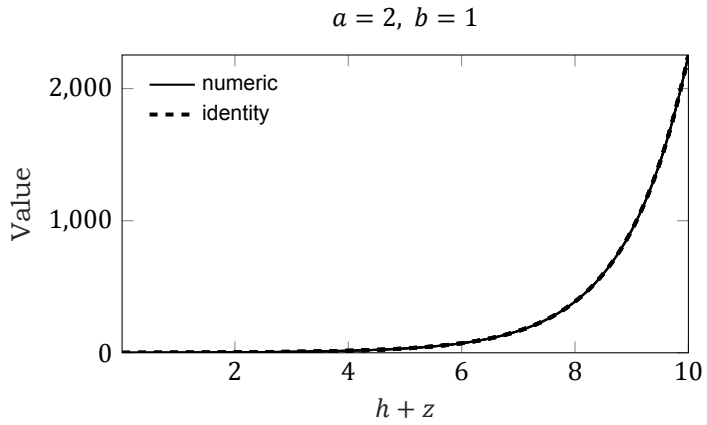

Figure B.3: Plot of the $h + z$ identity (eq: B.31) versus numeric integration. Blow-up occurs for large arguments $h + z$ if $a > b$.

B.9. Appendix: Indefinite integrals of $\mathrm{e}^{\pm ax}$ and $\mathrm{E}_1\,(bx)$ products

Applying the solution method of section 3.3.1 to the source term of B.12 gives rise to indefinite integrals of $\mathrm{e}^{\pm ax}$ and $\mathrm{E}_1\,(bx)$ products. Identities to integrate the terms need to be found: start with the following identities from [7]

$$\begin{aligned}\int \mathrm{e}^{-ax}\mathrm{E}_1\,(bx)\,\mathrm{d}x &= \frac{1}{a}\left[\mathrm{E}_1\{(a+b)\,x\} - \mathrm{e}^{-ax}\mathrm{E}_1\{bx\}\right] \\ \int \mathrm{e}^{ax}\mathrm{E}_1\,(bx)\,\mathrm{d}x &= -\frac{1}{a}\left[\mathrm{E}_1\{(b-a)\,x\} - \mathrm{e}^{ax}\mathrm{E}_1\{bx\}\right] \qquad b > a\end{aligned} \tag{B.30}$$

They consider a and b to be strictly positive. These identities form the inspiration for the new identity that can be proven by taking the derivative over z

$$\begin{aligned}\int \mathrm{e}^{\pm a(h+z)}\mathrm{E}_1\,(b\,(h+z))\,\mathrm{d}z &= \mp\frac{1}{a}\left[\mathrm{E}_1\{(b \mp a)\,(h+z)\} - \mathrm{e}^{\pm a(h+z)}\mathrm{E}_1\{b\,(h+z)\}\right] \qquad b > a \\ \int \mathrm{e}^{\pm a(h-z)}\mathrm{E}_1\,(b\,(h-z))\,\mathrm{d}z &= \pm\frac{1}{a}\left[\mathrm{E}_1\{(b \mp a)\,(h-z)\} - \mathrm{e}^{\pm a(h-z)}\mathrm{E}_1\{b\,(h-z)\}\right] \qquad b > a \\ \int \mathrm{e}^{\pm az}\mathrm{E}_1\,(bz)\,\mathrm{d}z &= \mp\frac{1}{a}\left[\mathrm{E}_1\{b \mp az\} - \mathrm{e}^{\pm az}\mathrm{E}_1\{bz\}\right] \qquad b > a\end{aligned} \tag{B.31}$$

All terms of the integrand can be written in this canonical form. Notice that in application, the condition $b > a$ is often violated, for example: $\alpha_\mathrm{e} > \alpha_\mathrm{d}$ were excitation light energy is absorbed more strongly than emitted fluorophore light. The interpretation is that the fluorophore radiance would blow-up if the medium were infinitely thick: the excitation light feeds the fluorophore radiance at a faster rate than it is removed. This is of-course physically impossible since the slab has a finite thickness of h. Therefore, the product of a, b and $h \pm z$ is very small for any real system. The indefinite integrals may not always exist, but for small, physically-real arguments they do. Figure B.3 depicts an example for this behaviour: a blow-up occurs, but only for large input arguments. The identity might not work in the mathematical sense, but it does so in a real-life, physical sense.

B.10. Appendix: Sanity checks for the FRTE solution

The derived solutions to the FRTE underwent some sanity checks by comparing model outputs to photon balances. In the coming discussion, assume $q = 0.5$ and that irradiance is going straight into the medium.

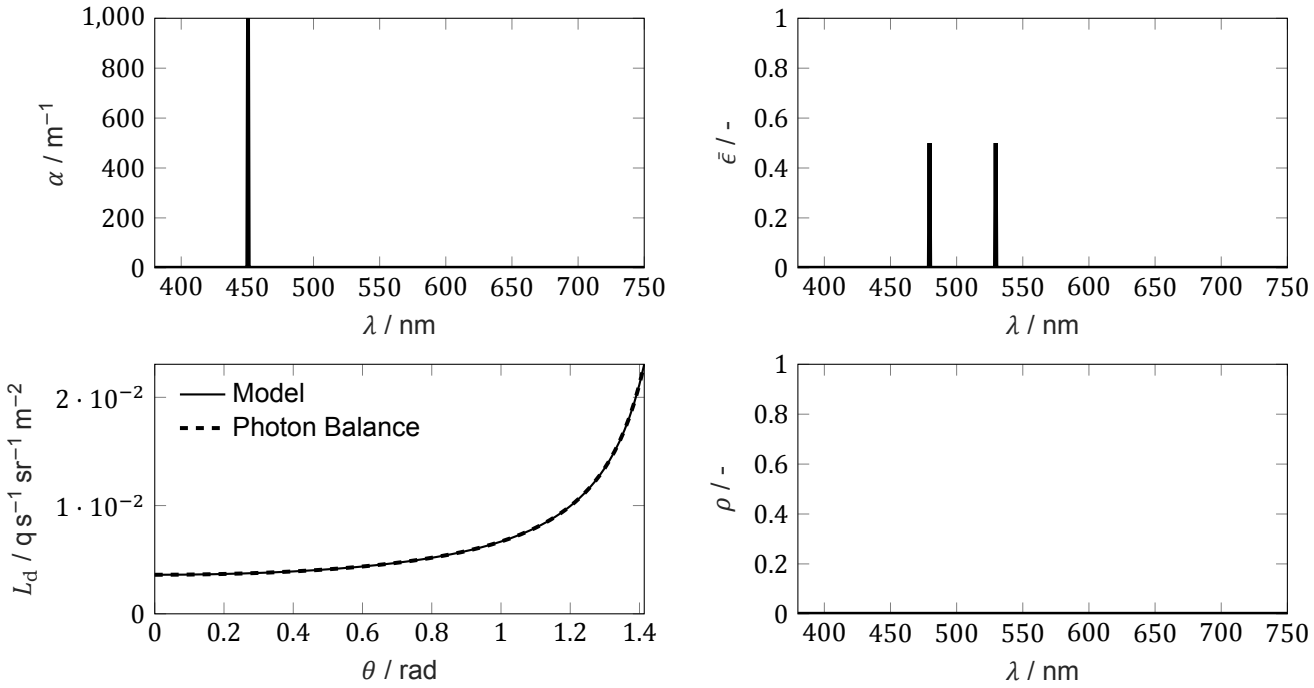

Figure B.4: Test case for L_d without reflectivity. Model evaluated at 530 nm, excited at 450 nm.

B.10.1. L_d, no mirror

Check the direct term, L_d, first. All data can be found in Figure B.4. Excitation happens at 450 nm and emission at 480 nm and 530 nm, of which we now consider the photon radiance balance at the latter one. By heuristics, the outgoing photon radiance at the top of the layer should be a fraction of the converted photon irradiance gathered along the path through the medium. The converted photons from the irradiance beam are not all put at the radiance wavelength of interest, so a efficiency, η, has to be introduced

$$L_\mathrm{d}(\theta, h, 530) = \eta \frac{\Delta E}{4\pi}$$

The 4π comes from the conversion of the photons in the parallel beam to the isotropic-over-solid-angle radiating process that is fluorescence. The change in irradiance along depth h follows from shuffling around Lambert Beer's law, but since the radiance is at angle with h, we need to scale by $\cos(\theta)$ to account for the longer photon-gathering path length that feeds the radiance L_d

$$L_\mathrm{d}(\theta, h, 530) = \eta \frac{E_0 \left(1 - \mathrm{e}^{-\alpha h}\right)}{4\pi \cos(\theta)}$$

E_0 is the irradiance at the top of the layer. From the normalized emission spectrum $\bar{\epsilon}$ and q, the efficiency can be defined

$$L_\mathrm{d}(\theta, h, 530) = q\bar{\epsilon} \frac{E_0 \left(1 - \mathrm{e}^{-\alpha h}\right)}{4\pi \cos(\theta)}$$

In the plots there is a perfect agreement between model and energy balance. For $\theta = 0.5\pi$, the cosine term goes to zero and both balance and model explode—not depicted in the plot.

B.10.2. L_d, mirror of half reflectivity

Let us now extend the previous model by adding a mirror. Add a spectrally constant reflectivity of $\rho(\lambda) = 0.5$—see Figure B.5

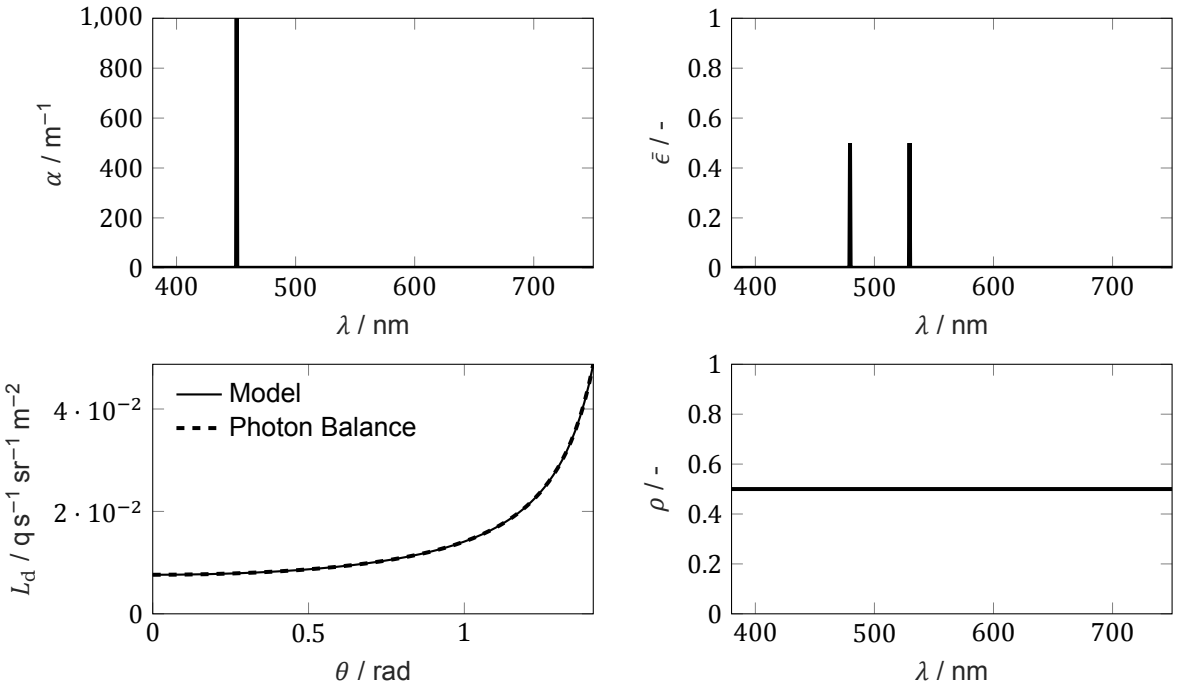

Figure B.5: Test case for L_d with half reflectivity. Model evaluated at 530 nm, excited at 450 nm.

$$L_\mathrm{d}(\theta, h, 530) = \eta_\rho \eta \frac{\Delta E}{4\pi}$$

The captured irradiance is modified by adding a reflected term. To do so, calculate the irradiance at the bottom of the layer, reflect it, and re-apply Lambert-Beer

$$L_\mathrm{d}(\theta, h, 530) = \eta_\rho \eta \frac{E_0 \left(1 - \mathrm{e}^{-\alpha h}\right) + \rho E_0 \mathrm{e}^{-\alpha h} \left(1 - \mathrm{e}^{-\alpha h}\right)}{4\pi \cos(\theta)}$$

η_ρ accounts for the reflected fluorescent radiance. Consider that fluorescence is an isotropic, radiative process, so the radiance hitting the mirror must be equal in size to the non-reflected one leaving the mirror. Therefore,

$$L_\mathrm{d}(\theta, h, 530) = (1 + \rho) q \bar{\epsilon} \frac{E_0 \left(1 - \mathrm{e}^{-\alpha h}\right) + \rho E_0 \mathrm{e}^{-\alpha h} \left(1 - \mathrm{e}^{-\alpha h}\right)}{4\pi \cos(\theta)}$$

Once again, model and photon balance are in agreement. This concludes the investigation of the L_d solution.

B.10.3. L_i no mirror, no-absorption limit case

L_i is much harder to check than L_d because of its dependence on fluorescent photon absorption, which is not as easily modelled as a parallel beam. The solution is to use an overlapping emission and absorption wavelength—see Figure B.6—where the latter is of such enormous magnitude that any emitted fluorescent photon is immediately re-absorbed to serve as a source for L_i. Therefore, the fluorescent photon source can be modelled like the parallel beam source. After the inclusion of the re-emission efficiency obtain

$$L_\mathrm{i}(\theta, h, 530) = q^2 \bar{\epsilon}^2 \frac{E_0 \left(1 - \mathrm{e}^{-\alpha h}\right)}{4\pi \cos(\theta)}$$

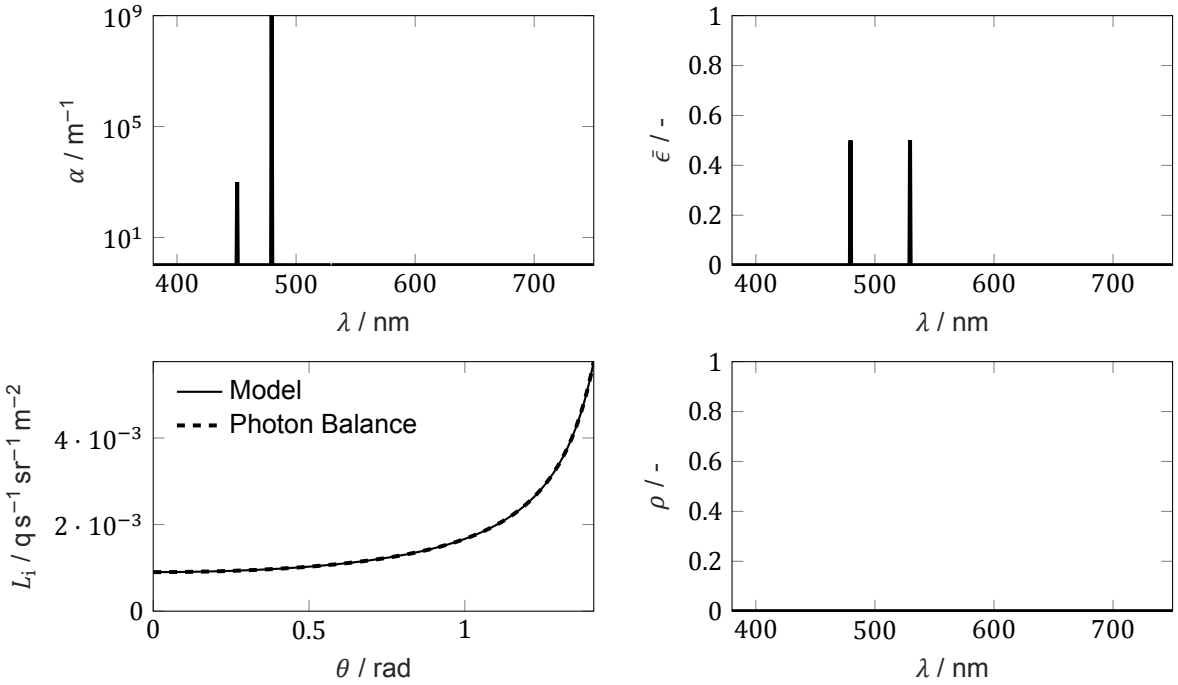

Figure B.6: Test case for L_i in the $\alpha_\mathrm{i} = 0$ limit without reflection. Model evaluated at 530 nm, excited at 450 nm.

We do not consider absorption of the second generation of fluorescent photon, so only the special limit case of $\alpha_\mathrm{i} = 0$ from section B.6 is tested.

B.10.4. L_i, no mirror, regular solution

Now verify the regular solution of L_i were absorption matters. Add a small absorption at 530 nm—Figure B.7. The model does indeed reduce the radiance as compared to the non-absorptive model, which increases with path length.

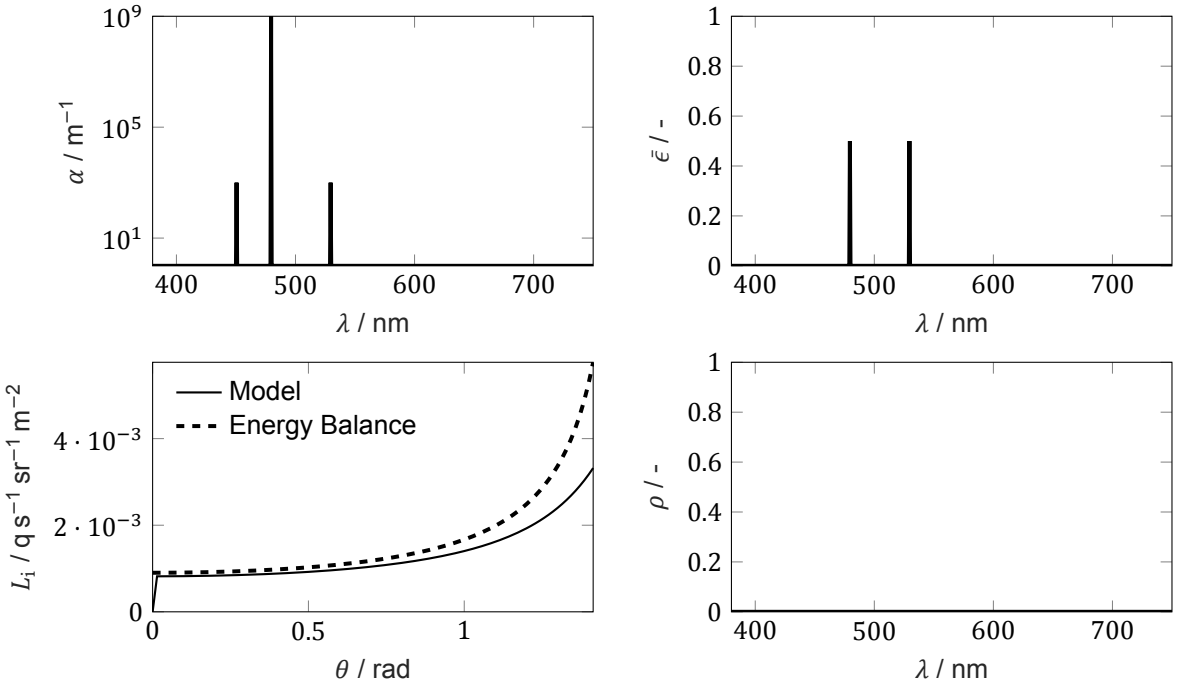

Figure B.7: Test case for L_i without reflection. Model evaluated at 530 nm, excited at 450 nm. Mild absorption added to test the regular solution. Zero value at $\theta = 0$ rad is due to $\alpha_\mathrm{i} = \alpha_\mathrm{e} \cos(\theta)$ throwing a NaN in Matlab which is set to zero by the script.

C

Appendix: Codes

C.1. Monte Carlo

main.m

```
clear all
close all
clc


%% Type of simulation
% Number of CPUs to use
parpool(4)
% of montecarlo simulations
repeat_no=1e9;

%Film heights m
% h = [20,500,900,2000]*1e-6;
h = [20,100,200,400,800,1200,1600,2000]*1e-6;
% h = [20,100,200,400]*1e-6;
h = [800,1200,1600,2000]*1e-6;

%angle of radiance with medium normal//z-axis radians
viewAngle = [0,1/8,1/4,3/8]*pi;

% Set reflection condition of domain's bottom: sets only angle; set
% spectral refl. coefficient "rho" in next section
reflType = 'lambertian';

%% Setup medium, dye- and spectral properties
% Import spectral data
filePathSpectra = ['C:\Users\plok\Google Drive\Uni\Master\Scriptie\',...
    'Matlab\SpectrumTool\Results\dataMasterSet.mat'];
data = open(filePathSpectra);


% Quantum Yield and molar concentration
phiFl = 0.85;
phiEy = 0.20;
cFl   = 0.5*0.25e-3;
cEy   = 0.5*0.25e-3;

% Absorption coeff. peaks [m^-1]

```

```
40 absCoPeakFl = 76.0e5*cFl;
41 %From: Spectrophotometric analysis of sodium fluorescein aqueous solutions.
42 %Determination of molar absorption coefficient
43
44 absCoPeakEy = 1.2*1.2*11.6e6*cEy;
45 %From: Data on eosin Y solutions for laser-induced
46 % fluorescence in water flows: it shows something close to or above 1e7
47 % Alternative: pH-Dependence of the absorption and fluorescent properties
48 % of fluorone dyes in aqueos solutions. Shows something close to to 2.2e7
49
50 % Wavelengths and LED wavelength
51 wvlArray = data.wavelengths;
52 wvlLED       = 450e-9;
53
54 % Spectrometer sensitivity
55 specSens = normalize(data.LampSpectrum, 'range')...
56      ./normalize(data.LampReferenceSpectrum,'range');
57 specSens = smoothdata(specSens,'gaussian',15);
58
59 % Absorption == Excitation spectrum of fluorescein and eosin
60 eyAbs = (normalize(data.eosinYAbsWater,'range'));
61 flAbs = (normalize(data.FluoresceinAbsWater,'range'));
62
63 % Eosin emissions. Filter, T, slightly bleeds into eyEm, cannot be removed
64 eyEm = data.eosinYEmWater./(specSens);
65 eyEm(isnan(eyEm)) = 0;
66 eyEm = normalize(eyEm, 'range');
67 eyEm = eyEm/sum(eyEm);
68
69 % Fluorescein Em. Filter, T, slightly bleeds into flEm, cannot be removed
70 flEm = data.FluoresceinEmWater./(specSens);
71 flEm(isnan(flEm)) = 0;
72 flEm = normalize(flEm, 'range');
73 flEm = flEm/sum(flEm);
74
75 % Shift spec: shifts, if applied, are from Fluorescence Properties of
76 % Twenty Fluorescein Derivatives:Lifetime, Quantum Yield, Absorption
77 % and Emission Spectra
78 eyEm = circshift(eyEm,-18); % -18 self-measured. slightly red-shifted due to thick layer.
79 eyAbs = circshift(eyAbs,0); % 2 according to literature; self-measured
80 flEm = circshift(flEm,1);   % 1 according to literature; have some doubts
81 flAbs = circshift(flAbs,0); % 2 according to literature; self-measured
82
83 % Spectral reflectivity
84 rho = data.MirrorCoating;
85 rho(:) = 1;
86
87 % Medium absorption
88 medAbs = zeros(size(flAbs));
89 absCoPeakMed = 0;
90
91 % Wavelength to index function.
92 wvl_c1 = length(wvlArray)-1;
93 wvl_c2 = wvlArray(1);
94 wvl_c3 = wvlArray(end)-wvlArray(1);
95 wvlId = @(wvl) round(1 +  wvl_c1 * (wvl-wvl_c2) / wvl_c3 );
96
97
98 %% Domain geometery and numerical aperture of sensor
99 % Sensor properties
100 r_s = 450e-6;               % Radius of sensor
```

```
numApAngle = deg2rad(10);   % Half-Angle of cone where-in rays are
                            % registered by the sensor
                            % viewAngle determines symmetry axis of the
                            % cone
lbAcceptAngle = cos(numApAngle);

%Optimize radius cylindrical domain m
Fmin = 0.01;    % Min view factor from infinitesimal cube to sensor disk -
                % Used to determine optimal domain size
cubeSz = h/10;  % Size of light-emitting cube

r_d = 3*0.5*optimizeR_d(r_s,Fmin,h,cubeSz); %Opt. function gives diameter.
                                            % R_f is rib-length, so multiply
                                            % by 0.5

% Rot. matrix projects ray from coord. syst. with z-axis along medium's
% surface normal to syst. with z-axis along optical axis of measurement
% system.
Rx = @(theta_x) [1, 0, 0;...
    0, cos(theta_x), -sin(theta_x);...
    0, sin(theta_x), cos(theta_x)];


%% Construct inverse CDF for wavelength selection
noOfSmpls = 10000;
[invCdf_EyWvl,invCdf_FlWvl] = findInvCdf_EmWvl(flEm,eyEm,wvlArray,noOfSmpls);

%% Storage for how many fluorophoric abs. events happen
maxAbsEvents = 20;
noAbsEvents = zeros(length(h),maxAbsEvents+1);

%% Simulation
% Store results
results = zeros(length(h),length(wvlArray),length(viewAngle));

no = length(h);
tic
ticBytes(gcp);

parfor jj =1:no
    % set database for photons: only ray terminating on sensor have a
    % non-zero energy.
    hTmp = h(jj);
    r_dTmp = r_d(jj);
    EatSensor = zeros(length(wvlArray),length(viewAngle));
    noAbsEvPerH = zeros(1,maxAbsEvents+1);
    for ii=1:repeat_no
        [wvlInd,energy,dx,fluorAbsCounter]=monte_carlo(hTmp,r_dTmp,...
            r_s,wvlLED,invCdf_EyWvl,invCdf_FlWvl,flAbs,eyAbs,medAbs,...
            absCoPeakFl,absCoPeakEy,absCoPeakMed,phiEy,phiFl,reflType,...
            noOfSmpls,wvlId,rho);

        if energy > 0

            for kk =1:length(viewAngle)
                % Project ray direction from coord. syst. with z-axis along
                % surface normal to z-axis normal with optical axis
                % Assume rotation symmetric optics == simple round
                % lenses...
                dxRot = Rx(viewAngle(kk))*dx.';
                if ( lbAcceptAngle <= -dxRot(3) ) %Direction cosine smaller
```

```
                    % than smallest direction cosine of acceptance angle
                    EatSensor(wvlInd,kk) = EatSensor(wvlInd,kk)+energy;
                end
            end


            if fluorAbsCounter <= maxAbsEvents
                noAbsEvPerH(fluorAbsCounter+1) = ...
                    noAbsEvPerH(fluorAbsCounter+1) + 1;
            end
        end

    end

    noAbsEvents(jj,:) = noAbsEvPerH;
    results(jj,:,:) = EatSensor;
    disp(['h = ',num2str(hTmp),' is done.'])
end
elapsedTime = toc
tocBytes(gcp);

%% Export data
medAbs = medAbs*absCoPeakMed;
descr = ['Rows correspond to h, columns to viewAngle. numSets is number',...
    'of samples Number of fluorophore abs. events index -1 is the true',...
    'number of events!'];
save([pwd,'/resultLambertianMC_ForGERIFPart2.mat'], 'viewAngle',...
    'h','descr','numApAngle','results','rho','medAbs','noAbsEvents',...
    'elapsedTime');

%% Shutdown after completion
system('shutdown -s')
```

optimizeR_d.m

```
function r_d = optimizeR_d(r_s,Fmin,h,meshSz)
% Obtain the optimal domain rib-length as defined by a cubic element's
% smallest view factor to the sensor such that the rays it releases make a
% significant contribution to the model output.
% INPUTS:
%   r_s:    radius of disk-shaped sensor. Scalar
%   Fmin:   cut-off view factor, cubic-elements with a smaller view factor
%   do not contribute meaningfully to the sensor. Scalar
%   h:    array of fluid heights
%   meshSz: array of cubic-element rib sizes. Same order as h.
% OUTPUTS:
%   r_d:    array of domain rib-lengths, same order as h


% Test variables
% r_s = 150e-6;
% Fmin = 0.01;
% h = [10,40,100,200,300,400,500,600]*10^(-6);
% meshSz = h/5;



%% Checks
assert(all(size(h) == size(meshSz)), 'h and meshSz array dimensions are not equal');
assert(all(0<h), 'h elements must all be positive');
assert(issorted(h),'h must be sorted');
assert((0<Fmin)&&(0.5>Fmin), 'Fmin must be between 0 and 0.5');
```

```
assert(0<r_s, 'r_s must be larger than 0');

%% Initiate optimization variables
%Optimization can give NaN for too large Fmin, script takes care of this
%case by max(r_dTmp); disabling prevents potential confusing errors
options = optimset('Display','off');
r_d = zeros(size(h));

%% Optimize for the domain's rib-length.
for ii = 1:length(r_d)

    % For every h there are multiple layers of cubic mesh-elements:
    % One of these layers has the smallest view factor and thus limits the
    % domain's size.
    hTmp = (1:h(ii)/meshSz(ii))*meshSz(ii);
    r_dTmp = zeros(size(hTmp));

    %Optimize half-rib length of domain for every possible cubic-mesh
    %element layer within h
    for jj=1:length(r_dTmp)
        r_dTmp(jj)=fzero(@(a)optDomSize(a,hTmp(jj),r_s,Fmin,...
            meshSz(ii)),5*r_s+hTmp(jj), options);
    end
    % 5*r_s +hTmp guarantees a very small start F, then F will monotically
    % increase to Fmin; if it exists.
    % Optmization function could have multiple minima: some directly under
    % the sensor disk, this initial condition prevents those from being
    % picked.


    %Pick largest half-rib length of all cubic mesh-element layers
    optR_f = max(r_dTmp);

    assert(r_s<optR_f,['Optimal r_d is smaller than r_s for h=',...
        num2str(h(ii)), ' check if Fmin is too large']);

    r_d(ii) = 2*optR_f; %Times two!!! opt. func. uses half rib-length r_d
end
end
```

optDomSize.m

```
function f = optDomSize(r_f,h_f,r_oAdj,Fmin, meshSz)
% Optimization function that determines if the view factor from an cubic
% element to the circular sensor is large enough by considering it as a
% root-finding problem where: f = Fcube - Fminimal = 0.
% Only considers the direct radiation from the top, sides and
% front of the cubic element. View factors derived from:
% New configuration factor between a circle, a sphere and a differential area
% at random positions.
% INPUTS:
% r_f: raw rib length of rectangular domain with square top
% h: fluid height
% r_oAdj: radius of sensor, adjusted to be multiple of mesh size
% Fmin: minimal view factor required
% OUTPUTS:
% f: difference between view factor and desired view factor
% NOTE r_f > r_oAdj and h > 0 and r_f >0 for sensible results

%Initiate usefull variables according to the paper's naming convention

x = 0;
```

```
y = h_f-meshSz*0.5;
z = 0.5*r_f-meshSz*0.5;
r = r_oAdj;

% View factors
Fside = (0.5/pi) * (atan((r+z)/y) + atan((r-z)/y)) +...
    (y/(4*pi*z)) * log( (r^2+y^2+z^2-2*r*z) / (r^2+y^2+z^2+2*r*z) );

Ffront = y*z / (2*(x^2+z^2))*....
    ( (r^2+x^2+y^2+z^2) / sqrt( (r^2+x^2+y^2+z^2)^2-4*r^2*(x^2+z^2) )-1 );

Ftop = 0.5*(1-(x^2+y^2+z^2-r^2) / sqrt((r^2+y^2+z^2)^2-4*r^2*(x^2+z^2)));

% Resulting view factor minus wanted view factor: --> is needed te create
% nonlinear, root-finding problem where a Newton scheme finds f = 0
% 1/6 for the six sides of the cube
f = (1/6)*(2*Fside+Ffront+Ftop)-Fmin;


end
```

findInvCdf_EmWvl.m

```
function [invCdf_EyWvl,invCdf_FlWvl] = findInvCdf_EmWvl(flEm,eyEm,wvlArray,noOfSmpls)
%Find the inverse cumulative distribution function from the emission
%spectra of Fluorescein and Eosin Y. Returns a look-up table.
% noOfSmpls needs to be >> length of wvlArray to prevent bias at the tails
% of the inv CDF.

flEm = normalize(flEm,'range');
eyEm = normalize(eyEm,'range');

pdfFl = flEm/sum(flEm); % Normalize spectra
pdfEy = eyEm/sum(eyEm);

% Remove 0 valued measurement artifacts right of the emission peak.
[~,pdfFl_max] = max(pdfFl);          % find peak
pdfFl_rhs = zeros(size(pdfFl));      % select indices right of the peak
pdfFl_rhs(pdfFl_max:end) = 1;
pdfFl(logical((pdfFl==0).*pdfFl_rhs)) = eps; % set 0's to machine precision

[~,pdfEy_max] = max(pdfEy);
pdfEy_rhs = zeros(size(pdfEy));
pdfEy_rhs(pdfEy_max:end) = 1;
pdfEy(logical((pdfEy==0).*pdfEy_rhs)) = eps;

% Find Cumulative Distribution Functions
cdfFl = cumtrapz(pdfFl);
cdfEy = cumtrapz(pdfEy);


% First select the indices where the CDF has one-to-one relation to the
% wavelengths
ind_Fl = find((0<cdfFl)); %Not smaller than 1 due to round-off errors
ind_Fl = [ind_Fl(1)-1,ind_Fl]; % Add the indices where F = 0 for last time;

ind_Ey = find((0<cdfEy));
ind_Ey = [ind_Ey(1)-1,ind_Ey];

% Pre-allocate inverted CDF
invCdf_FlWvl = zeros(1,noOfSmpls);
invCdf_EyWvl = zeros(1,noOfSmpls);
```

```

% Create a look-up table for inverted CDF
for ii = 0:1:(noOfSmpls-1)
    smplPoint = ii/(noOfSmpls-1); % Linear sampling of CDF between 0 and 1
    invCdf_FlWvl(ii+1) = interp1(cdfFl(ind_Fl).',wvlArray(ind_Fl).',...
        smplPoint,'linear',wvlArray(ind_Fl(end)));
    invCdf_EyWvl(ii+1) = interp1(cdfEy(ind_Ey).',wvlArray(ind_Ey).',...
        smplPoint,'linear',wvlArray(ind_Ey(end)));
end


end
```

monte_carlo.m

```
function [wvlInd,energy,dx,fluorAbsCounter]=monte_carlo(h,r_d,r_s,...
    wvlLED,invCdf_EyWvl,invCdf_FlWvl,flAbs,eyAbs,medAbs,absCoPeakFl,...
    absCoPeakEy,absCoPeakMed,phi_ey,phi_fl,reflType,noOfSmpls,wvlId,rho)


% Release LED rays by Uniform sampling of top of cylindrical domain
theta = rand*2*pi;
radius = r_d*sqrt(rand);
x0 = [radius*cos(theta),radius*sin(theta),0];
% Direct of ray
dx = [0,0,1];

% Wavelength
wvl = wvlLED;
wvlInd = wvlId(wvlLED);
% First path-length travelled
L = findAbsL(flAbs,eyAbs,medAbs,absCoPeakFl,absCoPeakEy,absCoPeakMed,wvlInd);
alive = true;
energy = 1;
fluorAbsCounter = 0;

while alive


    x = x0 +dx*L;

    if (x(3)-h) > 0 %Hit lower boundary

        [x0,dx,L,aliveTmp] = reflection(x0,dx,L,h,reflType);
        if aliveTmp == 0 %Prevents not creating output for monte carlo func.
            energy = 0;
            alive = false;
        end
        energy = energy*rho(wvlInd);
    elseif x(3)<0 % Left domain through top boundary

        if diskIntersect(x0,dx,r_s) % Hit detector
            alive = 0;
        else % Did not hit detector
            energy = 0;
            alive = false;
        end

    else % Ray still inside domain

        % Ray can now ge absorbed forever or re-emitted
```

```
47          % First, whicht dye does the actual absorbing?
48          absByDye = absDyeSelect(flAbs,eyAbs,medAbs,absCoPeakFl,...
49              absCoPeakEy,absCoPeakMed,wvlInd);
50
51          if  absByDye == 2
52              phi = phi_ey;
53              invCdf_Wvl = invCdf_EyWvl;
54              fluorAbsCounter = fluorAbsCounter+1;
55          elseif absByDye == 1
56              phi = phi_fl;
57              invCdf_Wvl = invCdf_FlWvl;
58              fluorAbsCounter = fluorAbsCounter+1;
59          else % abs by medium; stop simulation
60              energy = 0;
61              alive = false;
62              break
63          end
64
65          if rand<=phi % Re-Emissions at different wavelength
66              wvl_new = invCdf_Wvl(1+floor(rand*(noOfSmpls-1)));
67              energy = energy*wvl/wvl_new;
68              wvl = wvl_new;
69              wvlInd = wvlId(wvl);
70              L = findAbsL(flAbs,eyAbs,medAbs,absCoPeakFl,...
71                  absCoPeakEy,absCoPeakMed,wvlInd);
72              x0 = x;
73              dx = randomAngles();
74          else % Absorption/heat-generation
75              energy = 0;
76              alive = false;
77          end
78
79      end
80
81
82  end
```

findAbsL.m

```
1   function [absL] = findAbsL(flAbs,eyAbs,medAbs,absCoPeakFl,absCoPeakEy,...
2       absCoPeakMed,wvlInd)
3   % Uses the absorption spectra of Fluorescein and Eosin Y to create a
4   % realization for the path-length where a ray is terminated. The inverse
5   % cumulative distribution functions derived from Beer-Lambert's law
6
7   absL = -log(-rand+1) / (eyAbs(wvlInd)*absCoPeakEy+...
8       absCoPeakFl*flAbs(wvlInd)+absCoPeakMed*medAbs(wvlInd)) ;
9
10  end
```

reflection.m

```
1   function [x0_new,dx,L_remaining,alive] = reflection(x0,dx,L,h,reflType)
2   % Reflects the ray or absorbs it.
3   % Updates direction cosines, position, and path-length of the ray
4
5
6   L_traveled = (h-x0(3))/dx(3);
7   L_remaining = L-L_traveled;
8   x0_new = x0+dx*L_traveled; %Position on lower boundary
9
10  switch reflType
```

```
    case 'absorption'
        dx = dx;
        alive = 0;
    case 'lambertian'
        alive = 1;
        dx = diffuseRefl(); % Uses uniform sampling on a hemispher
    case 'specular'
        alive = 1;
        dx(3) = -dx(3);
    otherwise
        warning('Unknown reflection condition')
end
```

diffuseRefl.m

```
function [ dx ] = diffuseRefl()
%% Samples direction cosines
% Cartesian coordinate system
% Uniform distribution on a hemisphere: inverted z-axis
% From: Monte Carlo Technique for the Determination of Thermal Radiation
% Shape Factors

    theta = asin(sqrt(rand()));
    phi = 2.0*pi*rand();
    dx(1) = sin(theta)*cos(phi);
    dx(2) = sin(theta)*sin(phi);
%     dx(3) = cos(theta); % Regular solution
    dx(3) = -cos(theta);  % Coord. system is up-side down
end
```

diskIntersect.m

```
function [cond] = diskIntersect(x0,dx,r_s)
% Checks if a ray can pass through a disk in the xy-plane centered at
% (0,0,0). Method assumes a starting position where x0(3)>0.
t = -x0(3)/dx(3);

if x0(3)<0
    warning('Ray started outside of the fluorescent medium')
end

if t < 0
    cond = false;
    % Time is reversed in this case...
else
    cond = (x0(1)+dx(1)*t)^2 +(x0(2)+dx(2)*t)^2 - r_s^2 <=0;
end


end
```

absDyeSelect.m

```
function dyeNo = absDyeSelect(flAbs,eyAbs,medAbs,absCoPeakFl,...
            absCoPeakEy,absCoPeakMed,wvlInd)
% Returns the number of the dye responsible for photon absorption, or the
% if the absorption is done by the medium

norm = flAbs(wvlInd)*absCoPeakFl+eyAbs(wvlInd)*absCoPeakEy...
    +medAbs(wvlInd)*absCoPeakMed;
p1 = flAbs(wvlInd)*absCoPeakFl / norm;
p2 = eyAbs(wvlInd)*absCoPeakEy / norm + p1;
```

```

absEvent = rand;
if p1 > absEvent
    dyeNo=1;
elseif p2 > absEvent
    dyeNo=2;
else
    dyeNo=3;
end

end
```

randomAngles.m

```
function [ dx ] = randomAngles()
%% Samples direction cosines
% Cartesian coordinate system
% Uniform distribution on unit-sphere
    cosTheta = 1.0 - 2.0*rand;
    sinTheta = sqrt(1.0 - cosTheta*cosTheta);
    phi = 2.0*pi*rand();
    cosPhi = cos(phi);
    if (phi < pi)
        sinPhi = sqrt(1.0 - cosPhi*cosPhi);
    else
        sinPhi = -sqrt(1.0 - cosPhi*cosPhi);
    end
    dx(1) = sinTheta*cosPhi;
    dx(2) = sinTheta*sinPhi;
    dx(3) = cosTheta;
end
```

C.2. Derivation Analytic Solution

AnalyticModelSpecular.mlx

```
%% Solve the fluorescent radiative transfer equation for a plane-parallel
%% medium lying on a mirror
%   ^z  ^           ^----surface of medium
%   |mu/            |
%   |~/             | h
%   |/_____>x       v____mirror
%
%
%   mu = cos(theta): the direction cosine with the z-axis


clear all
clc

% Setup variables
syms a_e a_es a_d a_i a_ds h E_0 theta theta_e q_d q_i rho_e rho_d rho_i z Z
symlist = [a_e a_es a_d a_i a_ds h E_0 theta q_d q_i rho_e rho_d rho_i];

% Help Matlab by applying assumptions: not strictly true: see paper for
% the real assumptions
assume([a_e a_es a_d a_i a_ds h E_0 theta theta_e q_d q_i rho_e rho_d...
    rho_i z Z], {'real', 'positive'})
assumeAlso(theta >=0 & theta <=pi);
assumeAlso(h>z);
assumeAlso((a_d)>(a_e))

```

```
%% Define the excitation irradiation
% Is a collimated beam
% Theta_e is inside the layer! Not angle at which the layer is initially
% hit --> remember Snell's law
syms E(z)    % Irradiance of light source

% Not truly dependent on theta, but Matlab needs matching input arguments
% when combining functions
E_E(z,theta) = E_0*exp(-a_e*(h-z)) + rho_e*E_0*exp(-a_e*(h+z))



%% Solve for direct fluorescent radiance
% The part that is directly caused by the collimated beam of excitation light
% incident on the medium.

% Definitions
syms L_d(z,theta)                  % Direct radiance
dL_d = diff(L_d,z);                % Derivative
syms L_d_g L_d_p_down(z,theta)     % Integrating factor method parts
syms L_d_p_up(z,theta) mu_d Cd_d Cd_u


% Differential equation
eqnL_d = cos(theta)*dL_d == -(a_d)*L_d+multByTerm(E_E,q_d*a_es/(4*pi));

% Find general solution first
% Integrating factor
mu_d(z,theta)= exp(a_d*z/cos(theta)) ;
% Parameter from int. fact. method
Q_d(z,theta) = multByTerm(E_E,q_d*a_es/(4*pi*cos(theta)));
% General solution
L_d_g = sum(simplify(int(symCell2arr(children(Q_d))*mu_d,z)/mu_d));

% Find particular solution in downward direction
Cd_d = multByTerm(L_d_g(h,theta),-mu_d(h,theta));    % Int constant down
L_d_p_down = L_d_g + multByTerm(Cd_d,  1/mu_d);      % Particular solution

% Find particular solution in upward direction
Cd_u = multByTerm( subs(subs(L_d_p_down,cos(theta),-cos(theta)),z,0),...
    rho_d) - subs(L_d_g,z,0);  % Int constant up
L_d_p_up =  L_d_g + multByTerm(Cd_u,  1/mu_d)

% Check solution by subsitution in the differential equation
% simplify(subs(lhs(eqnL_d),L_d,L_d_p_up)-subs(rhs(eqnL_d),L_d,L_d_p_up))


%% Solve for the indirect fluorescent radiance: definitions
% Initialize
syms L_i(z,theta)                  % Indirect radiance
dL_i = diff(L_i,z);                % Derivative
syms L_i_g L_i_p_down(z,theta)     % Integrating factor method parts
syms L_i_p_up(z,theta) mu_i Ci_d Ci_u
syms S_t     S                     % Source term

% Differential equation
eqnL_i = cos(theta)*dL_i == -(a_i)*L_i+S_t;

%% Solve for the indirect fluorescent radiance: source term

%% DOWNWARD TERMS: solve differently for exp. term containing cos, and without
```

```
88  tmpIntegrands = symCell2arr(children(L_d_p_down));
89
90  % Note multiplication: from solid angle integral
91  tmpNoCos = 1/2*int(tmpIntegrands(3)*sin(theta),theta,pi/2,pi) +...
92      children(1/2*int(tmpIntegrands(1)*sin(theta),theta,pi/2,pi),2);
93  tmpWithCos = [sourceTermInt(tmpIntegrands(2),theta,"down","noCombine"),...
94      sourceTermInt(tmpIntegrands(4),theta,"down","noCombine")];
95  S_down = multByTerm(sum(tmpNoCos) + sum(tmpWithCos), q_i*a_ds);
96
97  %% UPWARD TERMS: solve differently for exp. term containing cos, without
98  tmpIntegrands = symCell2arr(children(L_d_p_up));
99
100 % Note on multiplication with constant: from solid angle integral
101 % Select Cauchy's Principal Value solution
102 tmpNoCos = 1/2*int(tmpIntegrands(1)*sin(theta),theta,0,pi/2) +...
103     children(1/2*int(tmpIntegrands(3)*sin(theta),theta,0,pi/2),2);
104
105
106
107 tmpWithCos = tmpIntegrands([2,4:8]);
108 for ii = 1:length(tmpWithCos)
109     tmpWithCos(ii) =sourceTermInt(tmpWithCos(ii),theta,"up","noCombine");
110 end
111
112 S_up = multByTerm(sum(tmpNoCos) + sum(tmpWithCos), q_i*a_ds);
113
114 %% FINAL RESULT
115 S = S_up + S_down;
116
117 %% Solve for the indirect fluorescent radiance: solutions
118
119 % Find general solution first: start with integrating factor
120 mu_i = exp(a_i*z/cos(theta));
121
122 % Split-up in log parts and the more difficult E1 parts.
123 tmpIntegrands = symCell2arr(children(S))*mu_i/cos(theta);
124 tmpLog = tmpIntegrands(has(tmpIntegrands,'log'));
125 tmpNoLog = tmpIntegrands(~has(tmpIntegrands,'log'));
126
127 for ii = 1:length(tmpLog)   % All log containing integrands
128     tmpLog(ii) = combine(collect(int(tmpLog(ii),z),{'E_0','a_ds','a_es',...
129         'q_d','q_i', 'rho_e'})/mu_i,'exp');
130 end
131
132
133 warning('off','symbolic:solve:SolutionsDependOnConditions');
134 for ii = 1:length(tmpNoLog) % All other terms
135     tmpNoLog(ii) = intEiExp2(tmpNoLog(ii),z,h)/mu_i;
136 end
137 warning('on','symbolic:solve:SolutionsDependOnConditions');
138
139 %% General solution
140
141
142 L_i_g = sum(tmpLog) + sum(tmpNoLog);
143
144 L_i_g = limit(L_i_g,a_i,0,'right')
145 mu_i = 1;
146
147 % Find particular solution in downward direction
148 Ci_d = - multByTerm(limit(L_i_g,z,h,"left"),subs(mu_i,z,h));
```

```
149 L_i_p_down = L_i_g + multByTerm(Ci_d,1/mu_i);
150
151 % Find particular solution in upward direction
152 Ci_u = multByTerm( limit(subs(L_i_p_down,cos(theta),-cos(theta)),z,0, ...
153     'right'),rho_i) - limit(L_i_g,z,0,'right'); % Int constant up
154 L_i_p_up =  L_i_g + multByTerm(Ci_u,  1/mu_i);
155
156 % Check solution by subsitution in the differential equation
157 simplify(subs(lhs(eqnL_i),L_i,L_i_p_up)-subs(rhs(eqnL_i),[L_i,S_t],...
158     [L_i_p_up,S]))
159
160 %% Limit cases for z  = h; limit case for zero indirect absorption
161 % The radiance at the top of the layer
162 L_i_p_up_at_h = limit(L_i_p_up,z,h,"left");
163 L_d_p_up_at_h = limit(L_d_p_up,z,h,"left");
164 L_i_p_up_at_h_0a_i = limit(L_i_p_up_at_h,a_i,0,'right');
165
166 %% Some extra limits for the general solution
167 % L_i_g_h = limit(L_i_g,z,h,"left")
168 % L_i_g_0 = limit(L_i_g,z,0,"right")
169
170 %% Create numeric matlab functions
171 syms nu % Prevent repeated calculation of cos(theta) by pre-calculating it
172
173 matlabFunction(subs(L_d_p_up_at_h,cos(theta),nu),'File','L_directSpec',...
174     'Vars',{theta,nu,h,a_e a_es a_d E_0 q_d rho_e rho_d},'Optimize',true);
175 matlabFunction(subs(L_i_p_up_at_h,cos(theta),nu),'File','L_indirectSpec',...
176     'Vars',{theta,nu,h,a_e a_es a_d a_i a_ds E_0 q_d q_i rho_e rho_d...
177     rho_i},'Optimize',true);
178 matlabFunction(subs(L_i_p_up_at_h_0a_i,cos(theta),nu),'File',...
179     'L_indirectSpecNo_a_i','Vars',{theta,nu,h,a_e a_es a_d a_ds E_0 q_d...
180     q_i rho_e rho_d rho_i},'Optimize',true);
181
182 %% This part was used to create formulas that are easy to parse to LaTeX
183 % L_i = limit(L_i_gensol_theta,z,h,'left')
184 % L_iPrt = symCell2arr(children(L_i_g_h))
185 % E1prt = sum(L_iPrt(has(L_iPrt,'ei')))
186 % E1prt = collect(E1prt,'ei')
187 % E1prtChild = symCell2arr(children(E1prt))
188 % Logprt = sum(L_iPrt(~has(L_iPrt,'ei')))
189 % Logprt = collect(Logprt,'log')
190 % symCell2arr(children(Logprt))
191 % mu = exp((a_i)*z/cos(theta))
192 % (simplify(subs(E1prtChild(8),[E_0,a_ds,a_es,q_i,q_d,],[1,1,1,1,1])))
```

multByTerm.m

```
1 function g = multByTerm(f,c)
2 % Simplifies the multiplication of a series by a constant term:
3 % Multiplies each term individually instead of the entire series
4 % Keeps the equation simple to process and re-arrange.
5  g = sum(symCell2arr(children(f))*c);
6 end
```

symCell2arr.m

```
1 function [arr] = symCell2arr(cell)
2 %The children function returns a cell-array, yet sym. toolbox.
3 %functions expect arrays...
4 % Written by Pieter Lok: 28-12-2021
5
6 arr = sym(zeros(size(cell)));
```

```
7
8  for ii=1:length(cell)
9      arr(ii)=cell{ii};
10 end
11
12 end
```

getExpPow.m

```
1  function pow = getExpPow(exp)
2  % Obtain the power of an exponential function
3          pow = simplify(log(findSymType(exp,'exp')),...
4          'IgnoreAnalyticConstraints',true);
5  end
```

sourceTermInt.m

```
1  function Sint = sourceTermInt(s,theta,hemisphere, outputForm)
2  % Symbolically evaluate the source term integrals that include cosine
3  % terms in the exponential-function argument
4  % s      the integrand: symbolic type
5  % hemisphere: "up" or "down", the part of the hemisphere to integrate over;
6  %        defined by x such that up is C [0,pi/2] and down is C [pi/2, pi]
7  % S      the integral of s: symbolic type
8  % outputForm: if "combine", integrand s will be output with a share
9  % denominator
10
11 %% Define integration variable and it's int. boundaries
12 syms x0 x1 x u v w
13 x = theta;
14 if hemisphere == "up"
15     x0 = sym(0); x1 = sym(pi/2);
16 elseif hemisphere == "down"
17         x0 = sym(pi/2); x1 = sym(pi);
18 else
19     warning('Select a proper hemisphere to integrate over: "up" or "down"')
20 end
21
22 %% simplify integrand into constant and relevant parts:
23 % assumes all source have denominator of the following form 4*pi*( f(cos(x)) )
24 s = expand(s); %Expand exponentials
25 expTerms = findSymType(s,'exp');
26 cosArgIdx = has(expTerms,'cos');
27
28 sExpNonCos = subs(s, expTerms, ones(size(expTerms)));
29 sExpNonCos = sExpNonCos*combine(prod(expTerms(~cosArgIdx)),'exp');
30 [num,den] = numden(sExpNonCos);
31
32 % part of integrand outside the integral: 2pi
33 % from integration over the azimuthal angle
34 sConst = num/2;
35 % integrand not moved outside of integral
36 sInt = simplify(combine(prod(expTerms(cosArgIdx)),'exp'))/(simplify(den));
37
38
39 %% Solve the integrand
40 Sint = int(sInt*sin(x),x,x0,x1, 'Hold', true);
41 Sint = clVWrapper(changeIntegrationVariable(Sint,cos(x),v));
42 Sint = clVWrapper(changeIntegrationVariable(Sint,v,1/u));
43 % Partial fractions of the integrand and convert to sym array
44 SintFrac = symCell2arr( children(partfrac(children(Sint,1),u)) );
45 x0 = children(Sint,3); x1 = children(Sint,4);
```

```
46
47
48  Sint_1 = int(SintFrac(1),u,x0,x1,'Hold',true);
49  Sint_2 = int(SintFrac(2),u,x0,x1,'Hold',true);
50
51  % Solve first fraction
52  Sint_1Pow = getExpPow(SintFrac(1));
53  Sint_1 = clVWrapper(changeIntegrationVariable(Sint_1,u,-w*u/Sint_1Pow));
54
55
56  signPow = not(has(expand(Sint_1),-w));
57
58  % Create a proper expintegral function: int(exp(-v)/v) _x0 ^x1
59  if signPow == 1
60      Sint_1 = clVWrapper(changeIntegrationVariable(Sint_1,w,-v));
61  end
62
63
64  Sint_1 = release(Sint_1);
65
66  % Solve second fraction
67  Sint_2Pow = getExpPow(SintFrac(2));
68  Sint_2 = clVWrapper(changeIntegrationVariable(Sint_2,u,-w*u/Sint_2Pow));
69  [~,den] = numden(children(Sint_2,1));
70  den = symCell2arr(children(den));
71  eq = v == den(has(den,w));
72  wIsEqToVFunc = solve(eq,w);
73  Sint_2 = clVWrapper(changeIntegrationVariable(Sint_2,w,wIsEqToVFunc));
74
75  signPow = not(has(expand(Sint_2),-v));
76
77  % Create a proper expintegral function: int(exp(-v)/v) _x0 ^x1
78  if signPow == 1
79      Sint_2 = clVWrapper(changeIntegrationVariable(Sint_2,v,-w));
80  end
81
82  Sint_2 = release(Sint_2);
83
84
85  %% Clean-up and combine parts of the integral
86  % In some edge-cases, MATLAB does not recognize that assumptions on
87  % symbolic variables are met, and as such creates a piecewise function.
88  % Select the right expint containing term
89  if hasSymType(Sint_1, 'piecewise')
90      tmp = symCell2arr(children(Sint_1));
91      Sint_1 = tmp(hasSymType(tmp, 'ei'));
92  end
93
94  % In some edge-cases, MATLAB does not recognize that assumptions on
95  % symbolic variables are met, and as such creates a piecewise function.
96  % Select the right expint containing term
97  if hasSymType(Sint_2, 'piecewise')
98      tmp = symCell2arr(children(Sint_2));
99      Sint_2 = tmp(hasSymType(tmp, 'ei'));
100 end
101
102
103
104 if outputForm == "combine"
105     Sint =partfrac(sConst*(simplify(Sint_1)+simplify(Sint_2)));
106 else
```

```
107     Sint = sConst*simplify(Sint_1)+sConst*simplify(Sint_2);
108 end
109
110
111 end
```

clVWrapper.m

```
1  function g = clVWrapper(f)
2  % The changeIntegrationVariable function can return integrals where the
3  % lower limit of intergration is larger than the upper limit. This poses a
4  % problem by repeated calls to the same function, as it expects the reverse
5  % of integration limits.
6  ar = children(f); % arguments of the unevaluated integral
7
8
9  % Check if lower int. limit >> upper int. limit
10 % If so, swap, as Mupad Engine assumes the reverse
11 if ar{3} > ar{4}
12     g = int(-ar{1},ar{2},ar{4},ar{3},'hold',true);
13 else
14     g = int(ar{1},ar{2},ar{3},ar{4},'hold',true);
15 end
16
17 if ar{3} == inf
18     g = int(-ar{1},ar{2},ar{4},ar{3},'hold',true);
19 end
20
21 if ar{4} == -inf
22     g = int(-ar{1},ar{2},ar{4},ar{3},'hold',true);
23 end
24 end
```

intEiExp2.m

```
1  function [F] = intEiExp2(f,x,c)
2  %Evaluate indefinite integrals with integrands of the following form:
3  % f = exp(+-au)expint(bu) with a and b real and positive:
4  % Use identities from Geller and Ng (1969)
5  % Assumes that exp. int. arguments can be factored such that
6  % expint(d*(e*c-/+x)) with d,e constants and c is a variable that
7  % linearly translate x.
8
9
10 syms u
11
12 %Split f up in constants, and exponents and exponential integrals
13 fChild = symCell2arr(children(f));
14 fExpEiPart = prod(fChild(has(fChild,'exp')))*fChild(has(fChild,'ei'));
15 fConstPart = prod(fChild(~has(fChild,'exp')&~has(fChild,'ei')));
16
17
18
19 % Split exp. and exp. int. part further
20 expTerm = findSymType(fExpEiPart,'exp');
21 eiTerm = findSymType(fExpEiPart,'ei');
22
23 % Sometimes,negative sign of constant part gets put into the exp. and
24 % exp int. containing parts. It will then be lost after the call to
25 % function "intEiExpIdentity". Add it back after this function-call.
26 sign = subs(fExpEiPart,[expTerm,eiTerm],[ones(size(expTerm)),1]);
27
```

```
%Simplify ei arguments to this form d*(e*c-/+x)
eiArg = children(findSymType(eiTerm,'ei'),2);
eiArgSimp = simplify(collect(expand(eiArg),[x,c]));
fExpEiPart = subs(fExpEiPart,eiArg,eiArgSimp);

%Change of variables u = (e*c-/+x) to create the form expint(bu)
eiArgParts = symCell2arr(children(eiArgSimp));
eiArgXPart = eiArgParts(has(eiArgParts,x));
eq = u == eiArgXPart;
xSubs = (solve(eq,x,'IgnoreAnalyticConstraints',true));
expTerm = subs(expTerm,x,xSubs);
eiTerm = subs(eiTerm,[eiArgXPart,x],[u,xSubs]);

%Rewrite exponents in parts that do-and-do-not contain a u-dependence
expTermParts = symCell2arr(children(expand(prod(expTerm))));

if length(expTermParts) ==1 %In case only single exp. term available
    expTermParts = expTerm; %the following lines would have  returned
end                         %the exponent's argument and not the
                            %exponents themself
expTermsNoU = simplify(combine(prod(expTermParts(not(has(...
    expTermParts,u)))),'exp'));
expTermsU = combine(prod(expTermParts((has(expTermParts,u)))),'exp');

intTerm = diff(eiArgXPart,x)*intEiExpIdentity(expTermsU,eiTerm,u);

% Subsitute u back in.
% Notice the diff: this is the reason: d(h-x)/dx =-1; for proof that altenative
% identiy works, uncomment following lines.
% syms a b x h
% y(x) = -(1/a)*(expint((a+b)*(h-x))-exp(-a*(h-x))*expint(b*(h-x)))
% diff(y(x),x)

F = simplify(combine(fConstPart*sign*subs(expTermsNoU*intTerm,...
    u,eiArgXPart),'exp'));

end
```

intEiExpIdentity.m

```
function g = intEiExpIdentity(expTerm,eiTerm,x)
% Uses the following identity
% int exp(+-a*x)expint(bx) dx = -+1/a *(expint((-+a+b)*x)-exp(+-a*x)*expint(b*x))
% with a,b>0. Note for a>b, and the exp(ax) identity, the solution will blow-up
% eventually when x grows and have an imaginary part.
%
syms a b

% Assemble exp terms
expTerm = combine(expTerm,'exp');

% Find coefficients; and cast to a pretty form
a = -expand(subs(children(expTerm,1),x,1), 'ArithmeticOnly',true);
    %Identity assumes exp(-a*x),
    % but function input is of "exp(c*x)-form"

b = expand(subs(children(eiTerm,2),x,1),'ArithmeticOnly',true);

% Apply identity
g = simplify(1/a)...
    *(expint(x*(a+b))-exp(-x*a)...
    *expint(x*b));
```

```
23
24 end
```

C.3. Analytic Model, Numerical Implementation

The analytic solutions' numerical functions are not given in this manuscript.

createAnalyticSpectraSpec.m

```
1  clear all
2  close all
3  clc
4
5  % Gives analytic solution for the fluorescent radiative transfere
6  % equation on a mirror.
7
8
9  %%  Initialize model
10 nameResults = '\analyticWedgeMeasurement';
11 % Define system and import spectral-data
12 hp = 6.62607e-34;   %Planck's const.
13 vl = 299792458;     %Speed of light
14 % molar concentrations; excitation irradiance; quantum yields
15 cFl = 0.5*0.25e-3;
16 cEy = 0.5*0.25e-3;
17 E_0 = 1;
18 phiFl = 0.85; % From Fluorescence Properties of Twenty Fluorescein Derivatives:
19 phiEy = 0.2;  %
20
21
22 % Import spectral data
23 filePathSpectra = ['C:\Users\plok\Google Drive\Uni\Master\Scriptie',...
24     '\Matlab\SpectrumTool\Results\dataMasterSet.mat'];
25
26
27 % Absorption coeff. peaks [m^-1]
28 absCoPeakFl = 76.0e5*cFl;
29 %From: Spectrophotometric analysis of sodium fluorescein aqueous solutions.
30 %Determination of molar absorption coefficient
31
32 absCoPeakEy = 1.2*1.2*11.6e6*cEy;
33 %From: Data on eosin Y solutions for laser-induced
34 % fluorescence in water flows: it shows something close to or above 1e7
35 % Alternative: pH-Dependence of the absorption and fluorescent properties
36 % of fluorone dyes in aqueos solutions. Shows something close to to 2.2e7
37
38 % set-up dye spectral absorption and reflectivity properties
39 data = open(filePathSpectra);
40 wvlArray = data.wavelengths;
41
42 % Excitation wvl [m]
43 wvlLED      = 450e-9;
44
45 % Tranmission spectrum of filter, fibre and coupling lenses: Normalized to 1.
46 T = data.FilterTransmission;
47
48 % Spectrometer sensitivity
49 specSens = normalize(data.LampSpectrum, 'range')...
50     ./normalize(data.LampReferenceSpectrum,'range');
51 specSens = smoothdata(specSens,'gaussian',15);
52
53 % Absorption == Excitation spectrum of fluorescein and eosin
```

```
54  eyAbs = absCoPeakEy*(normalize(data.eosinYAbsWater,'range'));
55  flAbs = absCoPeakFl*(normalize(data.FluoresceinAbsWater,'range'));
56
57  % Eosin emissions. Filter, T, slightly bleeds into eyEm, cannot be removed
58  eyEm = data.eosinYEmWater./(specSens);
59  eyEm(isnan(eyEm)) = 0;
60  eyEm = normalize(eyEm, 'range');
61  eyEm = eyEm/sum(eyEm);
62
63  % Fluorescein Em. Filter, T, slightly bleeds into flEm, cannot be removed
64  flEm = data.FluoresceinEmWater./(specSens);
65  flEm(isnan(flEm)) = 0;
66  flEm = normalize(flEm, 'range');
67  flEm = flEm/sum(flEm);
68
69  % Mirror
70  rho_arr = data.MirrorCoating;
71
72  % Shift spec:
73  eyEm = circshift(eyEm,-18); % -18 self-measured. slightly red-shifted due to thick layer.
74  eyAbs = circshift(eyAbs,0); % 2 according to literature; self-measured
75  flEm = circshift(flEm,1);   % 1 according to literature; have some doubts
76  flAbs = circshift(flAbs,0); % 2 according to liteterature; self-measured
77
78  % Absorption of excitation light
79  ledIdx = 142;
80  a_1e = flAbs(ledIdx);
81  a_2e = eyAbs(ledIdx);
82
83  % Path correction length for excitation light coming in at an angle
84  % h_effective = h / cos(theta)
85  corr = 1/cos(deg2rad(20));
86
87  % Medium absorption
88  medAbs = zeros(size(flAbs));
89  a_f = medAbs;
90  a_fe= a_f(ledIdx);
91
92  % Reflectivity
93  rho_e = rho_arr(ledIdx);
94
95  h = [20,500,900,2000]*1e-6;
96  h = [20,100,200,300,400,500,600,700,800,900,1000,2000]*1e-6
97  h = [20,100,200,300,400,500,600,700,800,900,1000]*1e-6
98
99  viewAngle = [0,1/8,1/4,3/8]*pi;
100 viewAngle = [0,deg2rad(32)]; % For measurement setup with camera
101 viewAngle = 0;
102 %% Find solution
103 noOfH = length(h);
104 noOfviewAng = length(viewAngle);
105 spectrumAnalytic = zeros(noOfH,length(wvlArray),noOfviewAng);
106
107 nu = cos(viewAngle); % pre-calculate directin cosine for speed-up
108 tic
109
110 % parfor kk = 1:noOfH %Code can be parallized for each different h
111 for kk = 1:noOfH
112     for jj = 1:noOfviewAng
113         %% Direct Photon Radiance: results of excitation light
114
```

```
115         % Fluorescein
116         spectrumLdFl = zeros(size(wvlArray));
117         for ii = 1:length(wvlArray)
118             incrLd = L_directSpec(nu(jj),h(kk),corr*...
119                 (a_1e+a_2e+a_fe),a_1e,flAbs(ii)+eyAbs(ii)+a_f(ii),...
120                 E_0,phiFl*flEm(ii),rho_e,rho_arr(ii));
121 
122             spectrumLdFl(ii) = incrLd;
123         end
124 
125 
126         % Eosin
127         spectrumLdEy = zeros(size(wvlArray));
128         for ii = 1:length(wvlArray)
129             incrLd = L_directSpec(nu(jj),h(kk),corr*...
130                 (a_1e+a_2e+a_fe),a_2e,flAbs(ii)+eyAbs(ii)+a_f(ii),...
131                 E_0,phiEy*eyEm(ii),rho_e,rho_arr(ii));
132 
133             spectrumLdEy(ii) = incrLd;
134         end
135 
136 
137         %% Indirect Photon Radiance: results of dye re-absorption re-emission light
138         spectrumLiFltoFl = zeros(size(wvlArray));
139         spectrumLiFltoFl = specInd(nu(jj),h(kk),wvlArray,...
140             corr*(a_1e+a_2e+a_fe),a_1e, flAbs+eyAbs+a_f, flAbs,...
141             E_0,phiFl,phiFl,flEm,flEm,rho_e,rho_arr);
142 
143         spectrumLiEytoFl = zeros(size(wvlArray));
144         spectrumLiEytoFl = specInd(nu(jj),h(kk),wvlArray,...
145             corr*(a_1e+a_2e+a_fe),a_2e, flAbs+eyAbs+a_f, flAbs,...
146             E_0,phiEy,phiFl,eyEm,flEm,rho_e,rho_arr);
147 
148         spectrumLiEytoEy = zeros(size(wvlArray));
149         spectrumLiEytoEy = specInd(nu(jj),h(kk),wvlArray,...
150             corr*(a_1e+a_2e+a_fe),a_2e,flAbs+eyAbs+a_f, eyAbs,...
151             E_0,phiEy,phiEy,eyEm,eyEm,rho_e,rho_arr);
152 
153         spectrumLiFltoEy = zeros(size(wvlArray));
154         spectrumLiFltoEy =  specInd(nu(jj),h(kk),wvlArray,...
155             corr*(a_1e+a_2e+a_fe),a_1e,flAbs+eyAbs+a_f, eyAbs,...
156             E_0,phiFl,phiEy,flEm,eyEm,rho_e,rho_arr);
157 
158 
159         %% Sum fluorescein and eosin spectra: change from photon to energy domain
160         spectrumAnalytic(kk,:,jj) = real(spectrumLdFl + spectrumLdEy +...
161             (spectrumLiFltoEy+spectrumLiFltoFl+spectrumLiEytoFl+...
162             spectrumLiEytoEy));
163 %         *hp*vl./wvlArray; %Convert to energy domain
164     end
165 end
166 
167 elapsedTime = toc;
168 
169 
170 %% Export data
171 medAbs = a_f;
172 descr = 'Rows correspond to h, columns to viewAngle.';
173 save([pwd,nameResults,'.mat'],...
174     'viewAngle','spectrumAnalytic','h','descr','rho_arr','medAbs','cFl',...
175     'cEy','phiFl','phiEy','absCoPeakFl','absCoPeakEy','wvlLED','elapsedTime');
```

specInd.m

```
function spec = specInd(nu,h,wvlArray,...
    a_e, a_es, a_arr,a_ds,E_0, q_d, q_i,...
    dEm, iEm, rho_e, rho_arr)
% Calculate the indirect radiance contribution of a specific fluorophore i,
% as caused by the radiation of fluorophore d.
%
% INPUTS
% nu viewing angle, direction-cosine
% h medium thickness
% wvlArray all wavelengths which are of interest
% a_e total absorption coefficient (m^-1) seen by excitation source
% a_es this fluorophore d's absorption coefficient for the excitation source
% a_arr the combined medium's and all fluorophores' absorption
% a_ds this is fluorophore i's absorption coefficient for all wavelengths
% E_0 excitation source's irradiation at the top of the medium
% q_d fluorophore d's quantum yield
% q_i fluorophore i's quantum yield
% dEm fluorophore d's emission spectrum; curve area normalized to equal 1
% iEm fluorophore i's emission spectrum; curve area normalized to equal 1
% rho_e specific reflectivity coefficient for excitation irradiance
% rho_arr reflectivity at all wavelengths
%
% OUTPUT
% Photon radiance spectrum of fluorohpore i, as caused by excitation from
% fluorophore d.

% Initiate spectrum
spec = zeros(size(wvlArray));

% Find-out where total absorption is low or high
idx = find(a_arr >= (0.001*max(a_arr)));
% idx = find(a_arr >= (1e-6*max(a_arr))); % For L_indirect test; Abs1 is
% very high
idxLim_a_i0 = find(a_arr < (0.001*max(a_arr)));
% idxLim_a_i0 = find(a_arr < (1e-6*max(a_arr))); % For L_indirect test


% Establish spectrum wavelength by wavelength
for ii = 1:length(idx)
        id = idx(ii);
        incrL = zeros(size(wvlArray));

        %Contribution of dye d emission at wavelength x to dye i emissions
        %at wavelength y.

        % At strong absorbing wavelengths
        incrL(idx) = L_indirectSpec(nu,h,a_e,a_es,...
            a_arr(id), a_arr(idx), a_ds(id), E_0, ...
            q_d*dEm(id), q_i*iEm(idx), rho_e,...
            rho_arr(id),rho_arr(idx));

        % At weak absorbing wavelengths
        incrL(idxLim_a_i0) = L_indirectSpecNo_a_i(nu,h,a_e,a_es,...
            a_arr(id), a_ds(id), E_0, ...
            q_d*dEm(id), q_i*iEm(idxLim_a_i0), rho_e,...
            rho_arr(id),rho_arr(idxLim_a_i0));

        % Denominator term can become zero for certain absorption and
        % direction-cosine combinations; reject and accept small
        % underestimation error
```

```
        incrL(isnan(incrL)) = 0;
        incrL(isinf(incrL)) = 0;
        spec = spec + incrL;

    end
end
```

C.4. Plot Ratio and Spectrums

PlotRatioAnalyticModels.m

```
clear all
close all
clc

%% Setup and get data
dirName = 'C:\Users\plok\Google Drive\Uni\Master\Scriptie\Matlab\ModelResults'
load(fullfile(dirName,'/analyticWedgeMirrorIrradiance20deg.mat'));
nameTEX = 'RatioLight0.tex'
reflCond = 'specular';


% Import spectral data
load('C:\Users\plok\Google Drive\Uni\Master\Scriptie\Matlab\SpectrumTool\Results\dataMasterSet

% Setup filter wavebands
wvlFilter520 = [510:0.5:528]*1e-9;
wvlFilter532 = [523.5:0.5:539.5]*1e-9;

% Setup filter transmissivities: obtained from manufacturer
% resample them at the wavelengths at which the analytic solution was
% calculated
filt532 = fliplr([0.49829,1.04171,2.25468,5.12734,11.42873,24.0103,43.13596,...
    64.73587,81.45908,90.69869,94.42489,96.19921,96.80226,97.20901,96.93609,...
    96.46327,96.1847,96.84495,96.72127,97.54354,97.35931,97.34093,96.93386,...
    94.63559,87.4587,72.30578,51.08831,29.84005,14.84017,6.59942,2.8578,...
    1.2435,0.58176]*0.01);

filt520 = fliplr([0.64469,2.97201,13.53116,39.34839,71.00861,91.15532,...
    97.07044,97.2268,96.89224,97.10666,97.12119,95.92615,87.51147,...
    62.82768,30.72126,9.35444,1.94364,0.42044,0.11291]*0.01);
filt520 = interp1(filt520,linspace(1,length(filt520),length(wvlFilter520)));

wvlFilter520_idx = wvlToIdx(wvlFilter520,wavelengths);
wvlFilter532_idx = wvlToIdx(wvlFilter532,wavelengths);

Camera = camera_pl_d795Green;

%% Build ratio
[H_f,ViewAngle] = meshgrid(h,viewAngle);
Ratio = zeros(size(H_f));

cam520 = Camera(wvlFilter520_idx).*wavelengths(wvlFilter520_idx);
cam532 = Camera(wvlFilter532_idx).*wavelengths(wvlFilter532_idx);

for ii = 1:length(h)
    for jj = 1:length(viewAngle)
        Ratio(jj,ii) = sum(spectrumAnalytic(ii,wvlFilter520_idx,jj)...
            .*cam520.*filt520./wavelengths(wvlFilter520_idx))...
            /sum(spectrumAnalytic(ii,wvlFilter532_idx,jj)...
            .*cam532.*filt532./wavelengths(wvlFilter532_idx));
```

```
    end
end

%% Plot Setup
% Defaults
width = 5;      % Width in inches
height = 3;     % Height in inches
alw = 0.75;     % AxesLineWidth
fsz = 10;       % Fontsize
lw = 1.5;       % LineWidth
msz = 8;        % MarkerSize

%%  Plot Ratio of the radiances versus h and viewing angle
figure(1)
pos = get(gcf, 'Position');
set(gca, 'FontSize', fsz, 'LineWidth', alw); %<- Set properties
set(gcf, 'Position', [pos(1) pos(2) width*100, height*100]); %<- Set size
surf(H_f*1e6,ViewAngle,Ratio,'FaceColor','none'), hold on
axis tight
view(70,30)
xlim([0,h(end)*1e6])
xlabel('$h$ / \si{\micro\meter}')
ylabel('$\theta$ / \si{rad} ')
zlabel("Ratio of Camera's Gray Levels")
title("Predicted Measurement Response for ERLIF method")
% Here we preserve the size of the image when we save it.
set(gcf,'InvertHardcopy','on');
set(gcf,'PaperUnits', 'inches');
%% Export to LATEX
cleanfigure;
matlab2tikz(nameTEX, 'width', '\fwidth',...
    'height','\fheight',...
    'interpretTickLabelsAsTex',true,...
    'parseStrings', false,'showWarnings',false);
```

wvlToIdx.m

```
function [wvlIdx] = wvlToIdx(wvl,wvlArray)

%Convert from wavelength to index of wvl array
wvl_c1 = length(wvlArray)-1; wvl_c2 = wvlArray(1); wvl_c3 = wvlArray(end)-wvlArray(1);
wvlIdx =  round(1 +  wvl_c1 * (wvl-wvl_c2) / wvl_c3 );

end
```

PlotSpectraCompareAnalyticAndMeasurement.m

```
clear all
close all
clc


% Name of figure
nameTEX = 'spectrums_meas_analytic_view0_irr20deg.tex';


%% Compensation for spectrometer sensitivity, and filter and fibre transmission
filePathSpectra = 'C:\Users\plok\Google Drive\Uni\Master\Scriptie\Matlab\SpectrumTool\Results\dataM
data = open(filePathSpectra);

% Wavelengths analytic
wvlAnalytic = data.wavelengths*1e9;
```

```
16
17 % Tranmission spectrum of filter, fibre and coupling lenses: Normalized to 1.
18 T = data.FilterTransmission;
19
20 % Spectrometer sensitivity
21 spectroSens = normalize(data.LampSpectrum, 'range')...
22     ./normalize(data.LampReferenceSpectrum,'range');
23 spectroSens = smoothdata(spectroSens,'gaussian',15);
24
25 %% Import Measurement Data
26 % File names for measurements
27 bounds = [1444, 2454];
28 dirName = 'C:\Users\plok\Google Drive\Uni\Master\Scriptie\SpectroMetingen\Metingen';
29
30 files = {"h500Light20Fibre0.txt",...
31     "h900Light20Fibre0.txt",...
32     "h2000Light20Fibre0M3.txt"};
33 % files = {"h500Light45Fibre0.txt",...
34 %     "h900Light45Fibre0.txt",...
35 %     "h2000Light45Fibre0M3.txt"};
36
37 % files = {"h500Light20Fibre45.txt" ,...
38 %     "h900Light20Fibre45.txt",...
39 %     "h2000Light20Fibre45.txt"}
40 %
41 % files = {"h500Light45Fibre45.txt" ,...
42 %     "h900Light45Fibre45.txt",...
43 %     "h2000Light45Fibre45.txt"}
44
45
46 % Obtain measured data: wavelenghts and specs.
47 wvlMeasure = zeros(length(files),bounds(2)-bounds(1) + 1);
48 specMeasure = zeros(length(files),bounds(2)-bounds(1) + 1);
49
50 for ii = 1:length(files)
51     [tmpWvl, tmpSpec] = getSpec(files{ii},dirName,bounds);
52     wvlMeasure(ii,:) = tmpWvl;
53     % Compensate for spectrometer sensitivity
54     specMeasure(ii,:) = normalize(tmpSpec./...
55         interp1(wvlAnalytic,spectroSens,tmpWvl), 'range');
56 end
57 clear tmpWvl tmpSpec
58
59
60
61 %% Obtain analytic data: wavelenghts and specs.
62 % Analytic results
63 dirName = 'C:\Users\plok\Google Drive\Uni\Master\Scriptie\Matlab\ModelResults';
64 load(fullfile(dirName,'/analyticMeasurementControlIrradiance20deg.mat'));
65
66 % load(fullfile(dirName,'/analyticMeasurementControlIrradiance45deg.mat'));
67 % Spectrum analytic: compensate for fibre and filter transmission
68 % specAnalytic = normalize(spectrumAnalytic(2:4,:,1).*T.*spectroSens,2,'range');
69 specAnalytic = normalize(spectrumAnalytic(2:4,:,1).*T,2,'range');
70 hPlot = h(2:4);
71
72
73
74 %% Plot Setup
75 % Defaults
76 width = 6;     % Width in inches
```

```
77  height = 3;     % Height in inches
78  alw = 0.75;     % AxesLineWidth
79  fsz = 10;       % Fontsize
80  lw = 1.5;       % LineWidth
81  msz = 8;        % MarkerSize
82  colour = {'#0072BD','#77AC30','#4DBEEE'};
83
84  %% Plot spectrogram
85  figure(2)
86  pos = get(gcf, 'Position');
87  set(gca, 'FontSize', fsz, 'LineWidth', alw); %<- Set properties
88  set(gcf, 'Position', [pos(1) pos(2) width*100, height*100]); %<- Set size
89  error = zeros(3,length(wvlAnalytic));
90  for ii = 1:3
91      plot(wvlAnalytic,specAnalytic(ii,:),'LineStyle','--','Color',...
92          colour{ii},'LineWidth',lw), hold on
93      plot(wvlMeasure(ii,:),specMeasure(ii,:),'LineStyle','-','Color',...
94          colour{ii},'LineWidth',lw)
95  %       find differences between measured and analysed
96  %     resampSpecMeasure = interp1(wvlMeasure(ii,:),specMeasure(ii,:),wvlAnalytic);
97  %     error(ii,:) = resampSpecMeasure./specAnalytic(ii,:);
98  end
99  axis tight
100 ylim([0.01,1])
101 xlabel('$\lambda$ / \si{\nano\meter}')
102 ylabel({'Normalized Photon radiance / -'})
103 yticklabels({})
104 legend('Analytic $h=500$\si{\micro\meter}','Measurement ...',...
105     'Analytic $h=900$\si{\micro\meter}','Measurement ...',...
106     'Analytic $h=2000$\si{\micro\meter}','Measurement ...')
107 legend('boxoff')
108
109
110 % Here we preserve the size of the image when we save it.
111 set(gcf,'InvertHardcopy','on');
112 set(gcf,'PaperUnits', 'inches');
113
114 %% Export to LaTeX
115 cleanfigure;
116 matlab2tikz(nameTEX, 'width', '\fwidth',...
117     'height','\fheight',...
118     'interpretTickLabelsAsTex',true,...
119     'parseStrings', false,'showWarnings',false);
120
121 %% Function to get wvl and spec from measurement file
122
123 function [wvl, spec] = getSpec(fileName,dirName,bounds)
124     % Get Data
125     file = fopen(  fullfile(dirName,'/',fileName),'r');
126     Datac = textscan(file, '%f %f', 'Delimiter',' ','HeaderLines',17,...
127         'CommentStyle', '>>>>>','CollectOutput',1);
128     data = Datac{1};
129     fclose(file);
130
131     % Extract wavelengths and process spectrum
132     idl = bounds(1);
133     idu = bounds(2);
134     dataSel= data(idl:idu,:);
135     wind = 15;
136     spec = normalize(smoothdata(dataSel(:,2),'gaussian',wind),'range');
137     wvl = dataSel(:,1);
```

```
138 end
```

C.5. Create Dataset

Datasets are the spectrums of the dyes and measurement setup components.

ResampleDataSets.m

```
1  %% resample created datasets == spectrum
2  % Resample all datasets at specified wavelengths, and safe the resampled datasets in
3  % one masterset for later use.
4  clear all
5  wavelengths = (380:0.5:750)*1e-9;
6  dataSetList = dir('**/DataSets/*.mat');
7
8
9  fileName = fullfile(pwd,'Results','dataMasterSet');
10 save(fileName,'wavelengths');
11
12
13 for ii = 1:length(dataSetList)
14     fieldName = erase(dataSetList(ii).name,'.mat');
15     loadedDataSet = load(fullfile(pwd,'DataSets',fieldName));
16     oldWaveLengths = loadedDataSet.(char(fieldnames(loadedDataSet)))(:,1);
17     if 1e-6 < max(oldWaveLengths)
18         oldWaveLengths = oldWaveLengths *1e-9; %Some old data is in nm, not m
19     end
20     signal = loadedDataSet.(char(fieldnames(loadedDataSet)))(:,2);
21     assignin('base',fieldName,interp1(oldWaveLengths,signal,wavelengths,'makima',0));
22     save(fileName,fieldName,'-append')
23 end
24
25 save(fullfile(pwd,'Results','dataMasterSet.mat'),'dataMasterSet');
```

csv2DataSet.m

```
1  %% 26/05/2021 create a dataset from an csv file
2  % Many fluorophore spectra are available for download in the form of a csv.
3  % Here, a csv file is reworked and saved to a mat file. Raw datasets must
4  % have .txt file type
5
6  dataSetList = dir('**/rawCsvDatasets/*');
7
8
9  %%
10 for ii = 1:length(dataSetList)
11     if dataSetList(ii).bytes >= 1
12         fieldName = erase(dataSetList(ii).name,'.txt');
13         fieldName(isstrprop(fieldName,'alphanum')==0) =[]; %clean up names
14         dataSet = load(fullfile(pwd,'rawCsvDataSets',dataSetList(ii).name)); %lazy programming
15         save(fullfile(pwd,'DataSets',fieldName),'dataSet');
16     end
17 end
```

Bibliography

[1] L. Biasiori-Poulanges, S. Jarny, and H. El-Rabii. Data on eosin y solutions for laser-induced fluorescence in water flows. *Data in Brief*, 29:9, 2020.

[2] J.M. Cabeza-Lainez, J.A. Pulido-Arcas, and M.V. Castilla. New configuration factor between a circle, a sphere and a differential area at random positions. *Journal of Quantitative Spectroscopy and Radiative Transfer*, 129:272–276, 2013. doi: https://doi.org/10.1016/j.jqsrt.2013.06.027.

[3] DLMF. *NIST Digital Library of Mathematical Functions*. http://dlmf.nist.gov/, Release 1.1.6 of 2022-06-30. URL http://dlmf.nist.gov/. F. W. J. Olver, A. B. Olde Daalhuis, D. W. Lozier, B. I. Schneider, R. F. Boisvert, C. W. Clark, B. R. Miller, B. V. Saunders, H. S. Cohl, and M. A. McClain, eds.

[4] S. M. El-Bashir, F. F. Al-Harbi, H. Elburaih, F. Al-Faifi, and I. S. Yahia. Red photoluminescent pmma nanohybrid films for modifying the spectral distribution of solar radiation inside greenhouses. *Renewable Energy*, 85:928–938, 2016. ISSN 0960-1481. doi: https://doi.org/10.1016/j.renene.2015.07.031.

[5] H. Ertürk and J.R. Howell. *Monte Carlo Methods for Radiative Transfer*, pages 1–43. Springer International Publishing, Cham, 2017. ISBN 978-3-319-32003-8. doi: 10.1007/978-3-319-32003-8_57-1.

[6] Á.I. Fábián, T. Rente, J. Szöllősi, L. Mátyus, and A. Jenei. Strength in numbers: Effects of acceptor abundance on fret efficiency. 11(17):3713–3721, 2010. ISSN 1439-4235. doi: https://doi.org/10.1002/cphc.201000568.

[7] M. Geller and E.W. Ng. A table of integrals of the exponential integral. *Journal of Research of the National Bureau of Standards*, 73(3):191–210, 1969.

[8] G. G. Guilbault. *Practical fluorescence*. CRC Press, 2020.

[9] T. Hagemeier, M. Hartmann, M. Kühle, D. Thévenin, and K. Zähringer. Experimental characterization of thin films, droplets and rivulets using led fluorescence. *Experiments in Fluids*, 52(2):361–374, 2011. doi: 10.1007/s00348-011-1232-x.

[10] R. P. Haugland. *Handbook of fluorescent probes and research products*. Molecular Probes, Eugene Oregon, 9 edition, 2002.

[11] C. H. Hidrovo and D. P. Hart. Emission reabsorption laser induced fluorescence (erlif) film thickness measurement. *Measurement Science and Technology*, 12(4):467–477, 2001. doi: 10.1088/0957-0233/12/4/310.

[12] S.J. Hoff and K.A. Janni. Monte carlo technique for the determination of thermal radiation shape factors. *Transactions of the ASAE*, 32(3):1023–1028, 1989.

[13] N. M. Husen. *Skin friction measurements using luminescent oil films*. Thesis, 2017.

[14] N. M. Husen, T. Liu, and J. P. Sullivan. The ratioed image film thickness meter. *Measurement Science and Technology*, 29(6):13, 2018. ISSN 0957-0233 1361-6501. doi: 10.1088/1361-6501/aabd27.

[15] A. D. Klose, V. Ntziachristos, and A. H. Hielscher. The inverse source problem based on the radiative transfer equation in optical molecular imaging. *Journal of Computational Physics*, 202 (1):323–345, 2005.

[16] A.D. Klose. *Radiative transfer of luminescence light in biological tissue*, pages 293–345. Springer Berlin Heidelberg, Berlin, Heidelberg, 2009. ISBN 978-3-540-74276-0. doi: 10.1007/978-3-540-74276-0_6.

[17] G. M. Krekov, M. M. Krekova, A. A. Lisenko, and G. G. Matvienko. Reabsorption of laser-induced fluorescence in a plant canopy: Stochastic model. *Optics and Spectroscopy*, 106(4):514–519, 2009. ISSN 1562-6911. doi: 10.1134/S0030400X09040092.

[18] J. R. Lakowicz. *Principles of Fluorescence Spectroscopy*. Springer Science+Business Media, New York, third edition, 2010.

[19] S. Leyre, M. Withouck, G. Durinck, J. Hofkens, G. Deconinck, and P. Hanselaer. Modelling fluorescent materials with a spectral overlap between excitation and emission spectrum. In *Proceedings 2nd International Conference on Photonics, Optics and Laser Technology*, pages 33–38. ISBN 9897580085.

[20] A. Liemert, D. Reitzle, and A. Kienle. Analytical solutions of the radiative transport equation for turbid and fluorescent layered media. *Scientific Reports*, 7(1):3819, 2017. doi: 10.1038/s41598-017-02979-4.

[21] Y. Ma, J. Sun, and X. Luo. Multi-wavelength phosphor model based on fluorescent radiative transfer equation considering re-absorption effect. *Journal of Luminescence*, 209:109–115, 2019. doi: https://doi.org/10.1016/j.jlumin.2019.01.038.

[22] R. McCluney. *Introduction to radiometry and photometry*. Artech House, Boston, second edition. edition, 2014. ISBN 9781608078349.

[23] M. Michalec, P. Svoboda, I. Křupka, and M. Hartl. A review of the design and optimization of large-scale hydrostatic bearing systems. *Engineering Science and Technology, an International Journal*, 2021. doi: 10.1016/j.jestch.2021.01.010.

[24] M.C. Mota, P. Carvalho, J. Ramalho, and E. Leite. Spectrophotometric analysis of sodium fluorescein aqueous solutions. determination of molar absorption coefficient. *International ophthalmology*, 15(5):321–326, 1991.

[25] M. Neuman, S. Edvardsson, and P. Edström. Solving the radiative transfer equation with a mathematical particle method. *Optics Letters*, 40(18):4325–4328, 2015. doi: 10.1364/OL.40.004325.

[26] J. P. A. Nijssen and R. A. .J. van Ostayen. Open form pressure balancing for compliant hydrostatic thrust bearings. *Advances in Mechanism and Machine Science*, pages 3965–3974, 2019. doi: 10.1007/978-3-030-20131-9_395.

[27] S. V. Patsayeva, V. I. Yuzhakov, and V. Varlamov. Laser-induced fluorescence saturation for binary mixtures of organic luminophores. In *ICONO'98: Laser Spectroscopy and Optical Diagnostics: Novel Trends and Applications in Laser Chemistry, Biophysics, and Biomedicine*, volume 3732, pages 147–156. International Society for Optics and Photonics.

[28] A. Peraiah. *An Introduction to Radiative Transfer : Methods and Applications in Astrophysics*. Cambridge University Press, Cambridge, UNITED KINGDOM, 2001. ISBN 9780511155314.

[29] L.J. Sandilands. Modeling fluorescence reemission in the one-dimensional radiativetransfer problem using the p3 approximation. *Journal of the Optical Society of America A*, 38(11):1631–1639, 2021. doi: 10.1364/JOSAA.434354.

[30] M. Schäferling. The art of fluorescence imaging with chemical sensors. *Angewante Chemie Interntional Edition*, 51(15):3532–3554, 2012. doi: 10.1002/anie.201105459.

[31] M. Schäferling and A. Duerkop. *Intrinsically Referenced Fluorimetric Sensing and Detection Schemes: Methods, Advantages and Applications*, book section Chapter 23, pages 373–414. Springer Series on Fluorescence. Springer-Verlag, 2008. ISBN 978-3-540-75206-6 978-3-540-75207-3. doi: 10.1007/4243_2008_023.

[32] S. J. Siers, J. P. A. Nijssen, and R. A. .J. Van Ostayen. Development and implementation of a film height measurement approach for deforming hydrostatic bearings. 2020.

[33] E. A. Slyusareva and M. A. Gerasimova. ph-dependence of the absorption and fluorescent properties of fluorone dyes in aqueous solutions. *Russian Physics Journal*, 56(12):1370–1377, 2014. doi: 10.1007/s11182-014-0188-8.

[34] A. E. Smart and R. A. J. Ford. Measurment of thin liquid films by fluoresence. *Wear*, 29:41–47, 1974.

[35] A. van Beek. *Advanced engineering design: lifetime performance and reliability*. TU Delft, sixth edition, 2015. ISBN 978-90-810406-1-7.

[36] R. A. .J. van Ostayen and J. P. A. Nijssen. Compliant hydrostatic bearings utilizing functionally graded materials. *Journal of Tribology*, 142(11), 2020. doi: 10.1115/1.4047299.

[37] R. A. J. van Ostayen, A. van Beek, and M. Ros. A mathematical model of the hydro-support: an elasto-hydrostatic thrust bearing with mixed lubrication. *Tribology International*, 37(8):607–616, 2004. doi: 10.1016/j.triboint.2004.01.008.

[38] F. Wardle. *Hydrostatic bearings*, pages 147–225. Elsevier Limited, 2015. ISBN 9780857091628. doi: 10.1533/9780857092182.147.

[39] C. .J. Willers. *Electro-Optical System Analysis and Design: A Radiometry Perspective*. SPIE Press, Bellingham, Washington (1000 20th St. Bellingham WA 98225-6705 USA), 2013. ISBN 9780819495693. doi: 10.1117/3.1001964.

[40] R.A. Yalçın and H. Ertürk. Monte carlo method solution of the broadband fluorescent radiative-transfer equation considering fluorescent cascade. *Applied Optics*, 60(4):1068–1077, 2021. doi: 10.1364/AO.410325.

[41] X.F. Zhang, J. Zhang, and L. Liu. Fluorescence properties of twenty fluorescein derivatives: lifetime, quantum yield, absorption and emission spectra. *Journal of fluorescence*, 24(3):819–826, 2014. ISSN 1573-4994.

[42] J. M. Zhao and L. H. Liu. *Radiative Transfer Equation and Solutions*, pages 1–46. Springer International Publishing, Cham, 2017. ISBN 978-3-319-32003-8. doi: 10.1007/978-3-319-32003-8_56-1.